INVESTIGATION ON NIR-SHIELDING MULTIFUNCTIONAL HEAT INSULATION COATING MATERIALS BASED ON ATO FOR ENERGY SAVING OF BUILDINGS

ZHONG HONG

PhD

The Hong Kong Polytechnic University

2019

The Hong Kong Polytechnic University

Department of Building Services Engineering

Investigation on NIR-Shielding Multifunctional Heat Insulation Coating Materials Based on ATO for Energy Saving of Buildings

ZHONG HONG

A thesis submitted in partial fulfillment of the requirements

for the Degree of Doctor of Philosophy

October 2018

CERTIFICATE OF ORIGINALITY

I hereby declare that this thesis is my own work and that, to the best of my knowledge and belief, it reproduces no material previously published or written, nor material that has been accepted for the award of any other degree or diploma, except where due acknowledgement has been made in the text.

                                                       (Signed)

          Zhong Hong   (Name of student)

ABSTRACT

Abstract of thesis entitled: Investigation on NIR-shielding multifunctional heat insulation coating materials based on ATO for energy saving of buildings

Submitted by: ZHONG HONG

For the degree of: Doctor of Philosophy

At The Hong Kong Polytechnic University in September 2018

In Hong Kong, the extensive use of building glazing materials is further leading to high heat gains through building envelop and high cooling demand. Therefore, over 50% of building energy consumption in Hong Kong arises from the air-conditioning systems for temperature cooling. Glazing windows are typically the weakest part of a building's thermal envelope. Onto the glazing windows applying transparent thermal insulation coatings, which can strongly shield the near infrared (NIR) and UV radiation and thus largely reduce the solar heat gain through windows, has been widely explored and applied in buildings in the aspect of energy conservation. For example, low-E coating, which possesses high reflection of light, has been widely applied in buildings in the past years. However, the low-E coating tends to cause light pollution because of its visible light reflection, which nowadays has been prohibited in many countries. Therefore, substitutes with selective bandwidth of light wavelength have attracted a large amount of attention.

This thesis newly presents a novel black TiO_2/ATO/Cs_xWO_3 triple-structured thin film for producing IR-blocking multifunctional heat insulation coating on glass with high transparency and excellent thermal blocking performance.

Firstly, a novel mixture of antimony doped tin oxide (ATO) and Cs_xWO_3 aqueous dispersions was obtained with controllable morphology, excellent optical properties and stability, through a controlled hydrothermal reaction and a series of optimization experiments. Generally, ATO, as a kind of transparent conductive oxides (TCO), shows optical property of high transmittance in visible light wavelength range and NIR absorption in the wavelength range of 1500 to 2500 nm. Meanwhile, the Cs_xWO_3 shows a high shielding performance in the NIR wavelength range of 800 to 1300 nm. Hence, a brand-new combination of ATO and Cs_xWO_3 coating in this thesis exhibits an excellent blocking characteristic in the whole NIR light wavelength range. However, the primary size of the as-prepared nanoparticles is more than 100 nm when using the traditional ceramic method, thus hindering the uniform dispersion of the nanoparticles in water and producing poor NIR shielding performance and visible light transmittance. In this study, nanoparticles of ATO and Cs_xWO_3 were successfully synthesized by controllable hydrothermal reaction with primary particle size of 5-10 nm. In addition, highly dispersive aqueous suspension was achieved by physical method with secondary particle size measured less than 60 nm. The blue transparent aqueous liquid was steady with no sedimentation after standing for 7 days.

After mixed with film-forming resins, the final coating was obtained onto glass samples. The transparent and NIR shielding coating consisting of binary components of ATO and Cs_xWO_3 was synthesized by using the waterborne polyurethane (WPU) as the matrix. The transmittances of WTNS coated glass samples in visible and NIR regions are 70.6% and 14.2%, respectively. As the samples show excellent thermal insulation property and see-through capability, the nanomaterials can be applied in building glazing facades for reducing solar heat gain through building envelop and saving energy for cooling.

Secondly, to furtherly enhance the ability of NIR light shielding, the black TiO_2 film mainly composed of self-doped TiO_2, was developed by controllable solvothermal technique and optimized electroreduction experiment. A portion of Ti^{4+} ions is reduced to Ti^{3+}, and then the oxygen vacancies are passively protected. Next, the electroreduction conditions have been investigated and optimized. The black-TiO_2 film exhibits an outstanding super-hydrophilicity with water contact angle lower than 5° and organic-matter degradation under illumination of natural light. Additionally, the prepared black TiO_2 effectively blocks more than 38% of the NIR light.

Finally, a novel TiO_2/ATO/Cs_xWO_3 tri-structured thin film was successfully fabricated in this study. Excitingly, it shows excellent NIR shielding performance and high visible transparency. The TiO_2 film acts as the external layer in the substrate glass with optimal thickness of 4 μm. Meanwhile, the ATO/Cs_xWO_3 film with an optimized thickness of 4.63

μm serves as the internal layer in the substrate glass. The visible transmittance and NIR absorbance of the entire thin films are 58.6% and 93.4%, respectively. Moreover, the tri-structured thin films also demonstrate prominent photocatalytic property, mirrored by a degradation test of 29.4% of methylene blue within 30 minutes. Hence, the tri-structured film shows a great potential in energy-efficient glazing windows.

PUBLICATIONS DURING PHD STUDY

Journal papers:

(1) Zhong, H., Hu, Y., Wang, Y., & Yang, H. (2017). TiO2/silane coupling agent composed of two layers structure: A super-hydrophilic self-cleaning coating applied in PV panels. *Applied Energy*, *204*, 932-938.

(2) Hu, Y., Zhong, H., Wang, Y., Lu, L., & Yang, H. (2018). TiO2/antimony-doped tin oxide: Highly water-dispersed nano composites with excellent IR insulation and super-hydrophilic property. *Solar Energy Materials and Solar Cells*, *174*, 499-508.

(3) Ji, Y., Rong, X., Zhong, H., Wang, Y., Wang, S., & Lu, L. (2017). Making Marble Powder Waste Profitable by Using Nano-TiO2 Surface Modification for Air Quality Improvement Applications. *Journal of Nanomaterials*, *2017*.

(4) Wen, T., Lu, L., & Zhong, H. (2018). Investigation on the dehumidification performance of LiCl/H2O-MWNTs nanofluid in a falling film dehumidifier. *Building and Environment*, *139*, 8-16.

(5) Wen, T., Lu, L., Zhong, H., & Dong, C. (2018). Experimental and numerical study on the regeneration performance of LiCl solution with surfactant and nanoparticles. *International Journal of Heat and Mass Transfer*, *127*, 154-164.

<u>Conference Paper:</u>

(1) Hong, Z., Yang, H., Yuanhao, W., & Hongxing, Y. (2017). TiO2/Silane Coupling Agent Composed Two Layers Structure: A Novel Stability Super-Hydrophilic Self-cleaning Coating Applied in PV Panels. *Energy Procedia*, *105*, 1077-1083.

(2) Hong, Z., Yuanhao, W., & Hongxing, Y. A novel transparent thermal insulation bilayer coating based on ATO/Black TiO2. 10th International Conference on Applied Energy (ICAE2018), 22-25 August 2018, Hong Kong, China

ACKNOWLEDGEMENT

This thesis would not be finished without the help and support of those who are gratefully acknowledged here.

First and foremost, I would like to express my sincere gratitude to my chief supervisor, Prof. Yang Hongxing, for his priceless trust, guidance, as well as his continuous support and encouragement towards the research goals. I thank him for offering me this opportunity of my PhD study, also for the guidance and support when I am confused. Besides, his noble personality is also an example for me.

My special appreciation is also devoted to my co-supervisor, Dr. Wang Yuanhao for his warm caring and insightful suggestion when I encountered some life troubles. I thank him so much for spending his time to proofread my research manuscripts and this thesis. He is more like a friend rather than a supervisor to me. Meanwhile, he is always my idol not only in research but also at work, due to his high intelligence quotient and high emotional quotient.

I also must express my gratitude to Prof. Lu Lin. She also gives much more help in my research and my life, I want to thank all my colleagues in Renewable Energy Research Group (RERG). Thank them all for spending three beautiful years with me.

Finally, I want to appreciate my wife and my daughter who are always encouraging me when I was in the lows of life, and my parents for their ubiquitous supports.

CONTENTS

LIST OF FIGURES

LIST OF TABLES

NOMENCLATURE

Abbreviations

NIR	Near infrared
UV	Ultraviolet
SEM	Scanning electron microscope
TEM	Transmission electron microscope
HTEM	High resolution transmission electron microscope
SAED	Selected area electron diffraction
XRD	X-ray diffraction
WCA	Water contact angle
EDX	Energy dispersive X-ray detector
ATO	Antimony doped tin oxide
ITO	Indium tin oxide
FTO	Fluorine doped tin oxide
TCO	Transparent conductive oxide
WPU	Waterborne polyurethane
MB	Methylene blue
LSPR	Localized Surface Plasmon Resonance

Symbols

ω_p	Collective electronic collective oscillation frequency
N	Concentration of material intrinsic carrier
Υ	Relaxation coefficient
ε_∞	High frequency dielectric constant
m*	Effective electron mass
e	Electron charge
Ne	Free carrier density
x	Average displacement
P	Negative recovery resistance of carrier

Chapter 1 Introduction

1.1 Motivation

As the country with the largest energy consumption in the world, China plays an essential role contributing to the total energy growth for the world. On 28th January 2017, the State Statistics Bureau of China published *the Statistical Bulletin of the People's Republic of China* on national economic and social development in 2016. As the initial assessment shown in the bulletin, the whole country consumed approximately 4.36 billion tons of standard coal of the total energy, which increased by 1.5% compared with that in 2015. Specifically, with a growth of 8% of natural gas consumption, 5% of electric power and 5.5%, of crude oil. Plus, sustainable development of carbon resources offers a method to tackle with energy shortage issues. Research programs involved have been added in the China 13th five-year plan. Therefore, energy serving, and sustainable development of carbon resources are the two important aims of energy development for China in the near future.

By the year 2016, energy consumption from residential and commercial buildings constituted 20.1% of total energy in the world. [1], which means that building energy consumption is the dominant part of global energy consumption. Likewise, the building energy consumption accounted for 30-40% of the total energy consumption, and specifically

more than 90% of building energy was used for heating, air conditioning, fan, and other household appliances. Materials with excellent heat preservation and thermal insulation performance are therefore significant for energy saving of buildings [2]. In contemporary society, to maintain the attractive appearance and sufficient lighting, glass acting as the replacement of concrete structures is applied widely on the roofs and walls of constructions. However, due to the high thermal transfer coefficient (U-value) of glass, it will consequently lead to low energy efficiency and high carbon dioxide emissions. With the precondition of not changing the existing constructions of buildings, we can reduce the energy consumption only by improving the insulation performance of glass. Many countries have done tons of tests and researches about energy-effective technologies on glass [3-5]. Among the commercially available products, there have coating thermal reflection glass, vacuum glass, insulating glass, laminated glass and so on. It has to be mentioned that, take the coating thermal reflection glass for instance, although with excellent insulation performance, it also causes Urban light pollution because of its high reflectivity for visible light [6]. In addition, the service life of insulating glass is short. Meanwhile the vacuum glass is set at the base of vacuuming the interlayer of insulating glass to achieve high insulation performance [7]. However, the high requirement of gas impermeability and the high manufacture cost make the vacuum glass hard to be widely utilized [8]. Laminated glass is mainly to attach a film made from infrared shielding materials on the surface of glass, which is mainly used in

automotive glass at present [9]. Due to the high cost, it is also difficult to be widely used in large area of construction glass.

In recent years, the so called "transparent thermal insulation coatings", acting as a new type of thin film technique, attracts wide attention from both academia and industry [10-13]. It is a combination of inorganic nano-transparent conductive oxide （TCO） and polymer resin films, which has selective shielding of near-infrared light and ultraviolet light while maintains a high visible light transmittance [14]. For sunlight radiation, ultraviolet (300~380 nm), visible light (380~780 nm), and near infrared light (780~2500 nm) account for 5% ,42% and 52%, respectively. In contrast, nano-transparent conductive oxide TCO (such as ITO, ATO, AZO) can selectively shield most the near-infrared light and ultraviolet light with a wavelength range of 200~2500 nm while maintaining a high visible light transmittance [15]. Therefore, it can achieve both of lighting and thermal insulation performance for buildings at the same time.

In some counties, transparent thermal insulation coatings have been widely utilized, but not be promoted in China yet. Obviously, lots of issues on transparent thermal insulation coatings still wait to be addressed. Firstly, TCO used in the coating is not ideal enough for selective absorption of the sunlight wavelength. For example, the visible light transmittance and the shielding effect of near infrared light is not sufficient. Secondly, the dispersion of nanoscale TCO in the medium is unstable, which will shorten the preservation time of

coatings. Thirdly, among the transparent thermal insulation coatings, the solvent based product is not environmental friendly, while the waterborne product has the poor performance on weatherability, low hardness, anti-aging performance and adhesion. Hence it is very important to develop a kind of water-based nano-transparent insulation coating with high near-infrared shielding, high visible light transmission, good weather resistance and dispersive stability.

1.2 Reference

[1] Buonomano, A., Forzano, C., Kalogirou, S. A., & Palombo, A. (2018). Building-façade integrated solar thermal collectors: Energy-economic performance and indoor comfort simulation model of a water-based prototype for heating, cooling, and DHW production. *Renewable Energy*.

[2] Ghosh, A., & Mallick, T. K. (2018). Evaluation of optical properties and protection factors of a PDLC switchable glazing for low energy building integration. *Solar Energy Materials and Solar Cells*, *176*, 391-396.

[3] Fang, Y., Eames, P. C., Norton, B., Hyde, T. J., Zhao, J., Wang, J., & Huang, Y. (2007). Low emittance coatings and the thermal performance of vacuum glazing. *Solar Energy*, *81*(1), 8-12.

[4] Liu, H. (2012). *The development of novel window systems towards low carbon buildings* (Doctoral dissertation, University of Nottingham).

[5] Chiba, K., Takahashi, T., Kageyama, T., & Oda, H. (2005). Low-emissivity coating of amorphous diamond-like carbon/Ag-alloy multilayer on glass. *Applied surface science*, *246*(1-3), 48-51.

[6] Reidinger, M., Rydzek, M., Scherdel, C., Arduini-Schuster, M., & Manara, J. (2009). Low-emitting transparent coatings based on tin doped indiumoxide applied via a sol–gel routine. *Thin Solid Films*, *517*(10), 3096-3099.

[7] Hammarberg, E., & Roos, A. (2003). Antireflection treatment of low-emitting glazings for energy efficient windows with high visible transmittance. *Thin Solid Films*, *442*(1-2), 222-226.

[8] Del Re, M., Gouttebaron, R., Dauchot, J. P., & Hecq, M. (2004). Study of the optical properties of AlN/ZrN/AlN low-e coating. *Surface and Coatings Technology*, *180*, 488-495.

[9] Wang, L., Hang, J., Shi, L., Sun, X., & Xu, F. (2012). Preparation and characterization of NIR cutoff antimony doped tin oxide/hybrid silica coatings. *Materials Letters*, *87*, 35-38.

[10] Ágoston, P., Albe, K., Nieminen, R. M., & Puska, M. J. (2009). Intrinsic n-type behavior in transparent conducting oxides: a comparative hybrid-functional study of In 2 O 3, SnO 2, and ZnO. *Physical review letters*, *103*(24), 245501.

[11] Edwards, P. P., Porch, A., Jones, M. O., Morgan, D. V., & Perks, R. M. (2004). Basic materials physics of transparent conducting oxides. *Dalton transactions*, (19), 2995-3002.

[12] Adamopoulos, G., Bashir, A., Gillin, W. P., Georgakopoulos, S., Shkunov, M., Baklar, M. A., ... & Anthopoulos, T. D. (2011). Structural and electrical characterization of ZnO films grown by spray pyrolysis and their application in thin-film transistors. *Advanced Functional Materials*, *21*(3), 525-531.

[13] Bang, K., Son, G. C., Son, M., Jun, J. H., An, H., Baik, K. H., ... & Ham, M. H. (2018). Effects of Li doping on the structural and electrical properties of solution-processed ZnO films for high-performance thin-film transistors. *Journal of Alloys and Compounds*, *739*, 41-46.

[14] Zhu, Q., Zhao, Q., An, Y., Anasori, B., Wang, H., & Xu, B. (2017). Ultra-microporous carbons encapsulate small sulfur molecules for high performance lithium-sulfur battery. *Nano Energy*, *33*, 402-409.

[15] Zhao, Y., Jiang, Y., Zheng, B., Zhuang, W., Zheng, Y., & Tian, Y. (2017). Influence of microwave vacuum drying on glass transition temperature, gelatinization temperature, physical and chemical qualities of lotus seeds. *Food chemistry*, *228*, 167-176.

Chapter 2 Literature Review

2.1 Classification of energy efficient glass

In architectures, glass has the highest heat transfer coefficient (U-values), About 60% thermal lose is caused by the existing architectural glass. Therefore, improving the thermal insulation of glass has always been a popular research topic.

Generally, there are three modes for heat transfer: heat convection, heat conduction and heat radiation. Convective heat transfer can be achieved by air convection because of the temperature difference between two sides of the glass, that is cold air rising on the one side and hot air falling on the other side. Heat conduction is a process of energy transferring by the movement of matter at molecular level; Radiation is to transfer energy by infrared light and ultraviolet light through the forms of radiation. As for transparent glass with high U-value, heat radiation is the main way to heat transfer. The fundamental technology of energy-saving glass is to achieve thermal insulation and energy saving by preventing one or several ways of heat transfer. At present, the main energy-saving glass products in the market include ~~such as~~ heat-absorbing glass, insulating glass, vacuum glass, low-e coating glass, heat-insulating film glass and insulating film glass, etc [1].

2.1.1 heat-absorbing glass

Figure 2.1 The optical properties of three kinds of tinted glass

color	visible light transmittance（%）	Solar direct transmittance（%）
tawney	≥42	≤60
grey	≥30	≥60
blue	≥45	≥70

The heat-absorbing glass is also called tinted glazing. The preparation of tinted glass is to add small metal ions into the raw materials of glass during the float process, or to spray the metal oxides directly on the glass surface. These micro additions make glass with specific colors such as green, blue, gray and bronze. Without changing other properties of the glass, the glass absorbs lights within a specific wavelength region in the solar spectrum, making the glass with a uniform color from overall thickness. Tinted glass can not only reduce the heat radiation from the sun, but also avoid unnecessary glare during the day time. Experimental results of Chow et al [2] show that thermal radiation of rooms with colored glass can be reduced by 20% or even higher. For example, blue and green glass have higher visible light transmittance and lower thermal radiation, which make them have a good market prospect. The specific optical properties of tinted glass are shown in table 2.1 [3].

Although heat absorbing glass can block about 50% of the solar radiation to achieve the heat insulation effect, the table also shows that heat absorbing glass is at the expense of the visible light transmittance, which therefore will increase the building energy consumption for lighting.

2.1.2 Hollow glazing

Hollow glazing has both heat insulation and sound insulation performance. During

the preparation process, the insulating glass is composed of several pieces of glass (usually two pieces) bonded together through a frame made by a high gas tightness adhesive, and desiccant is put in the middle. This highly efficient hollow glazing basically has same appearance as ordinary glass. Figure 2.1 shows the structure of the hollow glazing.
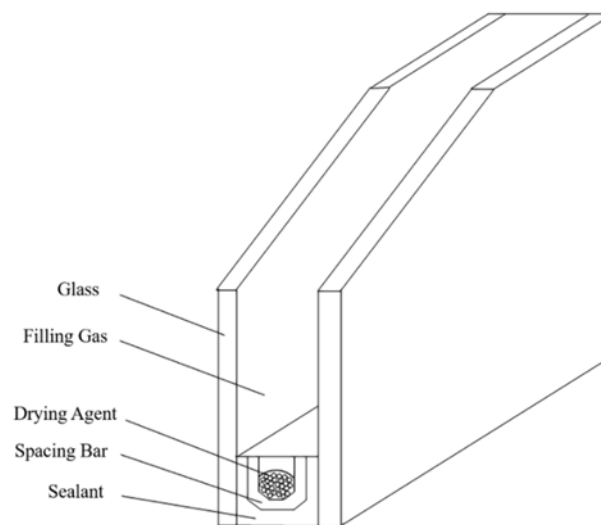
Figure 2.2 Schematic of a hollow glazing

Hollow glazing is to prevent heat conduction and convective heat transfer. The interior part of the hollow glass is a closed space, and the air inside has a heat transfer coefficient which is far less than that of glass itself, Plus, heat convection does not happen in the air inside and on both sides of the glass. therefore, hollow glass achieves the good effect of heat insulation and sound insulation. There are many production methods for insulating glass: welding, gluing, welding and gluing. In the buildings, glue is often used for preparation [4].

The practical application of hollow glass is still insufficient and with short life due

to the fatal weakness. Actually, the service life of single sealed insulating glass is only about 5 years. The performance of invalid hollow glass is worse than ordinary glass. such as negative effect on the esthetic performance because of impurity of inner space. If the indoor and outdoor temperature difference reaches a certain extent, the inside of the hollow glass will dew and even frost, which seriously affects the transparency and lighting of the glass, thus causes other undesirable effects [5].

2.1.3 Vacuum glass

The concept of vacuum glass was firstly proposed by Zoller [6] in 1913. A standard vacuum glass is composed of two layers of glass, with little gas in the middle layer, forming a narrow vacuum space, and the two layers of glass are maintained stably through the bulking agent between them, as is shown in figure 2.2. The bulking agent is put inside at a specific distance, which is very small, so it will not affect the overall transparency of the glass [7].

For the principle of heat insulation, vacuum glass and hollow glass are similar with each other, using the vacuum gap between two sides of two layers of glass to eliminate two means of heat transfer, heat convection and heat conduction. However the vacuum glass has better insulation performance and higher thermal resistance, and also has better condensation resistance and frost resistance [8].
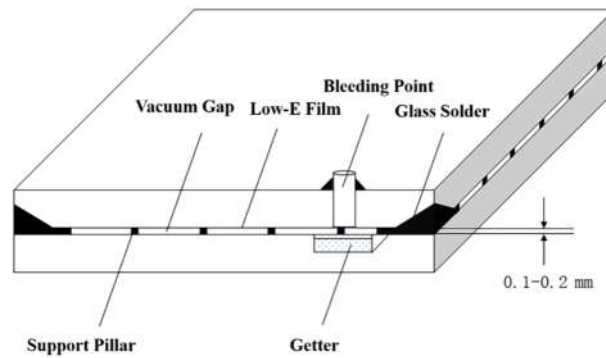
Figure 2.3 Schematic of a vacuum glazing

In combination with low emissivity coatings, which is plated on the inner face of vacuum glass, it can greatly improve the insulation effect of glass. However, at present, the vacuum glass technology is still in the initial stage, and the vacuum sealing technology as well as supporting technology between two glass plates has high technical difficulties to overcome. At the same time, the preparation process vacuum glass involves of vacuum insulation, low melting point welding and silicate, and technologies of interdisciplinary disciplines [9]. Therefore, the vacuum glass still requires further research and development, and it has not been widely utilized nowadays.

2.1.4 Low-E coated glass

Low emissivity coated glass also named as low-e (Low Emissivity) coated glass, is to plate metal or metal oxides on the glass surface, under the precondition of allowing most of the visible lights to pass through. It reflects a large number of optical radiations of other wavelength thereby reducing unnecessary heat absorption or heat loss. According to the production mode, low-e glass can be divided into online low-e glass and offline low-e glass. Off-line low-e glass with a wide range of types in the process

of production is tempered before coated, which can be controlled within 3 ~ 12 mm thickness, and the "hard coating" mode of production is to make the service life up to 30 years. Online low-e glass is toughened with coatings. However, this "soft coating" mode of production process of toughened glass itself is hard to control due to the heating asymmetry and will cause problems such as large toughened deformation to the glass. The product of this type of glass (a) is at thickness of only 6 mm with a short service life, which cannot be exposed in the air, and need to add additional protective layers. However, online low-e glass has higher visible transmittance and higher infrared reflectance, which means the insulation effect is more pronounced [10-13].

The energy-saving principle of low-e coating glass is mainly the reflection effect of low-e glass in the far-wave radiation above 2500 nm. We know that more than 90% of the solar radiation energy is almost in the wavelength range of 300 ~ 2500 nm, and the radiation energy of objects under 100 ℃ is far larger than 2500 nm wavelength range. When the sun rays go through the glass and cast on the indoor items, which radiate again at a distant wavelength. These wave radiation is reflected by the low-e glass, to prevent rising glass temperature caused by the secondary radiation, and hence to achieve insulation effect. On cloudy days and nights, low-e glass can effectively prevent heat loss. The research shows that low-e coating glass can reduce the 48% heat of the window, so low-e coating glass is widely used in modern buildings and becomes the mainstream product in the market [14].

However, low-e glass is still inadequate. On the one hand, low-e glass reflects

sunlight and causes serious light pollution to cities. On the other hand, the dominant methods of preparation for low-e glass are magnetron sputtering method and high temperature pyrolysis deposition method. These two methods are complex and expensive. For online low-e glass, it has short service life, and it cannot modify the existing urban construction with offline low-e glass. These deficiencies require further research and improvement [15].

2.1.5 Heat-insulating film glass

For the heat-insulating film glass, which actually is one kind of low-e glass with low radiation membrane according to the essential principle, it is made through combining the shielding function of metal oxide materials and film-forming characteristics of PET (polyester resin matrix) together to prepare a kind of heat insulation film on the glass. This kind of insulation film can not only be applied to the installation of energy-saving windows in new buildings, but also reform energy conservation in existing buildings [16].

The application of thermal insulation film glass for automotive is more extensive than that for building glass. Many common car stickers on the market come from large multinational companies such as 3M, which have mastered the core technology and monopolized the existing market [17]. On one hand, preparation equipment is extremely expensive, and the process is complicated. On the other hand, film glass is prone to rupture when being used. Production problems such as bubbles prevent the heat insulation film glass from being widely used in construction of large area.

2.1.6 Thermal insulation painted glass

In recent years, with the rapid development of research for nano-materials and nano-dispersion techniques, the preparation of thermal insulation painted glass made by transparent heat insulation coating, a new type of building energy-saving glass gradually comes to people's horizons. This kind of insulation painted glass has a controllable high visible light transmittance (50%~90%), which also has a very high shielding effect on near-infrared light and ultraviolet light [18-20].

Transparent insulation coatings used in the preparation of thermal insulation painted glass, are made from nano inorganic Transparent Conductive Oxides （TCO） and organic polymer resin film-forming agents. The coating preparation process is simple: disperse nano conductive oxides with near infrared absorption effects by using physical and chemical scattering into the dispersion medium, form stable dispersion solution, then mix it with film-forming agents of resin matrix according to a certain ratio, and trace amounts of dispersing agents, defoamer, tackifier coating additives, and finally stir them well to get the final coating. The produced coating can be coated on the glass surface by spraying, pouring, brushing, etc, with means of natural air drying or hot solidification, UV curing, to form heat insulation coated glass.

The research shows that [21], the transparent insulation coating can maintain the visible transmittance of 80%, and meanwhile absorb most of the near-infrared light, so as to achieve good thermal insulation and energy-saving effect. The production process of transparent insulation coating is facile, the required production equipment such as sanding machine and water kettle polyurea are at a friendly price. Meanwhile, the

construction method of transparent insulation coating is concise, and staff training cycle is short. These advantages indicate the great application prospect and development potential of the transparent insulating coating in the future of energy-saving glass technology. At present large corporations related with coating materials, such as RPM in the United States has done researches about coating insulating glass, and there have been relatively mature technology and products. In China, also did large exploration and studies of transparent insulation coating [22].

However, there are still some technical problems to be solved [23]. The first one is that the TCO commonly used for coating is not ideal for selective absorption of the sunlight wavelength. The optical transmission rate is not high enough and the shielding effect of the near infrared light is not sufficient yet. Secondly, the dispersion of nano-TCO in the medium is unstable, thus the preservation life of the coating is shortened accordingly. Thirdly, in the transparent insulation coatings, the solvent-based product is not environmentally friendly, while the waterborne coating has poor weatherability and low hardness, low anti-aging performance, and low adhesion. Therefore, developing a type of nano transparent heat insulation coating with high near infrared shielding, high visible light transmittance, good weatherability and water dispersion stability, is of great importance to research significance and tremendous economic benefit.

2.2 Literature review of transparent conductive oxides

In contemporary society, the application and reservation of energy is a big concern.

The researchers focused on coatings about capturing and using sunlight, reducing energy loss and so on. At present, many technologies and related equipment have been developed and commercialized rapidly. Transparent conductive Oxides (TCO) play an important role in energy capture and energy conservation. In order to obtain high visible light transmittance and conductivity, it should be insured that these materials are not absorbed at the wavelength region from 380nm (3.26eV) to 780nm (1.59eV), which also means their optical bands must be greater than 3.2eV. This transparent material with high conductivity provides a technical basis for many important technologies such as flat panel displays, solar capture, transparent insulation coatings, and other optoelectronic devices. Nowadays, mainstream transparent conductive oxides include In_2O_3, SnO_2, CdO, $CdIn_2O_4$ ZnO and their adulterants, as shown in table 2.2. All of them are N-type TCO materials, because the electrical properties of N-type TCO materials are better than that of the P-type TCO materials [24-28]. N-type TCO materials including nanometer antimony tin oxide (ATO), nanometer indium tin oxide (ITO) are produced by chemically doping N-type TCO material to close the conduction band levels of the donors [29], electrons of which enter into the conduction band by thermal ionization. P - type TCO material provides the acceptors with band levels through oxygen vacancy. According to the Drude theory, the electron is produced by further doping, and the material can get high conductivity and far infrared absorption capacity, while maintain the transparency within the visible range [30].

The conductive properties of TCO materials are mainly improved by oxygen

vacancy and doping. For most of the metal oxides, Conduction band Minimum level (CBM) is composed of spatial extension of spherical metal s orbit. If electron delocalization happens within the orbit, it will form a wide band gap. High doping can make the material have high conductivity. However, the maximum value of the valence band is made of the 2p orbital of the non-oxidized oxygen, and the discretization of the valence band is very small, it is difficult to be doped with holes. Therefore, it was not until 1997 that the first p-type TCO material was discovered, compared to the n-type TCO material, which was discovered in 1954 [31-32].

Figure 2.4 Classification of the N-type TCO materials

Host	In_2O_3	SnO_2	ZnO	CdO
Dopant	Sn, Ge, Mo, F, Ti, Zr, Hf, Nb, Ta, W, Te	Sb, F, As, Nb, Ta	Al, Ga, B, In, Y, Sc, F, V, Si, Ge, Ti, Zr, Hf	In, Sn

At present, most researches on TCO focus on the SnO_2 series, ZnO series, indium oxide (In_2O_3) series and ternary compounds. Early studies have shown that simple binary oxides such as tin oxide and zinc oxide are characterized with high conductivity and optical transparency [33]. By doping these binary oxides, the conductivity can be further improved [34-36]. Studies also have shown that AZO has the most potential to be used as TCO to replace the ITO and FTO. What is more, ITO, ATO, AZO, FTO, etc. as TCO materials have the advantages including chemical stability, high temperature resistance and high conductivity, and they have been widely used in photovoltaic industry and energy-saving glass of buildings [36-38].

2.2.1 Tin dioxide SnO₂

SnO₂ is a wide-band semiconductor with an optical band of 3.6 eV. Tin oxide has the structure of tetragonal rutile, and the corresponding spatial group is D14 (P42/ MNM) [39]. The structure unit contains two tin atoms and four oxygen atoms. Each tin atom has six oxygen atoms around it, forming a regular octahedron. Each oxygen atom is surrounded by three tin atoms, forming an equilateral triangle. The lattice parameters are: a=b=4.747 Å, c=3.185 Å. The ionic radius of O^{2-} and Sn^{4+} is 1.40 Å and 0.71 Å respectively. The specific crystal structure is shown in figure 2.3.
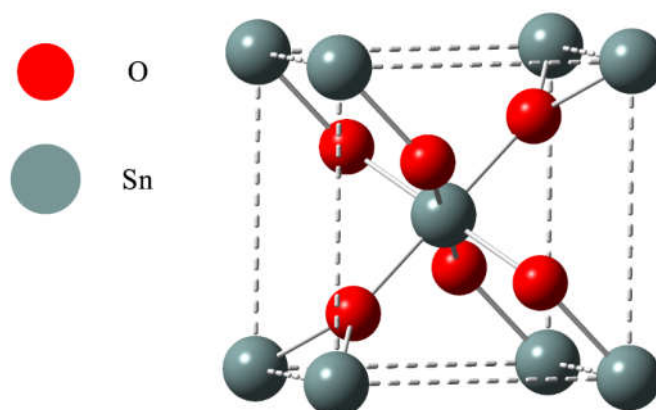
Figure 2.5 The crystal structure of SnO₂

Due to the wide band gap, stoichiometry of tin oxide is an insulator. However, its conductivity can be improved by increasing oxygen vacancies (non-stoichiometric tin oxide film) and adding dopant impurities such as antimony and fluorine. The oxygen vacancy of n-type tin oxide film can be generated through the following process:

$$O_O^x \leftrightarrow V_{\ddot{O}} + \frac{1}{2}O_2 + \frac{1}{2}e^- \tag{2.1}$$

When one of the oxygen atoms in dioxygen has been removed, then an oxygen

vacancy is present, with a double positive charge. The two black dots above the oxygen symbol in the equation represent the oxygen releasing an electron pair. This is the classic mechanism of n-type conductivity without doping. But recent calculations suggest that hydrogen doping can also improve conductivity in oxygen vacancies. On the other hand, the doping of Sb5+ instead of Sn4+ can produce free electrons in the guide band, that is $Sn_{1-x}^{4+}Sb_x^{5+}O_2^{2-} + xe^-$, fluorine anions can also produce free electrons by replacing oxygen anions, $Sn^{4+}O_{2-x}^{2-}X + xe^-$, where X stands for fluorine or other halogens doping dopants [40-42].

2.2.2 Zinc Oxide

The mineral of zinc oxide is known as the red zinc ore, which has a hexavalent (B4) lattice, with which the zinc atoms are arranged in the form of almost six cubic meters. The oxygen atom is in the tetrahedral cluster of four zinc atoms. These tetrahedrons point forward same direction along the hexagonal axis, giving the lattice a polar symmetry. The cell constants are: a=b=3.24 a, c=5.19 a. The specific crystal structure is shown in figure 2.4.
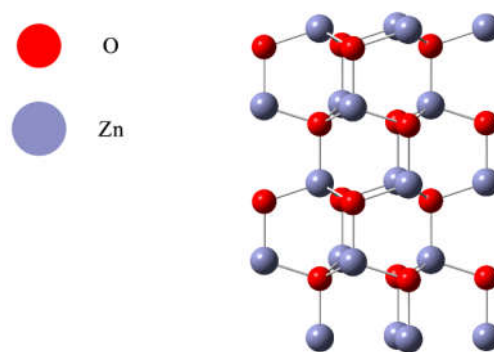
Figure 2.6 The crystal structure of zinc oxide

Many research groups have carried out computational studies on the band structure of zinc oxide [43], and the calculated Zn band structure of ZnO indicated that the base band of zinc oxide was 3.5ev [44-46]. At present, the mainstream TCO material in the market is ITO, but due to the scarcity and high cost of indium, the market continues to seek for other TCO as alternatives. The electrical properties of FTO and ITO make them emerge as new materials. On the other hand, ZnO film is relatively cheap, abundant and non-toxic, which make it have considerable potential as an alternative material for ITO.

2.2.3 Tungsten trioxide

The specific lattice structure is shown in figure 2.5. The optical band of tungsten trioxide is 2.62 eV, so the light with wavelength within the visible infrared light range is permeable. Research has shown that by doping oxygen vacancy [47] or chemical elements [48], it will introduce free electrons to tungsten oxide crystal, and changes electrical and optical properties of the produced oxides, and thus achieve high metal conductivity.

The oxygen vacancy of tungsten oxide results in forming a complex ordered structure called Magneli structure. Chemical elements doped tungsten trioxide can form tungsten bronze with a special oxygen octahedral structure of stoichiometric compounds (M_xWO_3, M = Na, Li, K, Rb, Cs), where M represents common alkali metals for doping elements, and the corresponding doping value is 0.33. This kind of tungsten bronze such as $Cs_{0.33}WO_3$, $Na_{0.33}WO_3$, etc., show excellent absorption

properties in the near infrared wavelength region [49]. They therefore can be substituted for traditional infrared absorption materials of ITO with a broad prospect of application and a high research value.
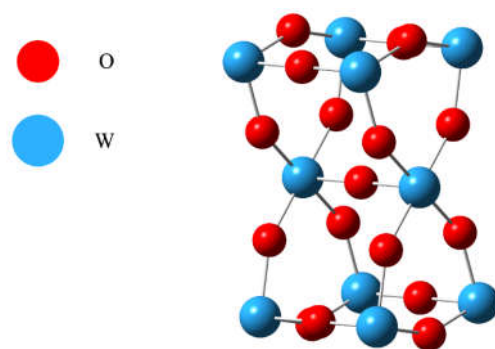
Figure 2.7 The crystal structure of tungsten trioxide

2.2.4 The preparation methods of transparent conductive oxides.

The preparation methods of transparent conductive oxide can be divided into physical and chemical methods. The common physical method is the physical deposition technology, that is to make the atoms evaporate, sputter and deposit into TCO films through the light and electricity on the material surface. Such synthetic methods mainly include Vacuum Evaporation, Magnetron Sputtering, pulse laser deposition (PLD), etc.

The chemical methods mainly include sol gel method (sol - gel), spray pyrolysis, saline solution of alcohol, chemical vapor deposition (CVD), direct precipitation, solvent hot method (hot water), microemulsion, and polymerization methods such as Pyrolysis [50-52].

The optical properties of transparent insulating coatings determine that the

required TCO materials are nanoparticles with small particle size, uniform distribution, and controllable shape, rather than thin films. Therefore, chemical methods are mainly used to prepare the TCO (transparent insulating coating).

2.3 Localized Surface Plasmon Resonance

2.3.1 Characteristics of localized surface plasma resonance

Surface plasmon resonance is first found in metallic materials. There are many free mobile electronics on the metal surface, and these free electrons produce a collective oscillation driven by the electromagnetic field introduced by the incident light, when the frequency of an incident light is same as that of the free electrons it will produce free electron resonance, this phenomenon is known as surface plasma resonance (SPR). The surface plasmon resonance causes a peak of the metal to have extinction effect on the incident light (light extinction = light absorption + light scattering), therefore, surface plasmon resonance is usually expressed as material for a certain wavelength of incident light to produce a large amount of absorption, produced corresponding absorption peak in the absorption spectrum. For nanoscale metal materials, the size of material is much smaller than the wavelength of the incident light, thus electronic oscillation on the Surface of the material is limited in the local area, then the surface of the nanometer metal plasma work is known as the local Surface Plasmon Resonance (Localized Surface Plasmon Resonance, LSPR) [58]. LSPR would also make a particular resonance absorption of metal nanostructures at certain wavelength of incident light. At the same time, LSPR will make the local area around nanostructures

light field which has been sharply increased due to the influence of size effect, and the phenomenon is known as the near field enhancement effect. Due to intense light absorption and near-field enhancement effect, the surface plasma resonance is widely used in surface enhanced Raman, optoelectronic devices, biological sensors to increase energy storage, chemical detection, solar cells, biological imaging and thermal treatment areas such as cancer.

In order to better explain the surface plasmon resonance of nanostructures, the Drude model presents the relationship between the dielectric function of materials and the incident light frequency [59]:

$$\varepsilon_\omega = \varepsilon_\infty - \frac{\omega_p^2}{\omega^2 + i\gamma\omega} \tag{2.2}$$

where ωp is collective electronic collective oscillation frequency, $\omega p2 = Ne2/(\varepsilon_0 m^*)$, ω for incident light frequency, γ for relaxation coefficient, ε_∞ is high frequency dielectric constant, N is concentration of material intrinsic carrier, e as the electron charge, ε_0 for vacuum dielectric constant, m^* is the effective electron mass. According to the model, the material's absorption of incident light depends on the collective oscillation of the electrons, and the formula is described as:

$$\sigma(\omega) = 9\frac{2\pi}{\lambda}\varepsilon_m^{3/2}\frac{Im[\varepsilon_{(\omega)}]}{\left(Re[\varepsilon_{(\omega)}] + 2\varepsilon_m\right)^2 + \left(Im[\varepsilon_{(\omega)}]\right)^2}V \tag{2.3}$$

From this formula, it can be seen that for a specific material,, ω_p is determined by the constant value of material itself, and the absorption of incident light for the material is not only related to materials, but also affected by the environment.

Based on the Drude model, we assume that the microstructure of metal nano-

materials is spherical, thus we can obtain the frequency of the plasma resonance in the

local surface of the material:

$$\omega_{sp} = \sqrt{Ne^2/\left(\varepsilon_0 m_\theta (\varepsilon_\infty + 2\varepsilon_m)\right)} \qquad (2.4)$$

and the wavelength of Plasma resonance:

$$\lambda_{sp} = 2\pi c/\omega_{sp} \qquad (2.5)$$

It can be seen from the formula that the resonant peaks of the nanostructured LSPR

are mainly determined by the carrier concentration of the material and the environment.

In fact, due to the influence of size effects, the shape and size of the material will also

affect the strength and peak position of LSPR. At the same time, the size of the material

should be much smaller than the incident light wavelength to ensure that the charge

resonance is concentrated in a certain local area.

2.3.2 Characteristics of local surface plasmon resonance in different nanostructures

Although the surface plasmon resonance properties were originally found in metal

materials, according to the above formula we can conclude that, surface plasmon

resonance properties are not confined to metal materials. Actually, when the

concentration of a carrier is high enough in material it can also produce surface plasmon

resonance, such as heavily doped semiconductor, semimetal nanometer materials, and

so on [60]. The LSPR peak position of various materials is shown in figure 2.7.

It can be seen from the figure that the LSPR peak position of precious metal

materials usually located at visible wavelengths due to the high carrier concentration,

usually greater $> 10^{22}\text{cm}^{-3}$. The carrier concentration of semimetal material is about $10^{21}\sim10^{22}\text{cm}^{-3}$, so its resonance peak position is within the visible light and near infrared region, and the carrier concentration of heavily doped semiconductor is about $10^{19}\sim10^{21}\text{cm}^{-3}$, and the resonance peak is located between the near infrared and the far infrared wave band. The LSPR characteristics of each three kinds of materials in precious metals materials have both advantages and disadvantages. Due to the high carrier concentration and mobility, the plasma resonance strength is very high, and can be processed by a variety of materials synthesis method to control the size and morphology of the precious metal nanometer materials and change the resonance peak position, so precious metal nanostructures are commonly used to enhance the performance of the uv/visible photoelectric device. But even through controlling the morphology and size, the peak position of surface plasmon resonance of precious metal is very difficult to be controlled to the other wave bands, and the cost precious metals is very high, thus its practical application therefore is limited [61]. Research about LSPR properties of semi-metallic materials is not much, they can be used in the near infrared communication, biological imaging and treatment of field and other fields because of a strong absorption in visible and near infrared band. However, their complex synthetic process and high cost also limit its application. For heavily doped semiconductor, the significant control of resonance peak position of can be realized by changing the doping concentration. Recently, many researchers have focused on its LSPR properties and application, which are widely used in enhanced infrared detectors,

infrared imaging, etc. However, the negative effects of doping defect on LSPR cannot be ignored. The doping process is usually complex, and will reduce the crystal quality of the material, which also affects the collective oscillation of the surface carrier. At the same time, the impurity atoms act as a scattering center, which greatly influences the migration of carrier and will greatly attenuate the intensity of the surface plasmon resonance [62].
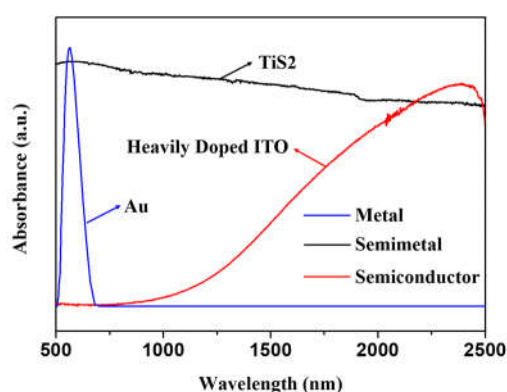
Figure 2.8 LSPR absorption peaks of various nanomaterials.

2.4 Thermal insulation mechanism of transparent insulation coating

2.4.1 The optical properties of transparent conductive oxides

In general, TCO materials are conductive, transparent in visible and near infrared light and can reflect thermal infrared radiation. For long wavelength region or far-infrared light, the reflection of TCO materials depends on the free electrons in the guide band. The absorption of TCO material is related to the optical band gap of the material in the short wavelength region, namely near infrared light region [63-65].

The optical properties of TCO materials can be reasonably explained according to

the Drude theory in the near infrared wavelength region. When light shines on the surface of the TCO semiconductor material, the free electrons produce polarization through interaction within the material due to the presence of the light magnetic field. On the other hand, the electrical properties of TCO films, such as carrier mobility and carrier density, determine the absorption of light in the far-infrared wavelength region. This absorption characteristic is caused by the free electrons of the TCO semiconductor materials and called the plasma frequency. The TCO material has been widely used in insulating glass materials due to this plasma edge [66-69].

The Drude theory of conductive metal can explain this phenomenon well. As mentioned in the previous article, light irradiation on TCO semiconductor material would cause the interaction of free electrons within the material to produce polarization, and the result affects the dielectric constant ε. The four basic hypotheses of the Drude theory are as follows:

(1) Independent electron approximation: to ignore the interaction between electronics, approximately assume that electronic movement is independent on each other, like isolated individual electrons, which is also known as single electron approximation.

(2) Free electron approximation: use a classic example of collision image to simplify the complex interaction between electrons and ions, and approximately assume that individual electrons freely move between two

successive times of collision with ions, so the conduction electrons in the metal are commonly referred as free electrons.

(3) Relaxation time approximation: collision probability between electrons and ions shall be the dt/tau in the dt time, including tau relaxation time: average free time between two times of collision of ions and electrons. No matter how closed they are before the collision, the statistical distribution of the electron velocity will be restored to the equilibrium state after the real collision, and it is approximately assumed that the electrons will recover to the equilibrium state after a relaxation time.

(4) The classic approximation: this is the motion of the electrons between the two successive ions following Newton's laws of motion. Plus, the electrons follow the Boltzmann statistical distribution before and after the collision.

Figure 2.8 shows the transmission, reflection and absorption spectra of typical TCO materials, which can be divided into three characteristic regions. First of all, the transparent conductive oxides are in visible area (argument lambda = 380 ~ 780 nm, h = 3.1 ~ 1.7 eV). Secondly, the incident light will be absorbed in the bandgap transition if its energy is greater than the optical band gap of TCO materials, which suggests that the transmittance in the short wavelength decreases sharply and absorption rate rises sharply (lambda < 350 nm, h argument > 3.5 eV). Therefore, as mentioned above, a typical TCO material must have an optical band greater than 3.2 eV. Finally, in the wavelength region> 1500 nm, there will be a sharp decrease in transmittance and a

sharp increase in reflectivity. In the process, if the absorption rate achieves the maximum at a particular point, which is known as the plasma wavelength λp, the corresponding oscillation frequency is called the frequency of the plasma oscillation. The frequency of the incident light at that point is equal to the electron collective oscillation frequency of the material [70-72]. The oscillations in the electric field component of the incident light would result in the absorption of light.
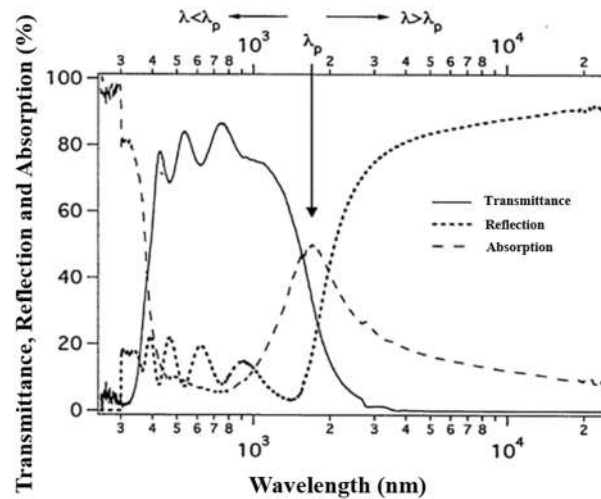
Figure 2.9 Transmission, reflection, and absorption spectra of a typical TCO

To sum up, when λ < λp, namely the incident light frequency ω > ωp, wave function is in the shape of wave motion and carrier inhibits the electrons movement due to the inertial mass acceleration, which also explains why electrons can't rapidly shield the electric field of the incident light and thermal radiation can pass through it . The results show that when λ > λp, namely ω < ωp ,the wave function begins to decay: omega electrons in the material with speed fast enough to shield the electric field of the

incident light and the thermal radiation cannot spread; When λ=λp, the result is the absorption of incident light [73].

A model is established for the plasma resonant frequency, assuming the average displacement of the carrier is ex, then the polarization P is introduced.

$$P = N_e ex \tag{2.6}$$

where, Ne is the free carrier density, e is the free carrier charge, and x is the average displacement. P is the negative recovery resistance of carrier. For P, there is the following relation:

$$\frac{-P}{\varepsilon}e = \frac{md^2x}{dt^2} = \frac{-N_e ex}{\varepsilon}e \tag{2.7}$$

calculate the average displacement x according to the equation:

$$x = A\exp\left\{\left(\frac{N_e e^2}{m_e \varepsilon}\right)t\right\} = A\exp\left(\omega_p^2 t\right) \tag{2.8}$$

$$\omega_p = \sqrt{\frac{N_e e^2}{m_e \varepsilon}} \tag{2.9}$$

According to the Drude model, the conductivity is:

$$\sigma = (N_e e)\left(\tau \frac{e}{m_e}\right) \tag{2.10}$$

The effective quality of the electron is used to measure the effect of carrier obstruction, so:

$$\omega_p^2 = \frac{\sigma}{\varepsilon\tau} = \frac{N_e e^2}{m_e \varepsilon} \tag{2.11}$$

These formulas reflect the interrelation between the electrical properties and optical properties of TCO materials. According to the above formulas, the carrier concentration can be concluded. Ne has a balance between the visible transmittance and conductivity of TCO materials. On the one hand, the conductivity of TCO

semiconductor materials is positively correlated with the carrier concentration Ne, so it needs to be as high as possible to maintain the highest possible conductivity. On the other, with the increase of carrier concentration of Ne, plasma resonance frequency rises as well, thus the plasma wavelength λp will shift, when it arrives at the edge of the near infrared ($\lambda p > 780$ - nm), carrier concentration reaches the maximum, where the TCO in the range of visible light passes through to achieve near infrared absorption and infrared reflection. Studies show that the carrier concentration cannot be greater than 2.6×10^{21} cm-3 [74] in order to ensure the visible light of TCO material with high conductivity.

To sum up, transparent conductive oxides are the key factors to ensure transparent heat insulation coating to reflect and absorb infrared light so as to achieve heat insulation effect, choosing suitable transparent conductive oxides for transparent insulation coating is very significant to be studied.

2.4.2 The special properties of nano - transparent conductive oxides

In the field of material science, materials of particle size between 1~100 nm are nanomaterials. Nanomaterials have distinct physical and optical properties that are different from those of large size materials. For nano-level transparent conductive oxides, the particle size determines the selective absorption characteristics for the solar spectrum. Only when TCO's particle size is less than the wavelength of visible light, the nano dispersion system can guarantee the transmission of visible light.

The total shielding area A of transparent conductive oxide materials is as follows:

$$A = \pi r^2 \frac{M/\rho}{4\pi r^3/3} \qquad (2.12)$$

It can be seen that the smaller the particle size is, the larger the surface area is, and the larger the total shielding area A is. At the same time, with the decrease of r, the decrease of electron density will lead to the decrease of sunlight absorption shielding effect. Therefore, the particle size r of nano-transparent conductive oxide can only be controlled within a certain range to maintain a good visible light transmittance and high near-infrared absorption [75].

2.5 Literature review of resins coating

2.5.1 Introduction of paint

Coating is a kind of material that protects and decorates the surface of an object. Specifically, coating is coated on the surface of the object, and after drying it will form a thin film, which is used for the protection, beautification or other functions for the object [76]. In terms of composition, the coating generally consists of four components: film-forming material (also mainly film material), solvent (dispersion medium), filler (secondary film material) and various coating additives.

The filler is the secondary material of the coating, it is also an integral part of the coating, which cannot leave the forming matter to make up the coating alone. Filler is the demonstration of the function of coating. For ordinary coatings, fillers can provide them with paint color, Anti-rust, wear-resisting and other functions. For transparent insulation coatings, the fillers are TCO nanomaterials, which can absorb and shield infrared light to achieve thermal insulation effect.

The solvent is to dissolve or disperse the film material and fillers in the coating, to meet the requirement of various coating technological process, with the dosage of about 50% (volume fraction). After coating film formed, the solvent does not remain in the paint film, but volatilizes completely.

Assistant addictive: To visualize this, the role of additives in coatings, is equivalent to the role of vitamins and trace elements in human body, little dosage about 0.1% (mass fraction) has very tremendous and indispensable effect. Modern paint additives are mainly divided into four categories: 1. Auxiliary agents for the production of coatings, such as defoaming agents, wetting agents, dispersants, emulsifiers, etc.;2. Auxiliaries for the action of coating storage, such as anti-sinking agent, stabilizer, anti-skinning agent, etc.;3. Auxiliaries for the coating construction process, such as leveling agent, defoaming agent, drier, etc.;4. Auxiliary agents for coating performance, such as plasticizer, antigloss agent, flame retardant and viscosifier, etc.

Coating forming material is a kind of polymer compound, namely resin. There are two kinds of natural macromolecules and synthetic polymers, where synthetic polymers are dominant.

For the solvent of paint, because it is volatile, it is easy to cause great pollution to the environment, and it also causes a great waste of resources. However, because of the very obvious superiority of waterborne coating, modern coating industry gradually focuses on waterborne development, the current waterborne coating is mainly water dispersive system, and the aqueous solution system is not enough. The composition of

waterborne coating is made up of three parts including water - based resin, filler, and auxiliary agents. The waterborne resins include water dispersion of polyurethane, waterborne acrylic resin, waterborne alkyd resin, waterborne polyester resin, waterborne epoxyresin, waterborne amino resin, etc. Consideration of choosing resins for coating is mainly based on the structure property of resins, properties of matrix material, environment and cost [77-79].

2.5.2 Mechanism of coating formation

Coating process can be divided into physical process and chemical process. For the physical process, it is mainly for polymer resins with high molecular weight. These resins can provide good flexibility and stability, and their glass transition temperature should be higher than the room temperature to ensure adequate hardness and resistance to scratch. With the polymer resin coatings can be prepared for water solution or organic solvent solution, dispersion liquid. Next in the coating-forming process, water or organic solvent evaporate to leave polymer coating with stable chemical properties.

The chemical coating contains adhesive component, which is micromolecular and formed by crosslinking after drying. These adhesives have a relatively low molecular weight so that the coating solution can achieve high solid content with low viscosity. Reactions such as of polymerization, polyaddition and polycondensation will happen in the process of chemical forming [80].
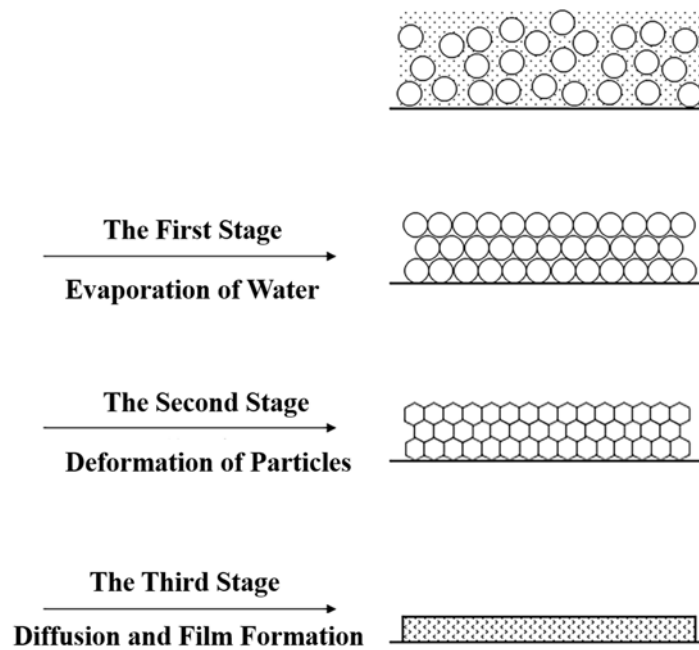
Figure 2.10 Latex film forming progress

Polymer emulsion is a kind of dispersing system in which solids are dispersed in water by polymer resin. The forming process of polymer emulsion coating is generally divided into three phases, as shown in figure 2.9: firstly, with the water molecules evaporating from the decentralized system, colloidal particles become more concentrated and close to each other, the gap latex particles filled with water and water-soluble substance; Then, as more water evaporated, the protective layer of rubber latex particles is destroyed, and the clearance between the colloid particles are increasingly closed until the capillary formation, the capillary forces latex particles to gradually form a dodecahedron diamond, until the interface between the particles disappears; In the final stage of coating process, the polymer diffuses across the boundary of the whole grain, increases the strength of the coating and eventually forms continuous and even latex coating layer [81-83].

2.5.3 Selection rules of coating-forming resin

It is necessary to prepare the coating forming agents for transparent insulating coatings. On the one hand, it should meet the current needs of society and trends of environmental protection. On the other hand, it should achieve the basic properties of the insulating coating itself. Generally, the selection of coating forming agents should meet the following conditions:

(1) As the transparent thermal insulating coating, the requirement on transparency of resin is very high. At least 80% of visible light transmittance of the resin matrix can only be qualified;

(2) Transparent heat insulating coating is widely used in the glass walls and auto glass, so the resin coating agents should have good performance on stain resistance, weather resistance, scratch resistance, sunlight and other complex outdoor climate conditions such as wind and rain;

(3) To improve the insulation effect of transparent insulation coating, resin coating agents should absorb radiation energy as little as possible, Namely resin macromolecules contain energy-absorbing functional groups as little as possible, such as - OH, C = O, O - C - C, etc.

Two kinds of commonly used coatings are described as below.

2.5.4 Waterborne polyurethane

Polyurethane resin can be divided into oil polyurethane and waterborne polyurethane. In the early society, solvent - based polyurethane, or oil polyurethane, was widely used, and a major forming agent in coatings. In the 1950s, waterborne

polyurethane began to enter the coating industry and the public's awareness. In the 1960s and 1970s, the waterborne polyurethane developed rapidly and was largely studied. In the 1970s, waterborne polyurethane was used in industrial production, mainly in leather finishing agents. In the 1990 s, environmental protection concept gradually became deeply rooted in the hearts of the public, more and more products began to attach importance to environmental friendly water-based polyurethane. It is applied in coatings, adhesives and other fields, gradually replaces solvent- based polyurethane and occupies the market. Waterborne polyurethane has become a research hotspot of modern water-based resins and one of the representatives of excellent resin forming agents [84].

Waterborne polyurethane coatings, which is to take water as dispersion medium, for preparation of waterborne polyurethane resin as coating, has advantages such as security, environmental protection, energy saving, stability, low toxicity, low VOC, etc. At the same time, it is featured in high hardness, good wear resistance, flexibility, adhesion and other excellent properties of oil polyurethane [85-87].

Although waterborne polyurethane is widely used in coatings, there are some defects in the performance. Hydrophilic groups exist in the waterborne polyurethane structure, so the water resistance and solvent resistance are poor. Aiming at this problem, the current domestic and international efforts are to improve the water resistance, solvent resistance and other properties of the materials through the modification of waterborne polyurethane. The common methods are physical and chemical methods,

such as blending, forming interpenetrating polymerization networks, grafting, and embedding other polymer materials.

2.5.5 Water-based acrylic resin

Acrylic resin, acrylate, methyl acrylate and vinyl monomers such as styrene copolymer, acrylic resin coatings based on acrylic resin as coating formers, also can be divided into two categories, water-based and oil-based .The research and application of waterborne acrylic resin began in the 1950s and developed rapidly in the 1970s.Water-based acrylic resin, which is low cost and has less energy consumption, safety for use and low pollution to the environment, and therefore replaces the traditional solvent-based coating, is current mainstream development direction of the acrylic resin.   At present, water-based acrylic resin paint is water-based paint series of varieties, most for the fastest growing environment friendly coating. According to disperse system classification, some water-based acrylic resin with acrylic resin, acrylic resin emulsion and aqueous acrylic resin and the emulsion are the most mature technologies. Acrylic emulsion can be divided into pure acrylic emulsion, styrene-acrylic emulsion, acetate-acrylic emulsion, silicone emulsion and fluorocarbon emulsion, in the terms of monomers, etc. [88].

Among them, the styrene acrylic emulsion is widely used in coating, adhesive, due to the good weather resistance, low pollution, non-toxic and other characteristics, but there are still some problems in practical applications, such as poor water resistance and minimum film-forming temperature. In recent years, the research of modified

styrene-acrylic emulsion has been widely concerned. The modification methods of styrene-acrylic emulsion mainly include epoxy resin modification, organic silicon modification, polyurethane modification, organic fluorine modification, crosslinking modification, etc.

2.6 Common dispersion methods for nano powder

In order to guarantee the basic properties of the coating and transparent heat insulation effect, functional nanoparticles in the transparent heat insulation coating need to be well dispersed in coating dispersion medium. Therefore, it is very important to reduce the agglomeration caused by surface activity of nanometer powders.

The reasons for the reunite of nanometer powders are mainly divided into soft and hard reunite. the Agglomeration of nanoparticles caused by Van der Waals force and coulomb force is called soft agglomeration, which is easy to be destroyed, and can be eliminated by means of ultrasonic stirring, mechanical stirring, grinding and other physical means. The formation of hard agglomeration is mainly due to the effect of chemical bonds, which is the main reason for the dispensability of nano-dispersive system. Physical and chemical methods can be used to solve hard agglomeration and improve dispensability of nanoparticles in dispersed systems. The physical method is to improve the dispersion stability by means of various mechanical dispersion methods such as ball milling, sand grinding, mechanical stirring, ultrasonic stirring, etc. The chemical ways are modified by adding surfactants, coupling agents and so on to reduce the surface energy, increase the interparticle resistance and neutralization surface

charge [89-92].

2.6.1 The dispersion process of nano powder

The dispersion of nanometer powder includes the following three processes:

（1） wetting process. After the powder enters the dispersed system, the surface air is replaced by the liquid.

（2） The process of dispersing and destroying reunite. Large size particle of powders is dispersed to small size by physical means such as ball milling and ultrasonic dispersion.

（3） The stabilization processes. By means of physical and chemical, the powders are prevented from reuniting, and are kept stalely dispersed for a long time.

The above three processes are not in completely a sequence, but almost synchronous.

2.6.2 Physical methods to disperse nano powder

The physical dispersion methods of nanometer powders mainly include ball milling, ultrasonic wave and high- speed stirring.

（1） Ball milling dispersion method: According to the required particle size, the zirconia beads with different particle sizes are selected, and the properties of which are stable and do not react with the nano powder. The dispersion and stability of nano-powders in the system are improved by means of the

rolling of zirconia beads and the rolling and collision of zirconia beads and ball grinding tanks.

(2) Ultrasonic dispersion: Under the action of sound waves, the tiny vesicles in the liquid are activated, producing the dynamic processes of oscillation, growth, contraction and collapse. And this phenomenon is called hypercavitation [93]. Ultrasonic dispersion method is to use ultrasonic cavitation to disperse nano powder. In a short period of time, the bursting of bubble will produce high temperature and high pressure in small space around and the temperature will change extremely quickly, resulting in a strong shock wave and high-speed jet stream. These external factors can destroy the van der Waals force between the aggregates, and then disperse the nanoparticles uniformly in the dispersed medium [94].

(3) High speed mechanical stirring: It is used to produce high strength shear force through high speed mechanical stirring above 8000 RPM, thus dispersing nano-aggregates and reducing particle size. The key point of this dispersive method is not the length of time, but the speed of mechanical stirring, or the shear force.

2.6.3 Chemical dispersion methods of nano powders

The chemical dispersion methods of nano powder mainly includes adding surfactants, esterification reaction, coupling agents and so on.

（1）	surface active agents: Adding surface active agents in the dispersion system, which can help to form a coating layer absorbed on the surface of nano powder and particles by intermolecular forces including hydrogen bonding, van der Waals force, to reduce the surface tension and prevent the reunion between the nano powder.

（2）	Esterification reactions: Through the esterification between metal oxide and alcohol, the hydrophilic of the nano powders is transformed, and the dispersive effect can be improved as well.

（3）	Coupling agent method: Common coupling agents include silane coupling agent, phthalate coupling agent and aluminum acid coupling agent. Functional groups of coupling agent molecular can band with which of nano powder surface, by means of physical winding and polymer reaction of nano powder surface modification, thus to improve the dispersion effect of nano powder.

2.7 Research   progress of transparent thermal insulation coatings

At present, the United States, Japan and other countries have published a large number of patents on transparent insulation coatings [95]. However, In China, the development of transparent thermal insulation coatings started late, although some research achieved in the academic field, the market application is still immature.

Nanophase Technologies Corporation in America mainly prepares all kinds of transparent conductive oxide nanoparticles aqueous dispersion and oily dispersion,

based on the preparation to produce multifunctional coating with properties of ultraviolet infrared shielding, thermal insulation, transparence, abrasion resistance. As early as in 2000, the company produced ITO nanoparticles particle which size is less than 44 nm, using physical vapor phase method, putting this nanoparticles into dispersion can be directly added into coating; Three-arrow company in Japan has developed a transparent thermal insulating coating, which has been widely used in the market to reduce the energy consumption of building glass. The coating produced by the company can filter out solar radiation without affecting the lighting, and it can shield up to 68 percent of infrared light and 95 percent of uv light. Nanomag company of South korea produced NMAS-Series of ATO, ITO and TiO2 sol, which have been widely used in building glass, automotive glass, medical equipment and electronic display screens. Germany also developed thermal insulating coating to meet the demand of light and heat insulation, the coating can absorb the sun's light energy and transform it into heat energy, then heat energy being sent out so as to achieve heat preservation, heat insulation, and other functions.

The core of transparent insulation coating is the research of nano- transparent conductive oxides. Because of the high price of indium in ITO (indium doped tin oxide), the search for other nano-functional materials that can replace ITO has become a hot topic in current research. Nowadays, ATO (antimony doped tin oxide) is the most widely used transparent conductive oxide. In addition, AZO (aluminum doped zinc oxide) doped with zinc oxide has been further studied due to its excellent near-infrared

shielding characteristics. In recent years, many researchers have studied transparent insulation coating related with tungsten bronze, which is mainly in trioxide of the tungsten bronze (MxWO3, M = Li, Na, K, Rb, Cs) and has higher shielding absorption characteristics in near infrared wave band,

Antimony doped tin oxide (ATO): Feng [96] prepared ATO/WPU composite coating, through the unique surface mould pressing method, which modified membrane structure into a lotus- leaf structure with hydrophobic structure performance, and finally made a coating with performance combined super hydrophobic and heat insulation. Wang et al [97] used ATO nano filler, silica polymer for resin matrix to composite and the prepared a type of transparent insulation coating, and one of the graft silica polymer was made by silica sol crosslinking reaction of KH570. The obtained organic/inorganic hybrid silicon nanocomposite coating has good infrared shielding effect and mechanical properties, which can reach 80% of the visible light transmittance and less than 6% fog degree. Li [98] et al. prepared ATO by using a frozen gel method, which was made by freeze-dried gel precursor and then calcined at high temperature. Research about the effects of Sb doping on optical properties were investigated, resulted that the optimum optical performance, conductivity and particle size were obtained by 10% doping. Lu [99], based on the preparation of ATO by hydrothermal method, combines TiO2 with it to prepare glass coatings to achieve both transparent insulation and self-cleaning characteristics. Li [100] et al prepared the ATO nano-mesoporous microspheres by hydrothermal method and prepared the thermal shielding transparent membrane

structure. In the process of preparation, methanol was used as the reaction solvent, and PVP polyvinylpyrrolidone was added as well. This mesoporous microsphere has a low thermal conductivity, so it enhances the effect of transparent insulation furtherly.

Aluminum doped zinc oxide (AZO): Buonsanti [101] used hydrothermal method to prepare AZO transparent conductive oxide and examined the influences of the mixed amount of aluminum (0 ~ 8%), and particle size (5 ~ 20 nm) to the optical performance, and the heat insulation effect. Li [102] et al. used AZO as a nano-filler and epoxy resin as the resin matrix to prepare transparent insulating coating. Research shows that when 6% as the doping amount, 600 °C for calcination conditions, the resulted AZO would have the best optical properties and particle size. When the quality score of AZO is 0.5wt.%, 50% of visible light transmittance and 0.45 shading coefficient can be achieved. Soumya[] et al prepared a transparent insulating coating with PMMA methyl methacrylate as resin matrix and AZO as functional filler， which had an average particle size of 261 nm and a coating thickness of 269 nm. When AZO doping at a amount of 2%, mass fraction of 0.7 wt. %, the surface temperature of coating glass can be reduced from 52.6 °C to 41.9 °C.

Tungsten bronze (MxWO3): In 2007, Takeda [103] proposed that the tungsten bronze system had special optical properties, and his system analyzed the infrared absorption characteristics of the tungsten bronze system. Experiments were conducted by heating alkali salt and WO3NH3 at 130 °C for 8 h, then put the mixture in hydrogen/nitrogen mixture environment under 550 °C heating for 1 h, and next for

calcination, at 800 ℃ in nitrogen environment for1 h, to get various types of doped tungsten bronze powder. Studies have shown that the produced M0.33WO3 (M=Li, Na, K, Rb, Cs) of 0.33 has very good near infrared absorption. Guo, [104] carried on the thorough research of tungsten bronze system, they used a controlled high temperature hydrothermal method to prepare the nanometer rod Cs0.33 WO3, K0.33 WO3 and Rb0.33 WO3, and conducted a comprehensive system of optical properties, such as morphology analysis and characterization. The prepared tungsten bronze got high visible light transmittance and excellent near-infrared absorption efficiency. Moon [105] et al prepared the tungsten bronze Na0.11Cs0.22WO3 with doped two elements. The size of particle is 80~120 nm, and the near infrared absorption rate can be controlled between 60% and 80%. Zhao et al [106] using WCl6 and CsOH reactants successfully synthesized cesium tungsten bronze by hydrothermal method, the synthetic method is simple and safe, and it didn't need harsh high temperature reaction conditions and dangerous inert gas environment. Zhanjun PENG synthesized Cesium tungsten bronze powder by hydrothermal synthesis in the citric acid solution using cesium carbonate and sodium tungstate as raw materials.

Other transparent conductive oxides: in 2016, Zhong [107] et al. prepared a relatively inexpensive nano-cus nanoparticle. As a new type of nano-infrared absorbing material, this material was synthesized by simple hydrothermal method, with the particle size at a range of 150~250 nm, and the minimum coating thickness was 30 nm. And study showed that 0.8mm of the coating could shield 78.1% of the near infrared

light while maintaining the visible transmittance of 63.0%. Adachi [] et al. studied and investigated the optical absorption characteristics and scattering behavior of LaB6 dispersion system with different particle sizes. Research had shown that near infrared absorption properties of LaB6 originated from the surface plasma resonance (LSPR), proving that LaB6 had the application prospect being used as near infrared absorption material for transparent heat insulation coatings and solar filter. After that, Chen [108] et al. prepared the high purity LaB6 by carbonization boron reduction method，which furtherly promote the development of LaB6.

2.8 Brief summary

In the building structures, glass has the highest total heat transfer coefficient (u-values), and approximate 60% of the heat loss is attributed to the glass structures of the building. Therefore, in order to reduce energy consumption in buildings, it has always been a hot research topic to improve the thermal insulation efficiency of glass itself. At present, the main energy-saving glass technology in the market, such as heat-absorbing glass, thermal insulating glass, vacuum glass, low-e coating glass, heat-insulating laminated glass. Thermal insulation coated glass and so on. The visible light transmittance of the absorbing glass itself is too low, which is not conducive to market application. The service life of thermal insulating glass is short, and moisture condensation and frost formation are prone to occur inside. Vacuum glass technology is very difficult, and the application is not popular. Low-E's light pollution problem and expensive cost limit its further promotion and application; Thermal insulation

laminated glass is prone to rupture, bubble formation and other problems, so that the application of laminated glass is limited to automotive glass, and the application of building glass is very few.

As a new type of building energy saving glass, the insulating film glass made by transparent insulation coating gradually entered people's daily life. This type of insulating coating glass has a controllable high visible light transmittance (50%~90%), which correspondingly has a very high shielding effect on near-infrared light and ultraviolet light. The coating is composed of nano-inorganic Transparent Conductive Oxide (TCO) and polymer organic resin. The transparent insulation coating is able to maintain 80% of the visible light transmittance while absorbing most of the near infrared light, thus achieving good thermal insulation energy saving effect. The production process of transparent insulation coating is simple, the required production equipment such as sanding machine and water kettle, polyurea are cheap, on the other hand, the construction method of transparent insulation coating is concise, staff training cycle is short. These advantages indicate the great application prospect and technology development potential of the transparent insulating coating in the future of energy-saving glass technology

2.9 Reference

[1] Energy Information Administration (US), & Government Publications Office (Eds.). (2016). *International Energy Outlook 2016: With Projections to 2040*. Government Printing Office.

[2] Chow, T. T., Li, C., & Lin, Z. (2010). Innovative solar windows for cooling-demand climate. *Solar Energy Materials and Solar Cells*, *94*(2), 212-220.

[3] Cuce, E., & Riffat, S. B. (2015). A state-of-the-art review on innovative glazing technologies. *Renewable and sustainable energy reviews*, *41*, 695-714.

[4] Bielert, F., & Stamm, G. (1994). Influence of quantized vortex lines on the stability of Taylor-Couette flow in He II. *Physica B: Condensed Matter*, *194*, 561-562.

[5] Sirinukunwattana, K., Pluim, J. P., Chen, H., Qi, X., Heng, P. A., Guo, Y. B., ... & Böhm, A. (2017). Gland segmentation in colon histology images: The glas challenge contest. *Medical image analysis*, *35*, 489-502.

[6] Shepovalova, O. V., Durnev, D. A., Chirkov, A. V., & Chirkov, S. V. (2017). High Vacuum Glass Units Application for Solar Radiation Thermal Conversion. *Energy Procedia*, *119*, 995-1002.

[7] Veerasamy, V. S., & Bracamonte, M. D. (2018). *U.S. Patent Application No. 15/725,475*.

[8] Henmi, H., Shoji, S., Shoji, Y., Yoshimi, K., & Esashi, M. (1994). Vacuum packaging for microsensors by glass-silicon anodic bonding. *Sensors and Actuators A: Physical*, *43*(1-3), 243-248.

[9] Cheng, Y. T., Hsu, W. T., Najafi, K., Nguyen, C. C., & Lin, L. (2002). Vacuum packaging technology using localized aluminum/silicon-to-glass bonding. *Journal of Microelectromechanical Systems*, *11*(5), 556-565.

[10] Ardakan, A. M., Sok, E., & Niemasz, J. (2017). Electrochromic glass vs. fritted glass: an analysis of glare control performance. *Energy Procedia*, *122*, 343-348.

[11] Ghosh, S. S., Biswas, P. K., & Neogi, S. (2017). Thermal performance of solar cooker with special cover glass of low-e antimony doped indium oxide (IAO) coating. *Applied Thermal Engineering*, *113*, 103-111.

[12] Cuce, E., Young, C. H., & Riffat, S. B. (2015). Thermal performance investigation of heat insulation solar glass: a comparative experimental study. *Energy and buildings*, *86*, 595-600.

[13] Zeng, L., & Chen, N. (2015). Bayesian hierarchical modeling for monitoring optical profiles in low-E glass manufacturing processes. *IIE Transactions*, *47*(2), 109-124.

[14] Cuce, E., Young, C. H., & Riffat, S. B. (2014). Performance investigation of heat insulation solar glass for low-carbon buildings. *Energy conversion and Management*, *88*, 834-841.

[15] Cuce, E. (2016). Toward multi-functional PV glazing technologies in low/zero carbon buildings: Heat insulation solar glass–Latest developments and future prospects. *Renewable and Sustainable Energy Reviews*, *60*, 1286-1301.

[16] Cuce, E., Young, C. H., & Riffat, S. B. (2015). Thermal performance investigation of heat insulation solar glass: a comparative experimental study. *Energy and buildings*, *86*, 595-600.

[17] Liu, J., Chen, B., Fan, C., Shi, F., Ran, S., Yang, J., ... & Liu, S. H. (2018). Controllable synthesis of small size Cs x WO 3 nanorods as transparent heat insulation film additives. *CrystEngComm*, *20*(11), 1509-1519.

[18] Kim, H. J., Lee, H. J., & Kim, D. S. (2018). Hollow TiO2 flake prepared from TiO2 coated glass flake for solar heat protection and their thermal performance. *Materials & Design*, *150*, 188-192.

[19] Hansen, T. K., Bjarløv, S. P., Peuhkuri, R. H., & Harrestrup, M. (2018). Long term in situ measurements of hygrothermal conditions at critical points in four cases of internally insulated historic solid masonry walls. *Energy and Buildings*, *172*, 235-248.

[20] Bremser, W., Ressel, J., & Reicher, J. (2018). *U.S. Patent No. 9,944,823*. Washington, DC: U.S. Patent and Trademark Office.

[21] Bozzoli, F., Mocerino, A., Rainieri, S., & Vocale, P. (2018). Inverse heat transfer modeling applied to the estimation of the apparent thermal conductivity of an intumescent fire retardant paint. *Experimental Thermal and Fluid Science*, *90*, 143-152.

[22] Qu, J., Song, J., Qin, J., Song, Z., Zhang, W., Shi, Y., ... & Xue, X. (2014). Transparent thermal insulation coatings for energy efficient glass windows and curtain walls. *Energy and Buildings*, *77*, 1-10.

[23] Enríquez, E., Fuertes, V., Cabrera, M. J., Seores, J., Munoz, D., & Fernández, J. F. (2017). New strategy to mitigate urban heat island effect: Energy saving by

combining high albedo and low thermal diffusivity in glass ceramic materials. *Solar Energy*, *149*, 114-124.

[24] Mallick, A., & Basak, D. (2018). Revisiting the electrical and optical transmission properties of co-doped ZnO thin films as n-type TCOs. *Progress in Materials Science*.

[25] Bivour, M., Schroeer, S., Hermle, M., & Glunz, S. W. (2014). Silicon heterojunction rear emitter solar cells: Less restrictions on the optoelectrical properties of front side TCOs. *Solar Energy Materials and Solar Cells*, *122*, 120-129.

[26] Lu, Y. B., Yang, T. L., Ling, Z. C., Cong, W. Y., Zhang, P., Li, Y. H., & Xin, Y. Q. (2015). How does the multiple constituent affect the carrier generation and charge transport in multicomponent TCOs of In–Zn–Sn oxide. *Journal of Materials Chemistry C*, *3*(29), 7727-7737.

[27] Ch, S. R., Zhang, L., Kang, T., Lin, Y., & Qiu, Y. (2018). Annealing impact on the structural and optical properties of electrospun SnO2 nanofibers for TCOs. *Ceramics International*, *44*(5), 4586-4591.

[28] Hoang, N. L. H. (2017). Electrical Properties Of Nb-Doped TiO2 Thin Films Deposited By Co-sputtering Process. *VNU Journal of Science: Mathematics-Physics*, *33*(3).

[29] Raghupathy, R. K. M., Kühne, T. D., Felser, C., & Mirhosseini, H. (2018). Rational design of transparent p-type conducting non-oxide materials from high-throughput calculations. *Journal of Materials Chemistry C*, *6*(3), 541-549.

[30] Sun, H., Yazdi, M. A. P., Ducros, C., Chen, S. C., Aubry, E., Wen, C. K., ... & Billard, A. (2017). Thickness-dependent optoelectronic properties of CuCr0. 93Mg0. 07O2 thin films deposited by reactive magnetron sputtering. *Materials Science in Semiconductor Processing*, *63*, 295-302.

[31] Lyubchyk, A., Vicente, A., Alves, P. U., Catela, B., Soule, B., Mateus, T., ... & Martins, R. (2016). Influence of post-deposition annealing on electrical and optical properties of ZnO-based TCOs deposited at room temperature. *physica status solidi (a)*, *213*(9), 2317-2328.

[32] Lu, Y. B., Yang, T. L., Ling, Z. C., Cong, W. Y., Zhang, P., Li, Y. H., & Xin, Y. Q. (2015). How does the multiple constituent affect the carrier generation and charge transport in multicomponent TCOs of In–Zn–Sn oxide. *Journal of Materials Chemistry C*, *3*(29), 7727-7737.

[33] Garg, V., Sengar, B. S., Awasthi, V., Kumar, A., Singh, R., Kumar, S., ... & Mukherjee, S. (2018). Investigation of dual-ion beam sputter-instigated plasmon generation in TCOs: A case study of GZO. *ACS applied materials & interfaces*, *10*(6), 5464-5474.

[34] Laflamme Janssen, J., & Gonze, X. (2015). Accurate effective masses from first principles. *Bulletin of the American Physical Society*, *60*.

[35] Tsukahara, T., & Wada, T. (2016). Immunotherapy for osteosarcoma. In *Osteosarcoma* (pp. 31-41). Springer, Tokyo.

[36] Ruske, F., Schönau, S., Ring, S., Neubert, S., Stannowski, B., Sittinger, V., ... & Rech, B. (2014, March). Material properties of high-mobility TCOs and application to solar cells. In *Oxide-based Materials and Devices V* (Vol. 8987, p. 898723). International Society for Optics and Photonics.

[37] Balakrishnan, G., Vinoba, J. S., Rishaban, R., Nathiya, S., & Ghosh, O. S. (2018). Microstructural and Properties of P-type Nickel Oxide (NiO) Thin Films Deposited by RF Magnetron Sputtering. *Advanced Science Letters*, *24*(8), 5866-5871.

[38] Siegl, S. J., Dzijak, R., Vázquez, A., Pohl, R., & Vrabel, M. (2017). The discovery of pyridinium 1, 2, 4-triazines with enhanced performance in bioconjugation reactions. *Chemical Science*, *8*(5), 3593-3598.

[39] Lou, X. W., Wang, Y., Yuan, C., Lee, J. Y., & Archer, L. A. (2006). Template-free synthesis of SnO2 hollow nanostructures with high lithium storage capacity. *Advanced Materials*, *18*(17), 2325-2329.

[40] Paek, S. M., Yoo, E., & Honma, I. (2008). Enhanced cyclic performance and lithium storage capacity of SnO2/graphene nanoporous electrodes with three-dimensionally delaminated flexible structure. *Nano letters*, *9*(1), 72-75.

[41] Lou, X. W., Li, C. M., & Archer, L. A. (2009). Designed synthesis of coaxial SnO2@ carbon hollow nanospheres for highly reversible lithium storage. *Advanced Materials*, *21*(24), 2536-2539.

[42] Law, M., Kind, H., Messer, B., Kim, F., & Yang, P. (2002). Photochemical sensing of NO2 with SnO2 nanoribbon nanosensors at room temperature. *Angewandte Chemie*, *114*(13), 2511-2514.

[43] Gondal, M. A., Drmosh, Q. A., Yamani, Z. H., & Saleh, T. A. (2009). Synthesis of ZnO2 nanoparticles by laser ablation in liquid and their annealing transformation into ZnO nanoparticles. *Applied surface science*, *256*(1), 298-304.

[44] Yang, L. Y., Feng, G. P., & Wang, T. X. (2010). Green synthesis of ZnO2 nanoparticles from hydrozincite and hydrogen peroxide at room temperature. *Materials Letters*, *64*(14), 1647-1649.

[45] Guo, T. H., Liu, Y., Zhang, Y. C., & Zhang, M. (2011). Green hydrothermal synthesis and optical absorption properties of ZnO2 nanocrystals and ZnO nanorods. *Materials Letters*, *65*(4), 639-641.

[46] Guo, M., Li, L., Lin, H., Zuo, Y., Huang, X., & Li, G. (2013). Targeted deposition of ZnO 2 on brookite TiO 2 nanorods towards high photocatalytic activity. *Chemical Communications*, *49*(100), 11752-11754.

[47] Deb, S. K. (2008). Opportunities and challenges in science and technology of WO3 for electrochromic and related applications. *Solar Energy Materials and Solar Cells*, *92*(2), 245-258.

[48] Lu, X., Zhai, T., Zhang, X., Shen, Y., Yuan, L., Hu, B., ... & Tong, Y. (2012). WO3–x@ Au@ MnO2 Core–Shell Nanowires on Carbon Fabric for High-Performance Flexible Supercapacitors. *Advanced materials*, *24*(7), 938-944.

[49] Irie, H., Miura, S., Kamiya, K., & Hashimoto, K. (2008). Efficient visible light-sensitive photocatalysts: grafting Cu (II) ions onto TiO2 and WO3 photocatalysts. *Chemical Physics Letters*, *457*(1-3), 202-205.

[50] Cao, H. T., Pei, Z. L., Gong, J., Sun, C., Huang, R. F., & Wen, L. S. (2004). Preparation and characterization of Al and Mn doped ZnO (ZnO:(Al, Mn)) transparent conducting oxide films. *Journal of Solid State Chemistry*, *177*(4-5), 1480-1487.

[51] Götzendörfer, S., Polenzky, C., Ulrich, S., & Löbmann, P. (2009). Preparation of CuAlO2 and CuCrO2 thin films by sol–gel processing. *Thin Solid Films*, *518*(4), 1153-1156.

[52] Ghosh, C. K., Popuri, S. R., Mahesh, T. U., & Chattopadhyay, K. K. (2009). Preparation of nanocrystalline CuAlO 2 through sol–gel route. *Journal of sol-gel science and technology*, *52*(1), 75-81.

[53] Zayats, A. V., Smolyaninov, I. I., & Maradudin, A. A. (2005). Nano-optics of surface plasmon polaritons. *Physics reports*, *408*(3-4), 131-314.

[54] Pendry, J. B., Holden, A. J., Stewart, W. J., & Youngs, I. (1996). Extremely low frequency plasmons in metallic mesostructures. *Physical review letters*, *76*(25), 4773.

[55] Liu, Z. W., Wei, Q. H., & Zhang, X. (2005). Surface plasmon interference nanolithography. *Nano letters*, *5*(5), 957-961.

[56] Pillai, S., Catchpole, K. R., Trupke, T., & Green, M. A. (2007). Surface plasmon enhanced silicon solar cells. *Journal of applied physics*, *101*(9), 093105.

[57] Haes, A. J., & Van Duyne, R. P. (2002). A nanoscale optical biosensor: sensitivity and selectivity of an approach based on the localized surface plasmon resonance spectroscopy of triangular silver nanoparticles. *Journal of the American Chemical Society*, *124*(35), 10596-10604.

[58] Naik, G. V., Kim, J., & Boltasseva, A. (2011). Oxides and nitrides as alternative plasmonic materials in the optical range. *Optical Materials Express*, *1*(6), 1090-1099.

[59] Ellmer, K. (2012). Past achievements and future challenges in the development of optically transparent electrodes. *Nature Photonics*, *6*(12), 809.

[60] Ali, H. M., El-Raheem, M. A., Megahed, N. M., & Mohamed, H. A. (2006). Optimization of the optical and electrical properties of electron beam evaporated aluminum-doped zinc oxide films for opto-electronic applications. *Journal of Physics and Chemistry of Solids*, *67*(8), 1823-1829.

[61] Raniero, L., Ferreira, I., Pimentel, A., Goncalves, A., Canhola, P., Fortunato, E., & Martins, R. (2006). Role of hydrogen plasma on electrical and optical properties of ZGO, ITO and IZO transparent and conductive coatings. *Thin Solid Films*, *511*, 295-298.

[62] Bhosle, V., Tiwari, A., & Narayan, J. (2006). Electrical properties of transparent and conducting Ga doped ZnO. *Journal of Applied Physics*, *100*(3), 033713.

[63] Sengupta, J., Sahoo, R. K., & Mukherjee, C. D. (2012). Effect of annealing on the structural, topographical and optical properties of sol–gel derived ZnO and AZO thin films. *Materials Letters*, *83*, 84-87.

[64] Jung, Y. S., Seo, J. Y., Lee, D. W., & Jeon, D. Y. (2003). Influence of DC magnetron sputtering parameters on the properties of amorphous indium zinc oxide thin film. *Thin Solid Films*, *445*(1), 63-71.

[65] Gupta, A., & Compaan, A. D. (2004). All-sputtered 14% CdS∕CdTe thin-film solar cell with ZnO: Al transparent conducting oxide. *Applied Physics Letters*, *85*(4), 684-686.

[66] He, H., Orlando, R., Blanco, M. A., Pandey, R., Amzallag, E., Baraille, I., & Rérat, M. (2006). First-principles study of the structural, electronic, and optical properties of Ga 2 O 3 in its monoclinic and hexagonal phases. *Physical Review B*, *74*(19), 195123.

[67] Agashe, C., Kluth, O., Schöpe, G., Siekmann, H., Hüpkes, J., & Rech, B. (2003). Optimization of the electrical properties of magnetron sputtered aluminum-doped zinc oxide films for opto-electronic applications. *Thin Solid Films*, *442*(1-2), 167-172.

[68] Gupta, R. K., Ghosh, K., Patel, R., Mishra, S. R., & Kahol, P. K. (2008). Structural, optical and electrical properties of In doped CdO thin films for optoelectronic applications. *Materials Letters*, *62*(19), 3373-3375.

[69] Gonçalves, G., Elangovan, E., Barquinha, P., Pereira, L., Martins, R., & Fortunato, E. (2007). Influence of post-annealing temperature on the properties exhibited by ITO, IZO and GZO thin films. *Thin solid films*, *515*(24), 8562-8566.

[70] Assuncao, V., Fortunato, E., Marques, A., Aguas, H., Ferreira, I., Costa, M. E. V., & Martins, R. (2003). Influence of the deposition pressure on the properties of transparent and conductive ZnO: Ga thin-film produced by rf sputtering at room temperature. *Thin Solid Films*, *427*(1-2), 401-405.

[71] Snedeker, R. H., Garty, K. T., & Skiermont, F. J. (1971). *U.S. Patent No. 3,622,440*. Washington, DC: U.S. Patent and Trademark Office.

[72] Takeda, H., Yabuki, K., & Adachi, K. (2001). *U.S. Patent No. 6,319,613*. Washington, DC: U.S. Patent and Trademark Office.

[73] KUNO, H., *Near infra-red shielding single ormultilayer film and a coating liquid for form ing the same: EP, 0943587 A1*.

[74] Isojima, T., Yamakawa, T., Maru, N., Aikyou, H., Takeuchi, H., Funayama, K., & Kusaka, H. (2011). *U.S. Patent Application No. 13/125,744*.

[75] Nishihara, A., Hayashi, T., & Sekiguchi, M. (1996). *U.S. Patent No. 5,518,810*. Washington, DC: U.S. Patent and Trademark Office.

[76] Kunimatsu, M., & Yamazaki, Y. (1998). *U.S. Patent No. 5,807,511*. Washington, DC: U.S. Patent and Trademark Office.

[77] Kondo, T. (1998). *U.S. Patent No. 5,830,568*. Washington, DC: U.S. Patent and Trademark Office.

[78] Feng, J., Huang, B., & Zhong, M. (2009). Fabrication of superhydrophobic and heat-insulating antimony doped tin oxide/polyurethane films by cast replica micromolding. *Journal of colloid and interface science*, *336*(1), 268-272.

[79] Wang, L., Hang, J., Shi, L., Sun, X., & Xu, F. (2012). Preparation and characterization of NIR cutoff antimony doped tin oxide/hybrid silica coatings. *Materials Letters*, *87*, 35-38.

[80] Li, S., Zhu, P., Zhao, T., & Sun, R. (2014). Optical, electrical, and thermal insulation properties of antimony-doped tin oxide nanoparticles prepared by frozen gel method. *Journal of Sol-Gel Science and Technology*, *70*(3), 366-370.

[81] Lu, X., Yu, G., Tan, Q., Hu, B., Zhang, J., & Dong, Q. (2014). Preparation and characterization of transparent fluorocarbon emulsion doped with antimony tin oxide and TiO 2 as thermal-insulating and self-cleaning coating. *Journal of Coatings Technology and Research*, *11*(4), 567-574.

[82] Li, Y., Liu, J., Liang, J., Yu, X., & Li, D. (2015). Tunable solar-heat shielding property of transparent films based on mesoporous Sb-doped SnO2 microspheres. *ACS applied materials & interfaces*, *7*(12), 6574-6583.

[83] Buonsanti, R., Llordes, A., Aloni, S., Helms, B. A., & Milliron, D. J. (2011). Tunable infrared absorption and visible transparency of colloidal aluminum-doped zinc oxide nanocrystals. *Nano letters*, *11*(11), 4706-4710.

[84] Li, Y. Q., Kang, Y., Xiao, H. M., Mei, S. G., Zhang, G. L., & Fu, S. Y. (2011). Preparation and characterization of transparent Al doped ZnO/epoxy composite as thermal-insulating coating. *Composites Part B: Engineering*, *42*(8), 2176-2180.

[85] Soumya, S., Mohamed, A. P., Mohan, K., & Ananthakumar, S. (2015). Enhanced near-infrared reflectance and functional characteristics of Al-doped ZnO nano-pigments embedded PMMA coatings. *Solar Energy Materials and Solar Cells*, *143*, 335-346.

[86] Guo, C., Yin, S., Huang, L., & Sato, T. (2011). Synthesis of one-dimensional potassium tungsten bronze with excellent near-infrared absorption property. *ACS applied materials & interfaces*, *3*(7), 2794-2799.

[87] Guo, C., Yin, S., Dong, Q., Kimura, T., Tanaka, M., Hang, L. T., ... & Sato, T. (2013). Solvothermal fabrication of rubidium tungsten bronze for the absorption of near infrared light. *Journal of nanoscience and nanotechnology*, *13*(5), 3236-3239.

[88] Moon, K., Cho, J. J., Lee, Y. B., Yoo, P. J., Bark, C. W., & Park, J. (2013). Near infrared shielding properties of quaternary tungsten bronze nanoparticle Na 0.11 Cs 0.22 WO 3. *Bulletin of the Korean Chemical Society*, *34*(3), 731-734.

[89] Zhao, Z., Yin, S., Guo, C., & Sato, T. (2015). CsxWO3 Nanoparticles for the Near-Infrared Shielding Film. *Journal of nanoscience and nanotechnology*, *15*(9), 7173-7176.

[90] Zhong, W., Yu, N., Zhang, L., Liu, Z., Wang, Z., Hu, J., & Chen, Z. (2016). Synthesis of CuS nanoplate-containing PDMS film with excellent near-infrared shielding properties. *RSC Advances*, *6*(23), 18881-18890.

[91] Adachi, K., Miratsu, M., & Asahi, T. (2010). Absorption and scattering of near-infrared light by dispersed lanthanum hexaboride nanoparticles for solar control filters. *Journal of Materials Research*, *25*(3), 510-521.

[92] Chen, D., Min, G., Wu, Y., Yu, H., & Zhang, L. (2015). The preparation and composition design of boron-rich lanthanum hexaboride target for sputtering. *Journal of Alloys and Compounds*, *638*, 380-386.

[93] Frasca, S., von Graberg, T., Feng, J. J., Thomas, A., Smarsly, B. M., Weidinger, I. M., ... & Wollenberger, U. (2010). Mesoporous indium tin oxide as a novel platform for bioelectronics. *ChemCatChem*, *2*(7), 839-845.

[94] Müller, V., Rasp, M., Rathouský, J., Schütz, B., Niederberger, M., & Fattakhova-Rohlfing, D. (2010). Transparent Conducting Films of Antimony-Doped Tin Oxide with Uniform Mesostructure Assembled from Preformed Nanocrystals. *Small*, *6*(5), 633-637.

[95] Hou, K., Puzzo, D., Helander, M. G., Lo, S. S., Bonifacio, L. D., Wang, W., ... & Ozin, G. A. (2009). Dye-Anchored Mesoporous Antimony-Doped Tin Oxide Electrochemiluminescence Cell. *Advanced Materials*, *21*(24), 2492-2496.

[96] Yiu, H. H., & Wright, P. A. (2005). Enzymes supported on ordered mesoporous solids: a special case of an inorganic–organic hybrid. *Journal of Materials Chemistry*, *15*(35-36), 3690-3700.

[97] Guo, K., Hu, Y., Zhang, Y., Liu, B., & Magner, E. (2010). Electrochemistry of nanozeolite-immobilized cytochrome c in aqueous and nonaqueous solutions. *Langmuir*, *26*(11), 9076-9081.

[98] El Kasmi, A., Leopold, M. C., Galligan, R., Robertson, R. T., Saavedra, S. S., El Kacemi, K., & Bowden, E. F. (2002). Adsorptive immobilization of cytochrome c on indium/tin oxide (ITO): electrochemical evidence for electron transfer-induced conformational changes. *Electrochemistry Communications*, *4*(2), 177-181.

[99] Topoglidis, E., Campbell, C. J., Cass, A. E., & Durrant, J. R. (2001). Factors that affect protein adsorption on nanostructured titania films. A novel spectroelectrochemical application to sensing. *Langmuir*, *17*(25), 7899-7906.

[100] Willit, J. L., & Bowden, E. F. (1990). Adsorption and redox thermodynamics of strongly adsorbed cytochrome c on tin oxide electrodes. *Journal of Physical Chemistry*, *94*(21), 8241-8246.

[101] Renault, C., Balland, V., Martinez-Ferrero, E., Nicole, L., Sanchez, C., & Limoges, B. (2009). Highly ordered transparent mesoporous TiO 2 thin films: an attractive matrix for efficient immobilization and spectroelectrochemical characterization of cytochrome c. *Chemical Communications*, (48), 7494-7496.

[102]   Rui, Q., Komori, K., Tian, Y., Liu, H., Luo, Y., & Sakai, Y. (2010). Electrochemical biosensor for the detection of H2O2 from living cancer cells based on ZnO nanosheets. *Analytica Chimica Acta*, *670*(1-2), 57-62.

[103]   Yin, Y., Wu, P., Lü, Y., Du, P., Shi, Y., & Cai, C. (2007). Immobilization and direct electrochemistry of cytochrome c at a single-walled carbon nanotube-modified electrode. *Journal of Solid State Electrochemistry*, *11*(3), 390-397.

Chapter 3 Objectives

Antimony doped tin oxide (ATO) is a kind of transparent conductive oxide (TCO), which exhibits a promising heat insulation property, due to its high absorption in NIR light range. Comparing with Low-E glass which has a high reflection of the sunlight, ATO can avoid the so called "light pollution" that has been prohibited in many countries. However, there are still several problems preventing the ATO from large-scale industrialization, i.e. the dispersion of ATO and NIR light absorption related problems. The primary size of the as-prepared nanoparticle is more than 100nm using the ceramic method, which can be hardly dispersed evenly in water and ATO exhibits poor NIR shielding performance in the wavelength range from 800nm to 1300nm. A new method is needed to develop this novel material. The objective of this thesis is to overcome these deficiencies through designing a novel $TiO_2/ATO/Cs_xWO_3$ thin film for producing IR-blocking multifunctional heat insulation coating. The main aims and objectives are summarized as follows:

1) The ATO nanoparticles and CsxWO3 nanoparticles will be fabricated by controlled hydrothermal reaction and s series of optimization experiment.

2) Then, these nanoparticles will be dispersed in water as an aqueous solution in a simple method which exhibited a low secondary particle size distribution.

3) For further study of its application performance, a wide waveband two-components transparent NIR shielding coating containing ATO and Cs_xWO_3 film will be synthesized using the waterborne polyurethane (WPU) as the

matrix resin.

4) To further enhance the NIR light shielding, the black TiO$_2$ film will be developed by controllable solvothermal method and optimized electroreduction experiment. The black-TiO$_2$ film was composed with self-doped TiO$_2$, which exhibited an excellent self-cleaning property and a high NIR light blocking rate.

5) Finally, the structural TiO$_2$/ATO/Cs$_x$WO$_3$ thin film will be fabricated in this study. Excitingly, it should show good NIR shielding performance and high visible transparency. The optimal thickness of the TiO$_2$ films is 4μm, and the TiO$_2$ film will act as the external layer in the substrate glass.

Chapter 4 Experimental Methods

4.1 Raw Materials

The chemical raw materials in this thesis are listed in Table 4.1

Figure 4.1 List of chemical raw materials

Name	Remark	Manufactory
H_2SO_4	98wt%	West Gansu Chemical (Mainland of China)
	30wt%	West Gansu Chemical (Mainland of China)
HCl	37wt%	West Gansu Chemical (Mainland of China)
SN5040	80wt%	West Gansu Chemical (Mainland of China)
Sn	97wt%	Alfa Aesar
SnO_2	AR	Alfa Aesar
$SbCl_3$	AR	Alfa Aesar
Sb_2O_3	AR	Alfa Aesar
Ethanol	AR	Aladdin
Tetrabutyl Titanate	AR	Aladdin
N'N'-Dimethylacrtamide	AR	Aladdin
Ethanediol	AR	Aladdin
NH_4Cl	AR	Aladdin
Citric Acid	AR	Aladdin

4.2 Characterization

4.2.1 X-Ray Diffraction (XRD)

The crystal structure of the nanoparticles was recorded by the X-Ray Diffraction (XRD), Druker D8 Advance, with using Cu-Ka radiation ($\lambda=0.15418$nm) as shown in Figure 4.1. The scan mode is step scan and the step size is 0.5°. The electric current and voltage of the equipment are 40mA and 20KV, respectively.

Figure 4.2 X-ray Diffractometer

4.2.2 Scanning Electron Microscopy (SEM)

The morphology and composition of the nanoparticles will be measured with the Tescan VEGA3 as shown in Figure 4.2. It shows a high resolution of 5nm with an energy of 12 KeV. The equipment is also provided with an energy dispersive X-ray spectroscopy (EDS Bruker) which can analysis the element content of the nanoparticles.

Figure 4.3 Scanning Electron Microscopy

In this study, the thickness and the surface roughness were recorded in the equipment. And to enhance the resolution, the gold film and silver paste will be coated on the surface of the samples. Meanwhile, the samples are also fixed on the specimen disk.

4.2.3 Transparent Electron Microscopy (TEM)

The TEM images of the nanoparticles were recorded with the JEOL Model JEM-2100F as shown in Figure 4.3. It shows a high resolution of 1nm which can record the morphology, Selected Area Diffraction (SAED) pattern, crystal lattice of the nanoparticles.

Figure 4.4 Transparent Electron Microscopy

4.2.4 Laser Particle Analyzer (LPA)

The secondary particle size of the nanoparticles and the dispersity of the nanoparticle aqueous solution were measured by the Mastersizer 3000 with laser diffraction as shown in Figure 4.4. The instrument is equipped with optical bench and sample dispersion units. During the testing, a laser beam illuminates the sample and a number of detectors measure the intensity of light scattered with a wide range of angles. The nanoparticles aqueous solution was dispersed by stirring and ultrasound in the dispersion units.

Figure 4.5 Laser Particle Analyzer (Mastersizer 3000)

4.2.5 UV-Vis-Near Infrared Spectrophotometer

In this thesis, to measure the optical property of the nano films, a Hitachi UH4150 UV-Vis-Near Infrared spectrophotometer, as shown in Figure 4.5, is employed in the wavelength range from 300nm to 2500nm for optical reflectance and optical transmittance measurements. In addition, the scanning rate of the measurements was 100nm/min.

Figure 4.6 UV-Vis-NIR spectrophotometer

4.2.6 The photocatalysis of the coating

The photocatalysis of the coating was investigated by performing photocatalytic activity experiments to evaluate degradation of the aqueous methylene blue (MB) solution by placing the thin films under illumination of fluorescent lamp light source (12w, 150mm long, broad emission peak range is 365nm-750nm, and the center peak is 550nm). The experiments, as shown in Figure 4.6, were placed at room temperature

where each sample was soaked in a glass container containing the MB solution and the glass containers were placed in a photocatalyzed reactor which was pained in black. The distance between the fluorescent lamp and the sample is 10cm. After 3h of irradiation time, the absorbance of the MB solution would be measured by UV-Vis-NIR spectrophotometer for wavelength range of 580nm-700nm and the scanning rate of 100nm/min. Finally, the degradation efficiency of the MB solution was estimated to obtain the photocatalytic activity of the coating.
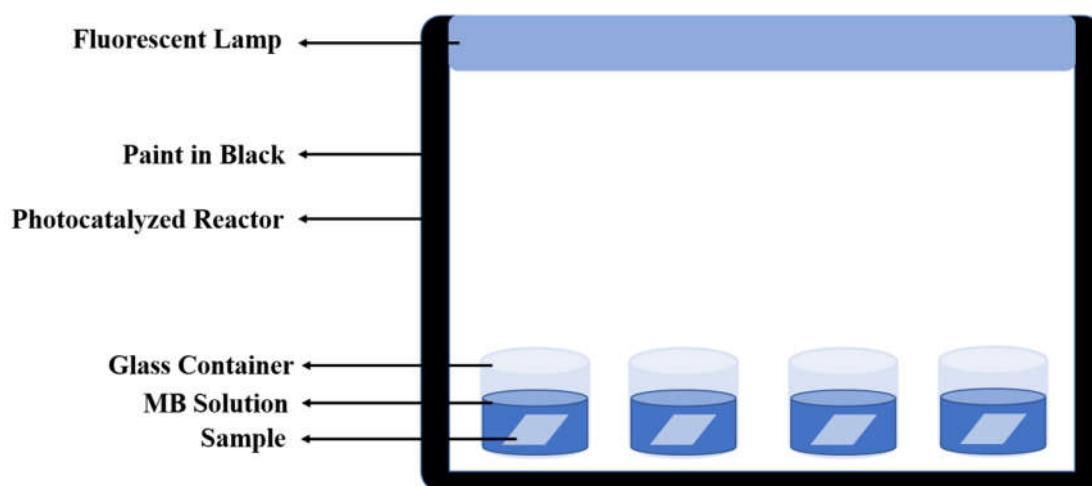
Figure 4.7 Schematic diagram of the photocatalytic property test

Due to the photocatalytic property of the films, the absorbance of the MB solution was expected to decrease. Based on the detected absorbance, the degradation efficiency of the film, D was calculated by using the equation (4.1).

$$D = \frac{Ab_0 - Ab_i}{Ab_0} \times 100\% \qquad\qquad (4.1)$$

where Ab_0 is the absorption of the light irradiated aqueous MB solution and Ab_i is the absorption of the MB solution after degradation by samples.

4.2.7 Contact Angle Meter (CAM)

To evaluate the self-cleaning properties of different samples, a camera was used to record the static behavior of a water droplet on the surface of different samples. The water contact angle (WCA) on the as-prepared samples was measured from sessile drops by a contact angle mater provided with a stage (JCY20-13, Shanghai Fangrui Science & Technology Co., LTD, China) as shown in Figure 4.7.
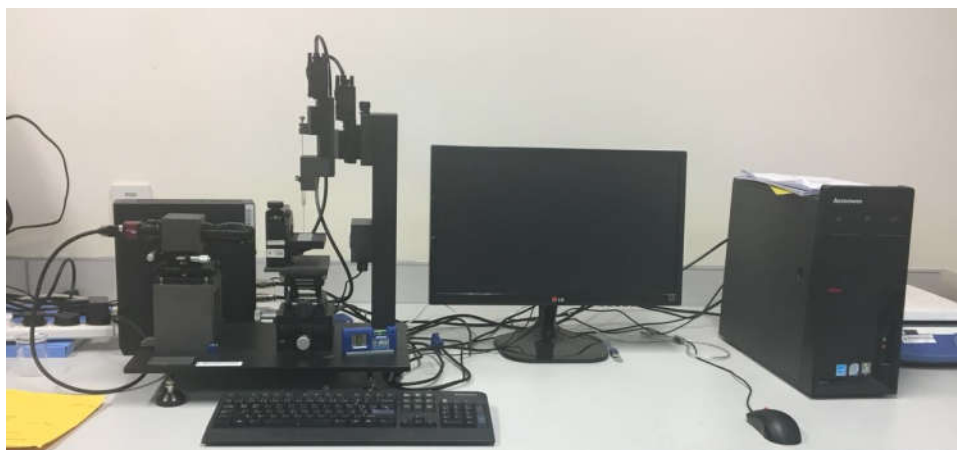
Figure 4.8 The Contact Angle Meter

4.3 Fabrication Equipment and Devices

4.3.1 Hydrothermal reactor

The nanoparticles were synthesized by controllable hydrothermal reaction with hydrothermal reactor as shown in figure 4.8. The shell and the liner of the reactor are stainless steel and para polyphenyl (PPL). PPL shows high temperature resistance (250°C~280°C).

Figure 4.9 Hydrothermal Reactor

4.3.2 Automatic Spraying Equipment

The thin films based on nanoparticles were fabricated by automatic spraying equipment from Hong Sheng Electronic Equipment Co., LTD, China as shown in figure 4.9. The diameter of the nozzle of the spraying gun in the equipment is 0.5mm, the coating was sprayed in the surface of subtract with 0.2MPa by using a turbo molecular pump. The distance between the substrate and the spraying gun was 30cm. During deposition, the substrate temperature was kept constant at room temperature.
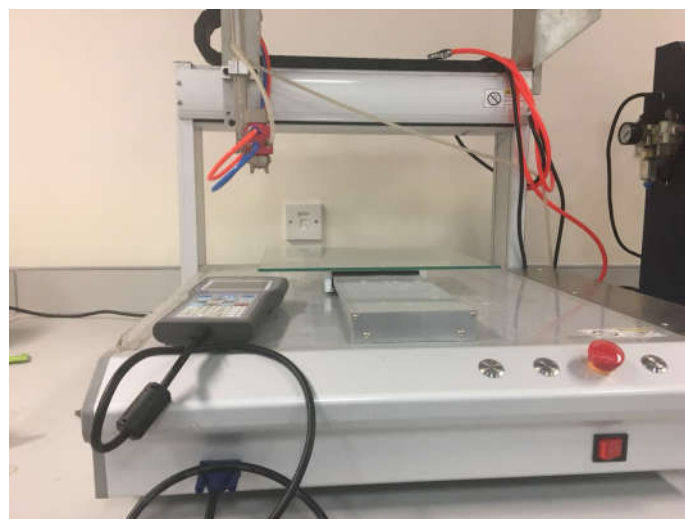
Figure 4.10 Automatic Spraying Equipment

4.3.3 Electric Reduction Equipment (ERE)

Black TiO_2 thin films were developed by an in-house made reactor, as shown in figure 4.10, where every film was placed on the surface of conductive glass and soaked inside a glass container containing the NH_4Cl, deionized water, and ethylene glycol. This device was equipped with direct-current electrical source (DCES), which can control the magnitude current of 0~5A and voltage of 0~30V.
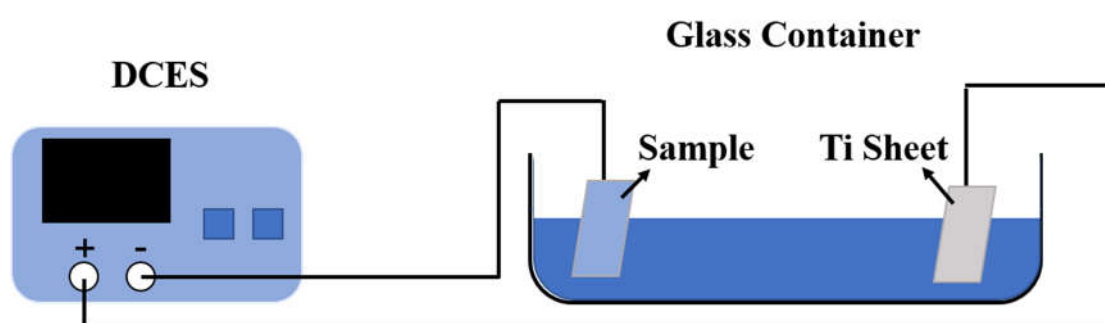
Figure 4.11 Electric Reduction Equipment

Chapter 5 Development and Investigation of Nano ATO and ATO Aqueous Dispersion

5.1 Introduction

Transparent conductive oxide (TCO) such as doped indium, doped tin, zinc oxide, because of their unique high electrical conductivity and visible light transmittance, which are widely used in solar cells and flat panel display device such as a thin layer of transparent electrodes, smart windows and chemical sensors, etc. In recent years, more scientists have shifted their eyes from thin films to nano-tco crystals. ATO (Antimony-doped tin oxide) has an optical band gap of more than 3.6eV, which has high transmittance in the visible region and has a high N type conductivity. Currently on the market, the commonly used transparent conductive oxide ITO (Indium tin oxide) resources are scarce and expensive, therefore ATO is ITO beneficial alternatives, and has broad prospect of research and application value [1].

There are a series of preparation for ATO nanometer crystal with different shape, size, conductivity, concentration. Generally speaking, compared to the physical method, chemical method can better control the ATO nanometer crystal grain size and the degree of stability in solution [2].The main chemical methods include sol-gel method [3], polymer precursor method [4], chemical coprecipitation [5], hydrothermal reaction and solvent thermal reaction [6].Among them, the sol-gel method, polymer precursor method and chemical coprecipitation method, can prepare large size particles, and

prevent the aggregation of nanoparticles. Hydrothermal reaction and solvent thermal reaction can better control the particle size of ATO in the process of growth, doping level and ATO dispersion in different solvents, etc.

Therefore, this chapter adopts the solvent thermal preparation to synthesize antimony doped with different content of ATO nanoparticles and use water as dispersion medium for preparation of ATO nanoparticles aqueous dispersion. The experiment focuses on the influence of different doping amount, reaction time and reaction temperature on the ATO particle size, morphology and the ATO spectral transmittance curve. At the same time, the effects of different dispersants and their addition amount, different pH value and different dispersion methods on the stability of ATO nano-aqueous dispersion were investigated. Using transmission electron microscopy (TEM), X-ray diffraction (XRD), scattering spectroscopy (EDS), laser particle size instrument to characterize particle size distribution and particle morphology of ATO nanoparticles, using UV-Vis-NIR spectrophotometer to measure the transmittance of the ATO in 300 ~ 2500 nm wavelength region and, study its infrared absorption properties.

5.2 Experiment

5.2.1 Development of Nano ATO

Nano ATO was synthesized by controllable hydrothermal reaction, and the details of the technical process are as followed (Figure 5.1):

1) The Sn powder and Sb_2O_3 were weigh with analytical balance and mixed in an agate mortar as a mixture A. The Sb% was designed as the equation 5.1.

$$Sb\% = \frac{Sb\ mol}{Sb\ mol + Sn\ mol} \times 100\% \qquad (5.1)$$

2) The mixture A was added with concentrated sulfuric acid in a glass contained and stirred with a glass rod, until the product became a black colloid as a mixture B.

3) The mixture B was added with hydrogen peroxide in PPL liner and stirred with a glass rod. During this process, a lot of heat would be produced and a yellow colloid was obtained.

4) The PPL with the reactant was sealed in stainless steel case and placed in drying oven at certain temperature.

5) After finishing reaction, the ionic impurity in the product should be removed by centrifuge and deionized water. Then the solid in the bottom of the centrifuge tube would be transferred into vacuum drying oven at 100°C. After drying, the navy-blue ATO nanoparticles, as shown in figure 5.2, would be obtained.
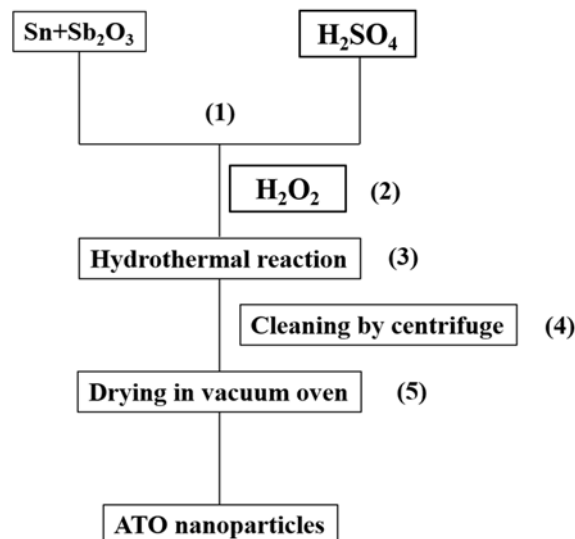
Figure 5.1 Synthesis of ATO nanoparticles
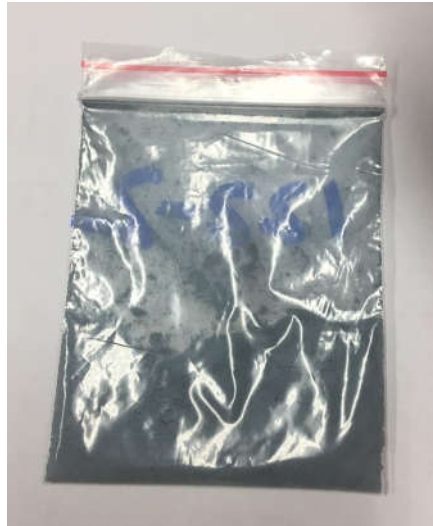
Figure 5.2 ATO nanoparticles

5.2.2 Development of ATO aqueous solution

A certain quality of the ATO nanoparticles, which were measured by analytical balance, were mixed with dispersing agent, hydrochloric acid and deionized water. A suspension liquid would be obtained after mechanical agitation and ultrasonic dispersion. The suspension then was placed into agate jar. After ball milling with some time, the final ATO aqueous solution would be fabricated. The details of the process are shown in figure 5.3.
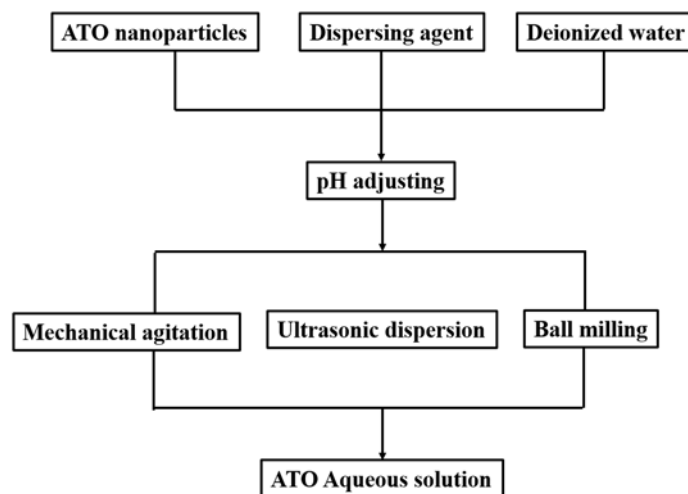
Figure 5.3 The fabrication of ATO aqueous solution

5.3 Results and discussion

5.3.1 ATO characterization

ATO nanoparticles were fabricated through controllable thermal insulation coating which is conducted as 5.2.1. The crystal structure of the nanoparticles was recorded by XRD, and are shown in Figure 5.4 A. It can be found that the peak positions of sample in red line is well agree with the reflections of bulk cassiterite SnO_2 in black line. Plus, no other impurity peaks in samples can be recorded, which indicates that antimony ions are uniformly replaced the tin ions in SnO_2 crystal structure.

The morphology of ATO nanoparticles were observed by TEM and are shown in figure 5.4B. The particle size of ATO is homogeneous and the size distribution is around 5-10nm. The SAED pattern taken form a part of the ATO nanoparticles in figure 5.4B are shown in figure 5.4C, which can be found that the nanoparticles possess interplanar spacings of 3.3470, 2.6427, 2.3487, 2.2694, 1.7641, and 1.4155Å corresponding to the (110), (101), (200), (111), (211), and (301) planes, respectively. Figure 5.4D shows the HRTEM image of the ATO nanoparticles. In this image, the lattice plane of ATO nanoparticles was (111) with a lattice space of 2.2694Å. Figure 5.4F shows the EDX of the ATO samples which can be found that the major elemental composition are Sn, Sb and O. The characteristic peak of Sn element is at 3.1, 3.5, 3.9, 4.2 and 4.3KeV, and the characteristic peak of Sb element appeared at 3.3, 3.4, 4.0, and 4.6KeV. In addition, the peak of O element at 0.5KeV can be observed in this figure. Besides, the Cu and C elements in the EDX pattern are from the TEM copper grid. Hence, it can be deduced

from the results that the sample can be regarded as the well-organized ATO structures.
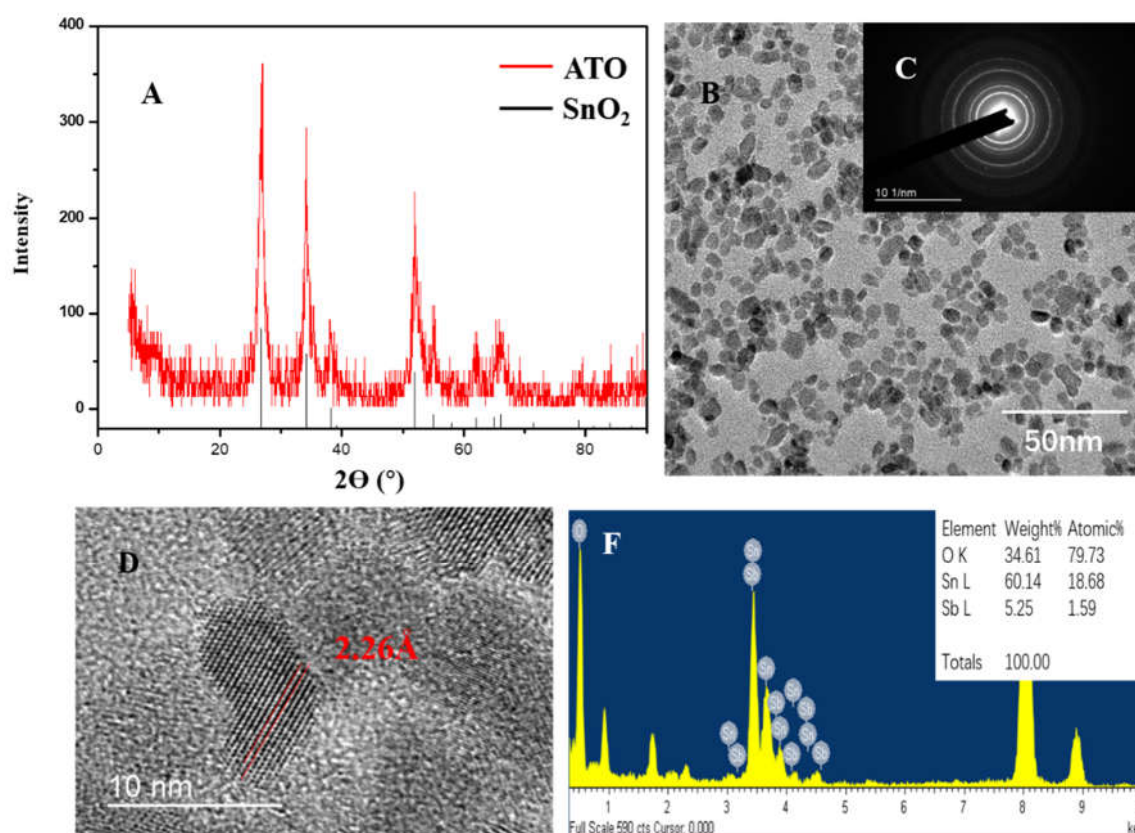
Figure 5.4 The Characterization of ATO nanoparticles

A: XRD pattern for ATO; B: TEM image for ATO nanoparticles; C: SAED image for ATO nanoparticles; D: HRTEM image for ATO nanoparticles; F: EDX pattern for ATO nanoparticles

5.3.2 Effect of Reaction Conditions on the Morphology and Properties of the ATO Nanoparticles

5.3.2.1 Effect of Reaction Temperature on the Morphology of the ATO Nanoparticles

Controllable hydrothermal reaction is a widely used crystallization reaction in nano-semiconductor materials fabrication. During this method, the physical properties

of the reactant would be changed to enhance the activity of crystallization reaction, and the crystal growth of the final product would be controllable. Meanwhile, the reaction condition of this method is mild than other traditional method, and the particle size distribution and the morphology could be controllable by changing the reaction conditions. Hence, this thesis has investigated the different reaction temperature and reaction time impact on the morphology of the ATO. The experimental procedures were conducted as in the 5.2.1. The reaction temperature was maintained in 200°C, 220°C, 230°C and 240°C. The reaction time would be kept in 12 hours, and the Sb% would be kept in 10%.

Figure 5.5 shows the TEM images of different samples in different reaction temperature. It can be found that the particle size distribution would increase with the reaction temperature enhancing. The average particle size of sample A, B, C and D is 4nm, 8nm, 11nm, and 14nm, respectively. This was attributed to that the high reaction temperature could make the precursor quickly to be saturated solution which will enhance the crystallization rate. However, the lattice imperfection would be enlarged with the crystallization rate increased, during the hydrothermal reaction. Hence, to obtain the small particle size and reduce the lattice imperfection of nano ATO, the reaction temperature should be decrease on the premise of fully crystallized.
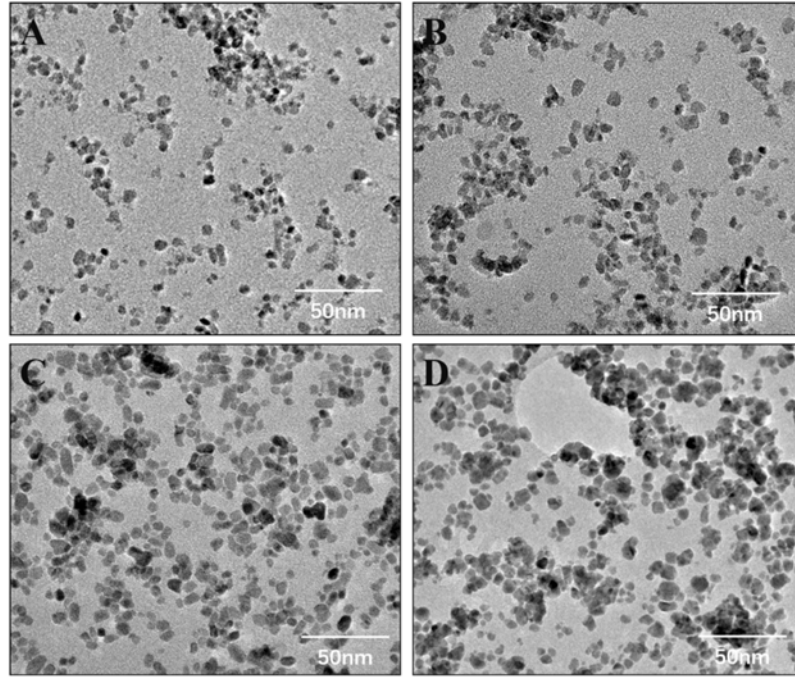
Figure 5.5 TEM image of different samples in different reaction temperature

A: 200°C, B: 220°C, C: 230°C and D: 240°C

Figure 5.6 shows the XRD pattern of different samples in different reaction temperature. It could be found that the intensity of the peaks would increase with the reaction temperature enhancing. The peaks position of sample C and sample D were well agreed with the reflections of bulk cassiterite SnO_2 in black line. In addition, no other impurity peaks in samples can be recorded, indicating that antimony ions are uniformly replaced the tin ions in SnO_2 crystal structure. However, sample A and sample B only show a clearly peaks position of (110), (101) and (211), which means that it crystallized un-fully crystallized in the reaction temperature of 200°C and 220°C.
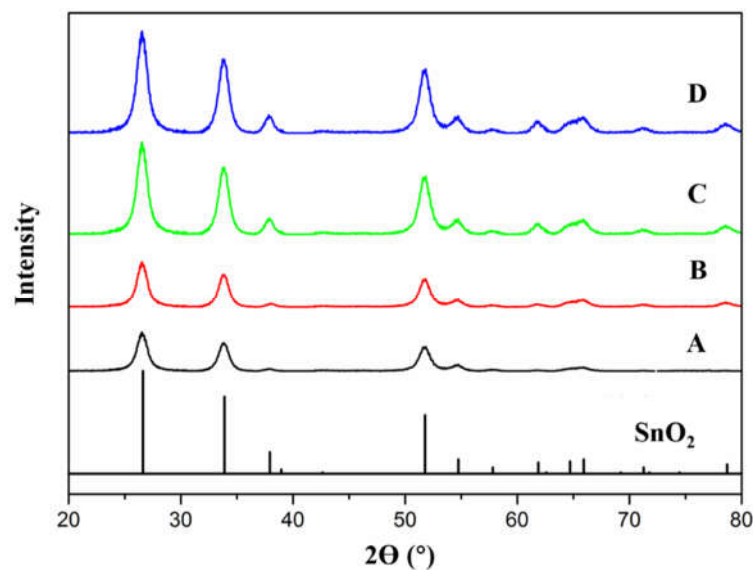
Figure 5.6 XRD pattern of different samples in different reaction temperature

A: 200℃, B: 220℃, C: 230℃ and D: 240℃

Owing to the above investigation of the effects of reaction temperature on the morphology of the ATO nanoparticles, the optimized reaction temperature of hydrothermal reaction of TO nanoparticle is 230℃.

5.3.2.2 Effect of Reaction Time on the Morphology of the ATO Nanoparticles

Reaction time is another important condition in hydrothermal reaction. This thesis investigated the effects of reaction time on the morphology of the ATO nanoparticles. The steps of experiment were conducted as in the 5.2.1. The reaction time was maintained at 6h, 8h, 12h, and 24h, respectively. The reaction temperature would be kept in 230℃, and the sb% would be kept in 10%.
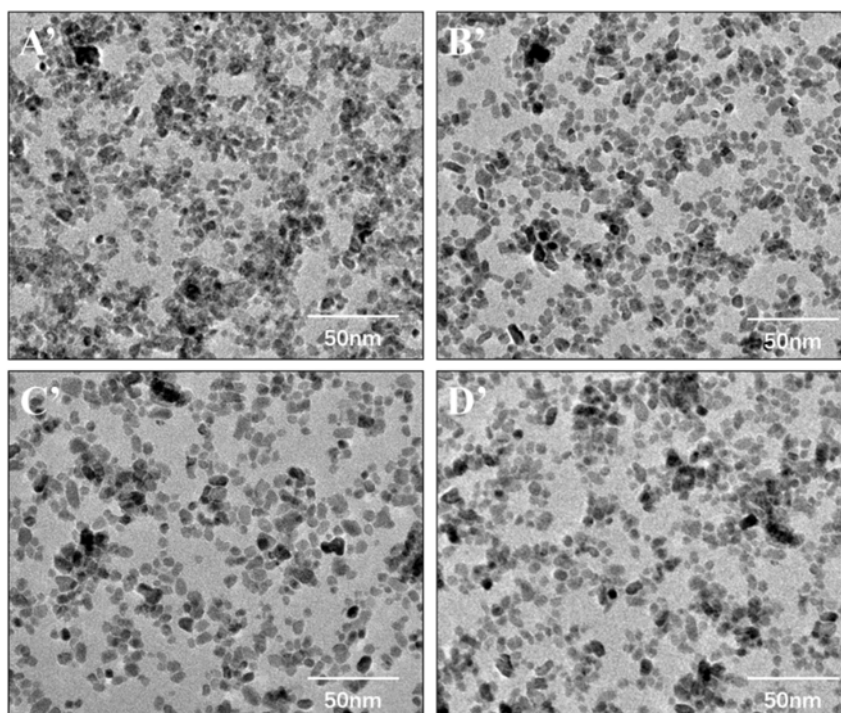
Figure 5.7 TEM image of different samples in different reaction time

A': 6h, B': 8h, C': 12h and D': 24h

Figure 5.7 shows the TEM image of different samples in different reaction time. It could be found that with the extension of reaction time, the particle size distribution would be increased slightly. However, the particle size distribution of sample C and sample D were roughly the same. The reason is that Ostwald Ripening would be in the hydrothermal reaction, in other words, the small crystal in the solution would be dissolved and deposited again on the large crystals. If the reaction time is too short, the grain could not be grow in completed nanocrystal. Nevertheless, the overextended reaction time would lead more nanocrystal conglomerated in large size particles, due to that the crystal growth had been saturated and the morphology of nanoparticles had been unchanged in a certain reactant content.

Figure 5.8 shows the XRD pattern of different samples at different reaction time. It could be found that the intensity of the peaks in the pattern would be increased with the reaction time protracted, which is consistent with the change of TEM image shows. In sample A' and B' which are in a short reaction time, the curves show a poor weakness, and the diffraction peaks are not obviously. This indicated that the reaction time is too short to have enough time with crystal growth of grain. When the reaction extends to 12 hours, the crystallization of nan ATO reacts completely and the nanoparticles crystal grows perfectly. Hence, the cures of sample C and sample D show a high intensity peaks in pattern.
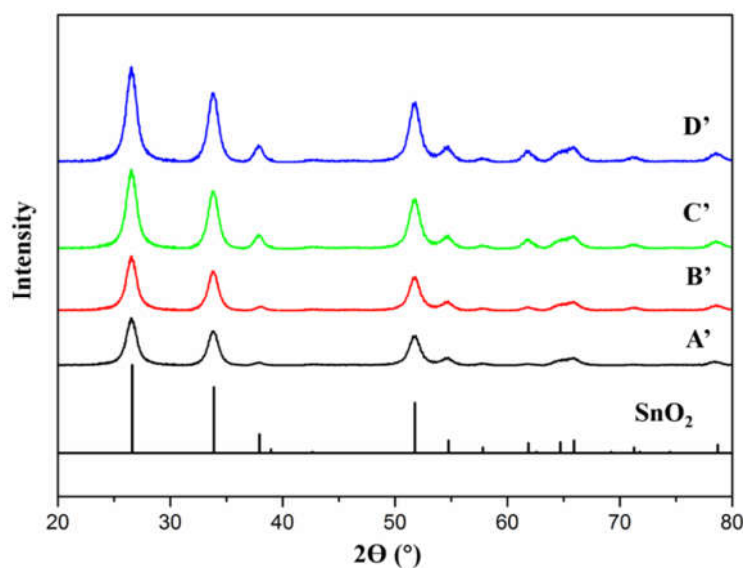
Figure 5.8 XRD pattern of different samples in different reaction time

A': 6h, B': 8h, C': 12h and D': 24h

According to the above investigation, to obtain a fully crystallization of ATO nanoparticles, save consumption and reduce the work times, the reaction time of the

hydrothermal reaction would be fixed at 12 hours.

5.3.2.3 Effect of Doping Content on the Optical Property of the ATO Nanoparticles

The antimony element in ATO do not only affect the particle size of nanoparticles, but also has impact on the optical properties of the semiconductors. As shown in the previous research, when the Sb% is higher than 30%, the impure crystallization related with antimony oxide would be in nanoparticles, which means that the Sb% should be lower than 30% [106]. Hence, this section investigated the morphology and optical property of different samples in different doping content. The steps of experiment were conducted as in the 5.2.1. The reaction temperature was maintained at 230°C. The reaction time would be kept at 12 hours, and the Sb% would be in 5%, 10%, 15%, and 20%.

The morphology of different samples was recorded by TEM images as shown in figure 5.9. It could be found that with the Sb% increase, the particle size distribution of ATO would be decreased. This is because the ionic radius of Sn^{4+} (0.69Å) is higher than Sb^{5+} (0.61Å), and the lattice imperfection and volume shrinkage should lead the particle size decrease when the Sn^{4+} is substituted via a competition mechanism between the oxygen vacancy generative Sb^{5+} and the oxygen vacancy compensating Sb^{3+}. However, when the Sb% was higher than 15%, it exhibited almost same particle size distribution between sample C'' and sample D''. The reason is that the Sb% is tend to saturation which has little effect on the particle size, meanwhile, when the particle size tends to small, the surface area of the nano ATO would be increased which would lead to

conglomeration of nanoparticles.
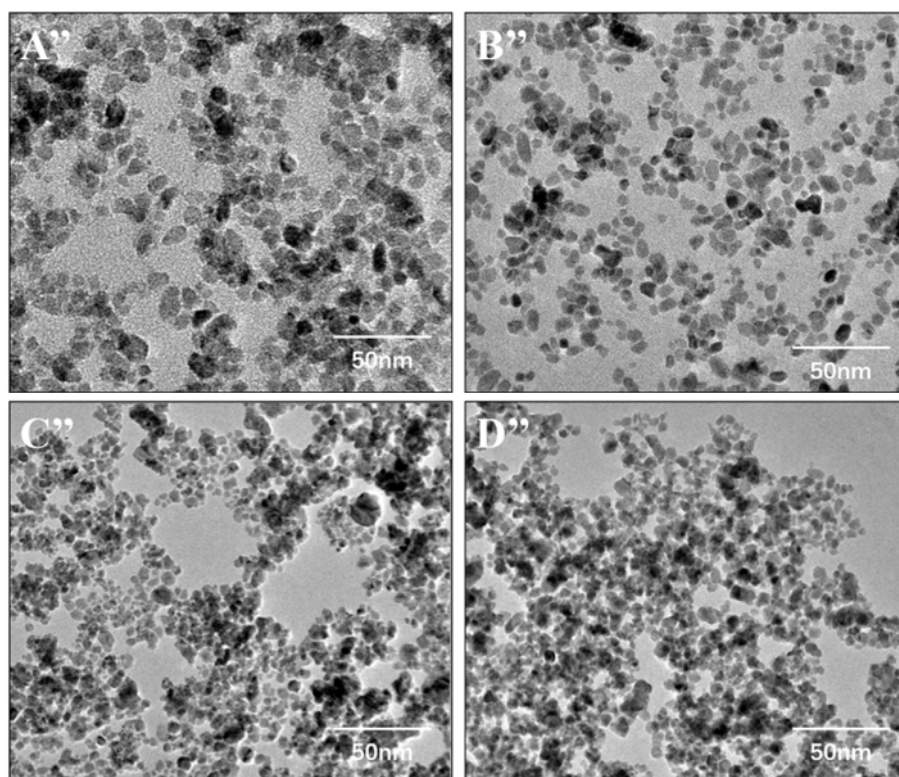
Figure 5.9 TEM images of different samples with different Sb%

A": 5%, B": 10%, C": 15% and D": 20%

The figure 5.10 shows the XRD pattern of different samples with different Sb doping content. It could be found that the peaks position would not be changed but the intensity of the peaks would be decreased with the Sb doping content be enhanced. The reason is that the crystallinity of nanoparticles reduced by the lattice distortion and particle size reduction, when the Sn^{4+} was replaced by Sb^{5+} and Sb^{3+}. This behavior is consistent with the TEM and morphology analyses.

Hence, to obtain a small size and high crystalline nanoparticle, the Sb doping

content should be considered carefully.
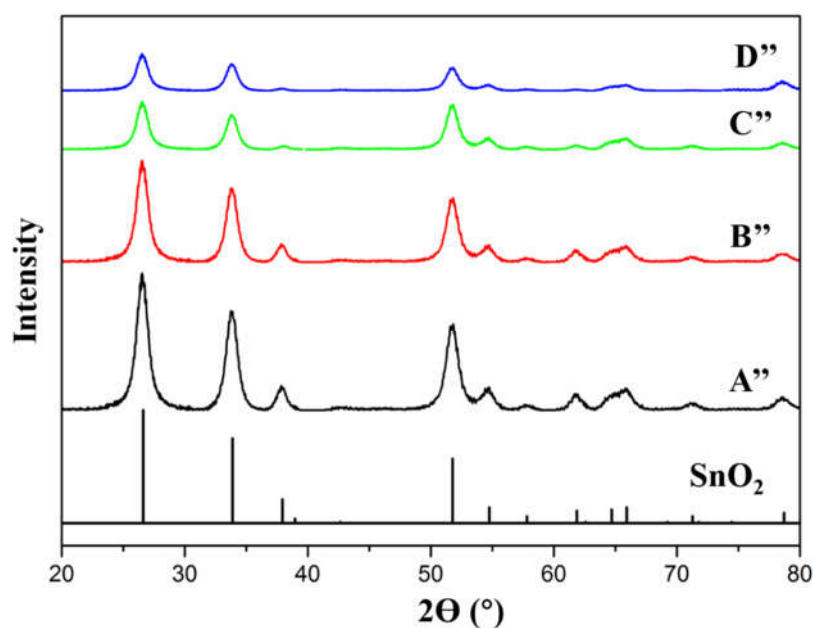
Figure 5.10 XRD pattern of different samples with different Sb%

A": 5%, B": 10%, C": 15% and D": 20%

UV-Vis-NIR transmittance can accurately represent the optical properties of the ATO nanoparticles. The figure 5.11 shows the UV-Vis-NIR transmittance of different samples with different Sb doping content. It could be found that all the samples exhibited a high transmittance in the visible light range of 380~780nm, and a high blocking rate in the NIR light range of 780~2500nm. The sample with the Sb% of 10% present the highest visible light transmittance. As the previous research, the Sb doping could increase the carrier concentration and plasma resonance frequency, which could change the optical properties of the semiconductors, especially the absorption and reflection of the visible light and NIR light. Nevertheless, the lattice distortion of the

ATO nanoparticles would increase with the Sb% further increase, which could lead the carrier concentration reduce and visible light transmittance decrease. Hence, 10% of the Sb doping content in ATO nanoparticles was the optimum point in the consideration to carrier concentration and electronic mobility, which exhibited a high visible light transmittance and excellent NIR light blocking rate.
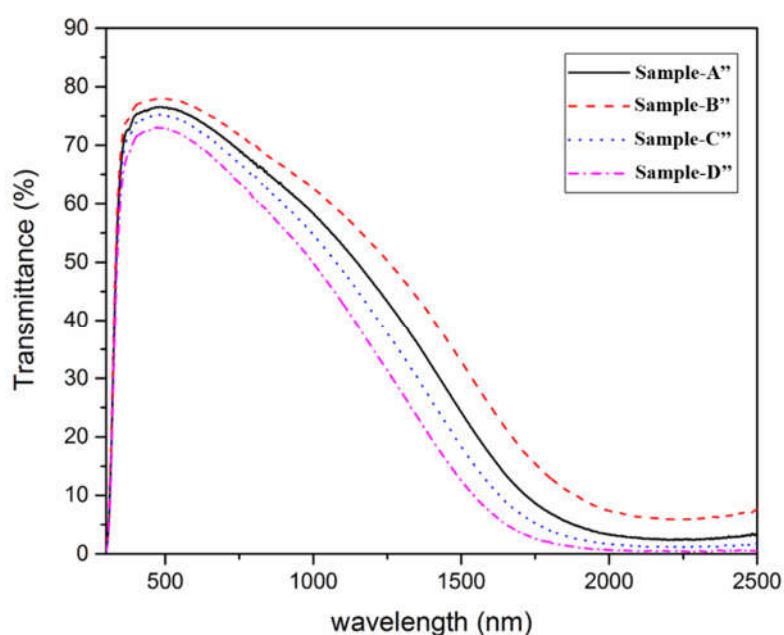
Figure 5.11 UV-Vis-NIR transmittance of different samples with different Sb%

A": 5%, B": 10%, C": 15% and D": 20%

Owing to the above investigation that the optimum Sb doping content is 10%. The Figure 5.12 shows HRTEM image, SAED pattern and the EDX image of the ATO nanoparticles with the Sb doping content of 10%. The reaction time and the reaction temperature were 12 hours and 230°C, respectively. The HRTEM image shows that the particles size of the ATO was around 10nm. The SAED pattern taken form a part of the

ATO nanoparticles in figure 3.12a are shown in figure 3.12b, which can be found that

the nanoparticles possess interplanar spacings of 2.63 and 3.37Å corresponding to the

(110) and (101) planes, respectively. The EDX of the ATO (Figure 3.12c) samples

which can be found that the major elemental composition are Sn, Sb and O and without

impurity element. In addition, the mole ration of Sb:Sn was 1:9, which further indicate

the Sb doping content was 10%.
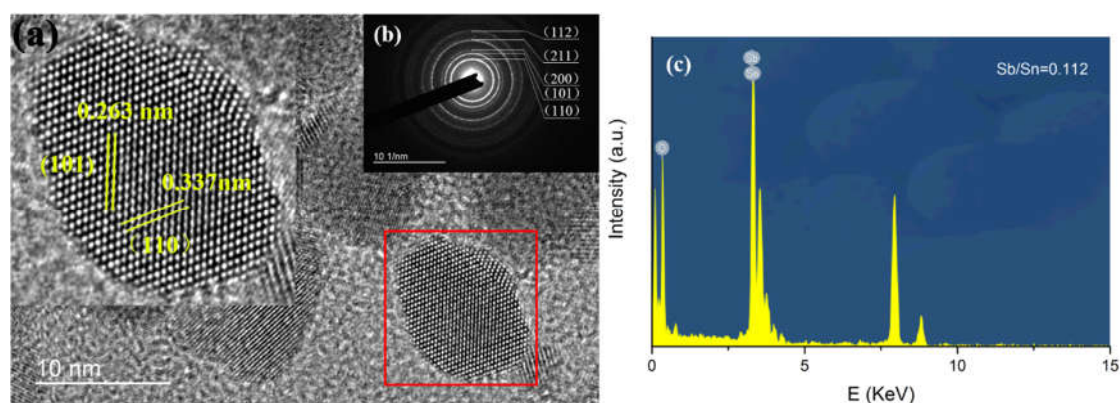
Figure 5.12 a: HRTEM image of the ATO nanoparticles; b: SAED pattern of the ATO
nanoparticles; c: EDX image of the ATO nanoparticles

5.3.3 Effect of Dispersing Process on the Stability of the ATO Aqueous Solution

**5.3.3.1 Effect of Different dispersing agent on the Stability of the ATO Aqueous
Solution**

The dispersing agents applied in nanoparticles aqueous dispersion have great

varieties and can be divided into two major categories, surface active agent and silane

coupling agent. In this thesis, the effect of four kinds of common dispersing agents on

the stability of the ATO aqueous solution were investigated. They were PVP (polymer

surface active agent), SN5040 (ionic surface-active agent), KH550 (silane coupling agent), SIM6492.72 (high active silane coupling agent). The steps of experiment were conducted as in the 3.2.2. The pH of the aqueous was adjusted in 9 by ammonium hydroxide. The physical dispersing method was high speed mechanical agitation and the stirring time, and the stirring rate were 2 hours and 5000rpm, respectively.
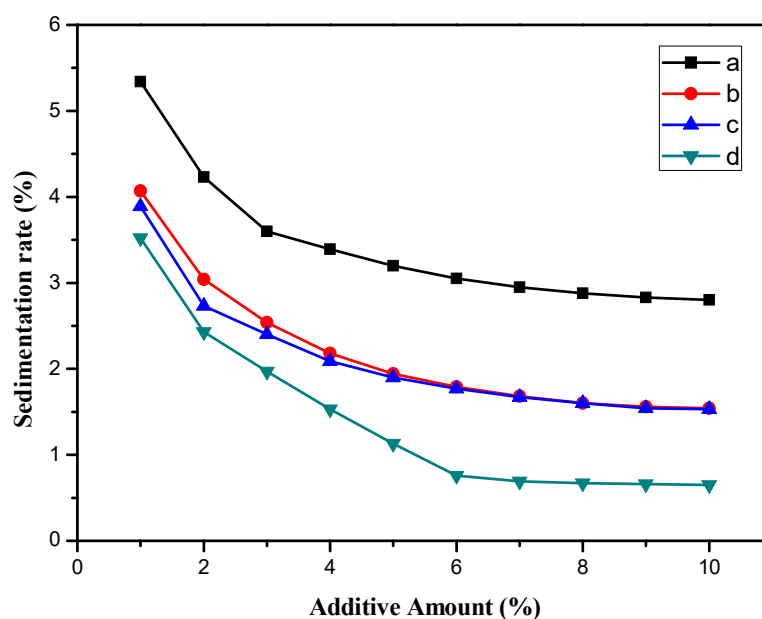
Figure 5.13 The sedimentation rate of ATO dispersion with different dispersing agent
(a: PVP; b: SN5040; c: KH550; d: SIM6492.72)

Figure 5.13 shows the sedimentation rate of ATO dispersion with different dispersing agent in different additive amount. The standing time of the samples was 7 days. It could be found that 4 dispersing agents had positive effect on ATO aqueous dispersion and the sedimentation rate exhibited the dispersion effect of SIM6492.72 > KH550 > SN5040 > PVP. Besides, with the additive amount higher than 6%, the sedimentation rate tended to a fixed value. Hence, in the ATO nanoparticles dispersion,

the optimum and the content of dispersing agent was SIM6492.72 and 6%, respectively.

3.3.3.2 Different pH Value Impact on the stability of the ATO Aqueous Solution

Zeta potential of ATO aqueous dispersion was decided by the pH value of solution. According to the DLVO theory, the high absolute value of the Zeta potential means the large electrostatic repulsion of nanoparticles electrical double layer, which leads to mutual repulsion of nanoparticles and keeps the stability of ATO aqueous dispersion. This experiment would test the sedimentation rate and the Zeta potential of ATO dispersion with different pH value and the optimum pH value would be considered. The steps of the dispersion method followed 5.2.3, and the pH value was adjusted by hydrochloric acid and ammonium hydroxide. The dispersing agent was SIM6492.72 in this experiment and the content was 6%. The physical dispersing method was high speed mechanical agitation and the stirring time and stirring speed was 2 hours and 5000rpm, respectively.

Figure 5.14 shows the sedimentation rate of ATO dispersion with different pH value. It could be found that the sedimentation rate of ATO dispersion was always exhibited low speed at different pH value, which means the ATO aqueous dispersion was stabled. When the pH value range is 8-10, the ATO aqueous shown an excellent dispersion. When the pH value is 9, the sedimentation rate of ATO dispersion was the lowest, which can be speculated that the absolute value of the Zeta potential is the largest with the pH value is 9.
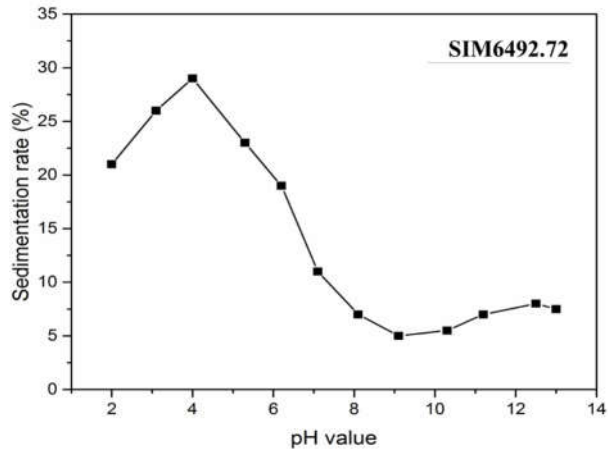
Figure 5.14 The sedimentation rate of ATO dispersion with different pH value

Figure 5.15 shows the Zeta potential of ATO aqueous dispersion at different pH value. It could be found that Zeta potential was positive value when the pH is lower than 4 which means the particle surface carry the negative charge, and the Zeta potential was negative value when the pH value is higher than 4 which means the particle surface carries the positive charge. With the further increase of the pH value, the Zeta potential gradually increase. When the pH value was 9, the absolute value of the Zeta potential was the largest, which means the system was the most stabled. This result was consistent with figure 3.14 exhibiting.
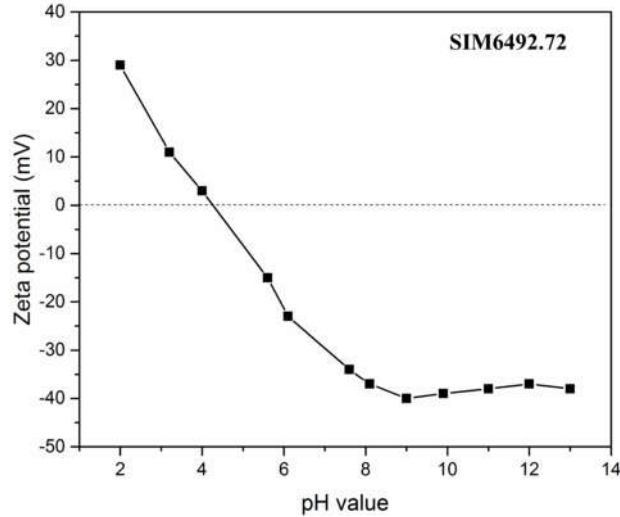
Figure 5.15 The Zeta potential of ATO dispersion with different pH value

5.3.3.3 Effect of Different Physical Dispersing Method on the stability of the ATO Aqueous Solution

According to the above experiment, the ATO dispersion with high speed mechanical agitation exhibited a less-than-ideal stability, due to the stratification of the ATO dispersion after 7 days. Hence, consideration of the optimized dispersing method was very important. The stability of the ATO aqueous dispersion with different physical dispersing methods were investigated in this experiment.

To consider the stability of ATO aqueous dispersion, the secondary particle size of the samples would be measured by Mastersizer 3000 laser particle analyzer. The experiment steps were followed the 5.2.3, and the pH value was 9, which was adjusted by ammonium hydroxide. The dispersing agent was SIM6492.72. The physical methods were high speed mechanical agitation, ball-milling dispersion and ultrasonic dispersion. The stirring speed and stirring time of high-speed mechanical agitation was 5000rmp and 6 hours, respectively. The ball-milling dispersion was applied in planetary

ball mill with 0.3mm alumina toughened zirconia bead in 6 hours. The fluctuating

frequency and the ultrasonic time was 20KHz and 6 hours, respectively.
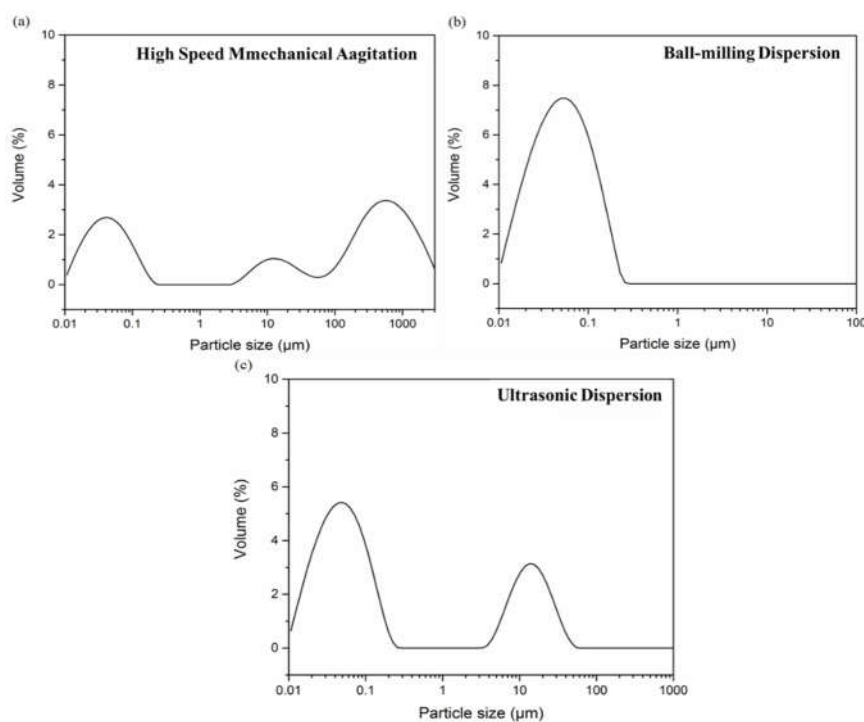
Figure 5.16 The particle size distribution of ATO dispersion with different dispersion methods：(a) mechanical stirring, (b) ball-milling dispersion, (c) ultrasonic dispersing

Figure 5.16 shows the secondary particle size distribution of ATO aqueous

dispersion with different physical dispersion methods. It could be found that the ATO

dispersion with high speed mechanical agitation exhibited a lowest stability due to the

3 peaks in the curve, and the largest secondary particle size is higher than 1000um,

which was caused by the serious aggregation of nanoparticles in the ATO aqueous. The

ATO dispersion with ball-milling dispersion exhibited a highest stability due to the

unimodal distribution and the narrow diameter distribution of the secondary particle

size. After calculating, the average particle size of the ATO aqueous dispersion with ball-milling was 28.1nm. The ATO aqueous dispersion was processed by ultrasonic dispersion with a narrow diameter distribution but the curve exhibited two peaks. Hence, the optimum physical dispersion method of ATO aqueous is ball-milling dispersion.

5.4 Conclusion

In this chapter, the ATO nanoparticles were synthesis by the controllable hydrothermal reaction and dispersed in water with surfactant. The effects of doping content, reaction time and reaction temperature on the morphology and optical properties of ATO were investigated, by which the optimum reaction conditions were obtained. The effects of the kind and concentration of dispersant, pH value and dispersion methods were also analyzed. The details are as follows:

1. The doping content of Sb was 10%, the reaction temperature was 230℃ and the reaction time was 12 h.

2. Using surfactant agent SIM6492.72 with 6wt%, adjusting pH value to 9 and the size of zirconia ball milling to 0.3 mm during 6 h could obtain stable ATO aqueous dispersion. The secondary particles size of aqueous dispersion was unimodal distribution and the narrow diameter distribution. Meanwhile, the average secondary particle size of the ATO aqueous dispersion was 28.1nm.

5.5 Reference

[1] Frasca, S., von Graberg, T., Feng, J. J., Thomas, A., Smarsly, B. M., Weidinger, I. M., ... & Wollenberger, U. (2010). Mesoporous indium tin oxide as a novel platform for bioelectronics. *ChemCatChem*, *2*(7), 839-845.

[2] Müller, V., Rasp, M., Rathouský, J., Schütz, B., Niederberger, M., & Fattakhova-Rohlfing, D. (2010). Transparent Conducting Films of Antimony-Doped Tin Oxide with Uniform Mesostructure Assembled from Preformed Nanocrystals. *Small*, *6*(5), 633-637.

[3] Hou, K., Puzzo, D., Helander, M. G., Lo, S. S., Bonifacio, L. D., Wang, W., ... & Ozin, G. A. (2009). Dye-Anchored Mesoporous Antimony-Doped Tin Oxide Electrochemiluminescence Cell. *Advanced Materials*, *21*(24), 2492-2496.

[4] Yiu, H. H., & Wright, P. A. (2005). Enzymes supported on ordered mesoporous solids: a special case of an inorganic–organic hybrid. *Journal of Materials Chemistry*, *15*(35-36), 3690-3700.

[5] Guo, K., Hu, Y., Zhang, Y., Liu, B., & Magner, E. (2010). Electrochemistry of nanozeolite-immobilized cytochrome c in aqueous and nonaqueous solutions. *Langmuir*, *26*(11), 9076-9081.

[6] El Kasmi, A., Leopold, M. C., Galligan, R., Robertson, R. T., Saavedra, S. S., El Kacemi, K., & Bowden, E. F. (2002). Adsorptive immobilization of cytochrome c on indium/tin oxide (ITO): electrochemical evidence for electron transfer-induced conformational changes. *Electrochemistry Communications*, *4*(2), 177-181.

sics Letters, 2010, 96(26):2379.

Chapter 6   Development and Investigation of Nano Cs_xWO_3 and Cs_xWO_3 Aqueous Dispersion

6.1 Introduction

It is well known that the bandgap width of tungsten trioxide is 2.62eV [1], thus it is transparent in the region of visible and infrared light. High metal conductivity and strong near-infrared absorption properties can be obtained by reducing oxygen content or by increasing the third-party elements to introduce free electrons into the crystal. The oxygen deficiency of tungsten oxide results in a complex ordered structure known as the Magneli structure, and the addition of a third element is the introduction of positive ions into the tungsten bronze structure. When the alkali metals (Li, Na, K, Rb, Cs) are incorporated into the crystal structure of trioxide, the electrons of the alkali metal will improve the conduction band of tungsten trioxide and form a free electron plasma resonance. Thus, tungsten bronze has unique electrical and optical properties [2]. Study found that cesium tungsten bronze Cs_xWO_3 in visible region (380 ~ 780 nm) had high optical transmittance. Meanwhile, compared with other materials such as ITO transparent conductive oxide, ATO, has better infrared absorption property in near infrared region (780 ~ 2500 nm), which can be the core of transparent insulation coating material and an optional function material [3].

Nowadays, Cs_xWO_3 is synthesized by means of two reaction pathways, namely the reaction route [4] and the high pressure wet chemical route [5] (hydrothermal

reaction and solvent heat reaction). There are also a few researchers to prepare Cs_xWO_3 by inductively coupled thermal-plasma technology [6] and the process of mixing beads. The traditional method for the preparation of Cs_xWO_3 requires harsh reaction conditions such as high temperature, and the synthesis reaction requires additional reaction steps. The size of the nanoparticles is often not well controlled. The hydrothermal reaction and solvent thermal reaction can produce nanoparticle materials with controllable particle size at a lower temperature.

Therefore, this chapter adopts the solvent thermal preparation to synthesize Cs_xWO_3 nanoparticles and use water as dispersion medium to prepare Cs_xWO_3 nanoparticles aqueous dispersion. The experiment focuses on the influence of reaction time and reaction temperature on the particle size and morphology, and spectral transmittance curve of Cs_xWO_3. At the same time, the effects of different dispersants and dispersants on the stability of Cs_xWO_3 aqueous dispersion were investigated. Using transmission electron microscopy (TEM), X-ray diffraction (XRD), scattering spectroscopy (EDS), laser particle size instrument to characterize particle size distribution and particle morphology of Cs_xWO_3 nanoparticles, using UV-Vis-NIR spectrophotometer to measure the transmittance of the Cs_xWO_3 in 300~2500 nm wavelength region and, investigate its infrared absorption properties.

6.2 Experiment

6.2.1 Development of Cs_xWO_3 nanoparticles

Nano Cs_xWO_3 was synthesized by controllable hydrothermal reaction, and the

details of the technical process are as followed (Figure 6.1)

1) WCl$_6$ and CsOH.H$_2$O powder was measured with analytical balance and mixed in an agate mortar as a mixture A. The Cs% was according to the equation 6.1.

$$Cs\% = \frac{Cs\ mol}{Cs\ mol+W\ mol} \times 100\%$$ (6.1)

2) The mixture A was added with dissolving in the absolution ethyl alcohol, and mechanical stirring in 10min with the speed of 300r/min. A yellow solution would be obtained. Then acetic acid and polyvinyl pyrrolidone (PVP, M=50000) would be added in the solution, as mixture B.

3) The mixture B was transferred to PPL liner and sealed into stainless steel shell. The hydrothermal reactor would be placed into air dry oven at 220℃.

4) After 12 hours, the product in PPL would be cleaned with deionized water and absolution ethyl alcohol to remove the ionic impurity. Then the cleaned product would be transfer into vacuum drying oven at 100℃. After drying, the sky-blue Cs$_x$WO$_3$ nanoparticles, as shown in figure 6.2, would be obtained.
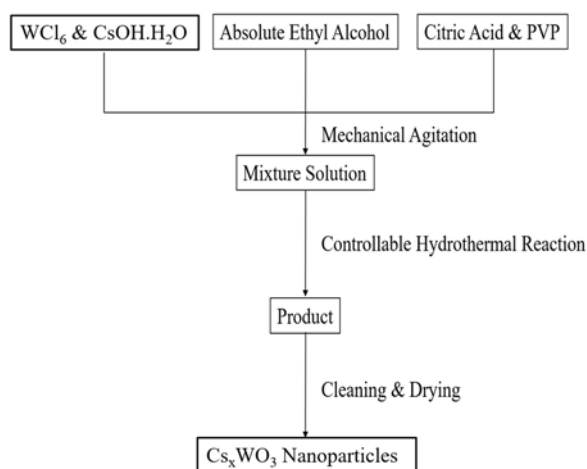
Figure 6.1 The process flowchart of the preparation of Cs$_x$WO$_3$ nanoparticles
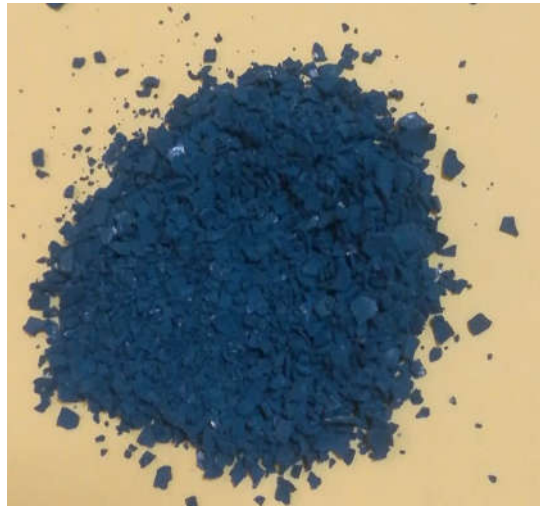
Figure 6.2 The Cs$_x$WO$_3$ nanoparticles fabricated by hydrothermal reaction

6.2.2 Development of Cs$_x$WO$_3$ aqueous solution

A certain quality of the Cs$_x$WO$_3$ nanoparticles, which were measured by analytical balance, were mixed with dispersing agent, hydrochloric acid and deionized water. A suspension liquid would be obtained after mechanical agitation and ultrasonic dispersion. The suspension then was placed into agate jar. After ball milling, the final Cs$_x$WO$_3$ aqueous solution would be fabricated. The details of the process are shown in figure 6.3.
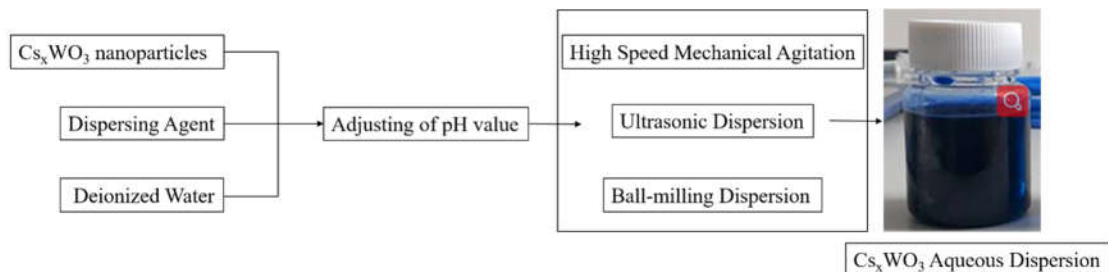
Figure 6.3 The process flowchart of the preparation of Cs$_x$WO$_3$ aqueous dispersion

6.3 Results and discussion

6.3.1 Effect of reaction conditions on the morphology and properties of the Cs_xWO_3 nanoparticles

6.3.1.1 Effect of reaction temperature on the morphology of the Cs_xWO_3 nanoparticles

This thesis investigated the effect of reaction temperature on the morphology of the Cs_xWO_3 nanoparticles. Cs_xWO_3 nanoparticles were fabricated through controllable thermal insulation coating which is conducted as 6.2.1. The reaction temperature was maintained at 180°C, 200°C, 220°C and 240°C. The reaction time was kept at 12 hours, and the Cs% was kept in 20%. Meanwhile, the citric acid content was 5wt%.

The figure 6.4 shows the TEM images of the Cs_xWO_3 nanoparticles under different controllable hydrothermal reaction temperature. It could be found that the Cs_xWO_3 nanoparticles in different reaction temperature exhibited the similar particle size. However, the edge sharpness of Cs_xWO_3 nanoparticle was increased with the reaction temperature enhanced. In figure 6.4A, there are same lager size particles which were WO_3 powder as measured in XRD pattern. It is because that the low-purity of the Cs_xWO_3 nanoparticles would be fabricated in low reaction temperature. In figure 6.4B, the nanoparticles agglomeration is more than other nanoparticles in higher temperature as shown in figure 6.4C and figure 6.4D. It is because that the larger sized WO_3 powder would be dissolved in high temperature and join the grain growth.
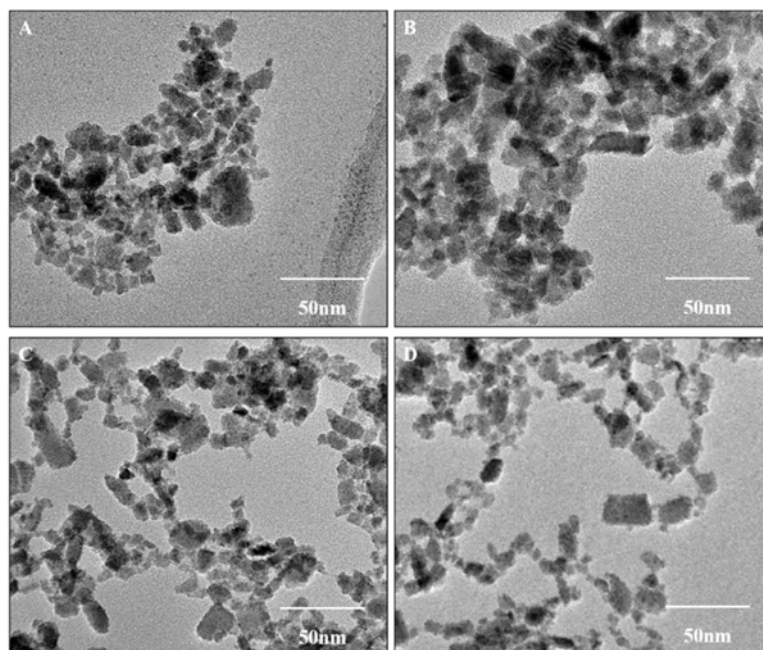
Figure 6.4 The TEM images of Cs_xWO_3 nanoparticles in different reaction
temperature (A: 180°C, B: 200°C, C: 220°C, D: 240°C)

Figure 6.5 shows the XRD pattern of the Cs_xWO_3 nanoparticles in different

reaction temperature. It could be found that the peak positions of all the samples were

agree with the reflections of $Cs_{0.33}WO_3$(Ref. No.83-1334). When the reaction

temperature elevated, the intensity of the peak was increased, which means the

crystalline of the Cs_xWO_3 nanoparticles was increased. However, the line of sample A

(180°C) exhibited a peak position, inconformity with the reference ($Cs_{0.33}WO_3$), is the

characteristic peak of WO_3, which further proofs the larger sized particles in TEM and

the incomplete reaction in low reaction temperature. However, when the reaction

temperature was enhanced to 200°C, the impurity of the peak intensity was decreased,

and the intensity of the characteristic peak (Ref. $Cs_{0.33}WO_3$) was increased and more

obvious. When the reaction temperature was enhanced to 220°C, the impurity of the

peak was disappeared, which was well agree with the reflections of $Cs_{0.33}WO_3$(Ref.

No.83-1334). Hence, to obtain a fully crystallization of Cs_xWO_3 nanoparticles without impurity crystal, the reaction temperature should be higher than 200°C.
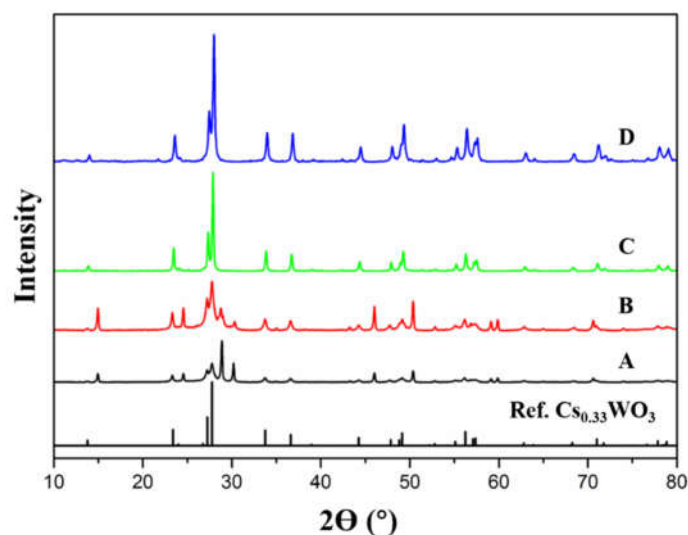
Figure 6.5 XRD pattern of the Cs_xWO_3 nanoparticles in different reaction temperature
(A: 180°C, B: 200°C, C: 220°C, D: 240°C)

The WO3 obtained in low reaction temperature do not affect the transmittance in visible light range and NIR light range, which cannot be applied in NIR shielding films. Figure 6.6 shows the UV-Vis-NIR transmittance of Cs_xWO_3 aqueous dispersion in different reaction temperature. It could be found that sample A (reaction temperature was 180°C) exhibited a high transmittance both in visible light range and NIR light range. With the temperature increased, the degree of crystallinity would be enhanced, which would improve the blocking rate of NIR light. According to the UV-Vis-NIR transmittance of Cs_xWO_3 aqueous dispersion, the optimum reaction temperature was 220°C, due to sample C exhibited high NIR light blocking rate and excellent visible light transmittance.
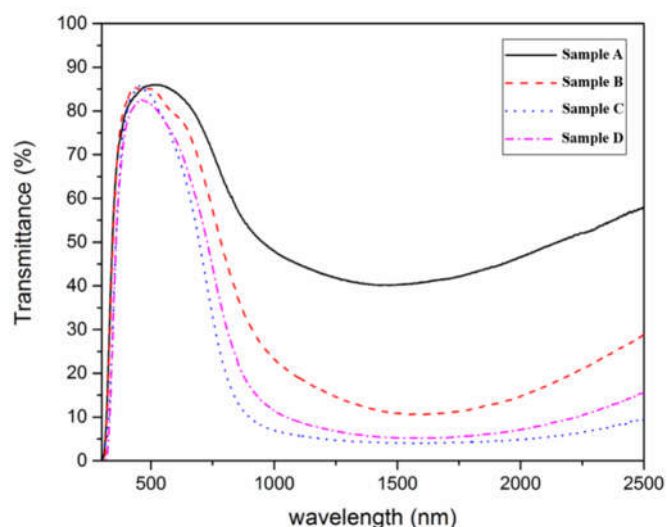
Figure 6.6 The UV-Vis-NIR transmittance of Cs_xWO_3 aqueous dispersion in different hydrothermal reaction temperature

(A: 180°C, B: 200°C, C: 220°C, D: 240°C)

6.3.1.2 Effect of reaction time on the morphology of the Cs_xWO_3 nanoparticles

In this section, the effect of the reaction time on morphology of the Cs_xWO_3 nanoparticles had been investigated. Cs_xWO_3 nanoparticles were fabricated through controllable thermal insulation coating which is conducted as 6.2.1. The reaction time of the Cs_xWO_3 nanoparticles synthesis was 6h, 12h, 24h and 48h, respectively. The Cs% was 20% in the Cs_xWO_3 hydrothermal reaction. The reaction temperature and citric acid content was 220°C and 5wt%, respectively.

Figure 6.7 shows the TEM images of the Cs_xWO_3 nanoparticles at different reaction time. It could be found that the particle size of the Cs_xWO_3 would slightly increase with the reaction time extension, due to the Ostwald Ripening during the

hydrothermal reaction, and the dispersity of the Cs_xWO_3 nanoparticles was reduced with the reaction time extension, especially sample C (reaction time was 24 hours) and sample D (reaction time was 48 hours). Hence, the reaction time should not be longer than 12 hours.
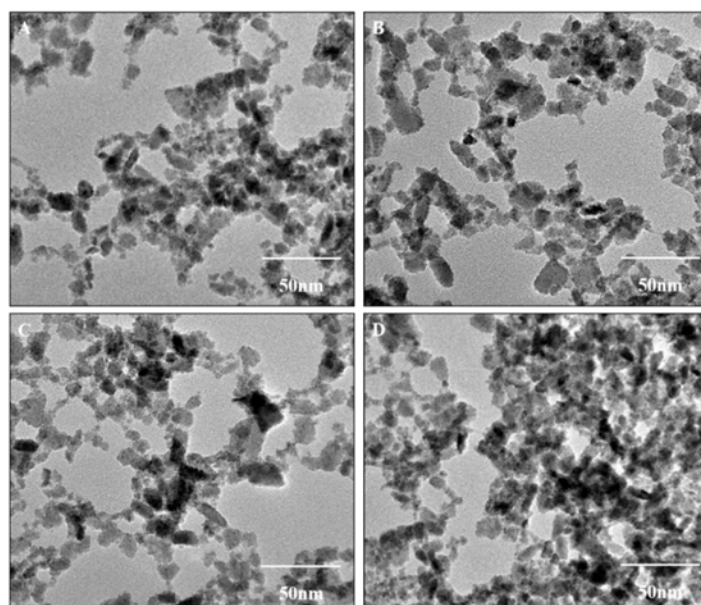
Figure 6.7 The TEM image of the Cs_xWO_3 nanoparticles in different reaction time (A: 6h, B: 12h, C: 24h, D: 48h)

Figure 6.8 shows the XRD pattern of the Cs_xWO_3 nanoparticles at different reaction time. It could be fund that the intensity of the characteristic peak was increased with the reaction time extension, which is consistent with the change of TEM image showing. When the reaction time was longer than 12 hours, the crystallization of nano Cs_xWO_3 reacted completely and the nanoparticles crystal grown perfectly. The high intensity and the high acutance of the characteristic peak could be exhibited in sample B, sample C and sample D, which indicated that the reaction time of the Cs_xWO_3

nanoparticles synthesis should be longer than 12 hours.
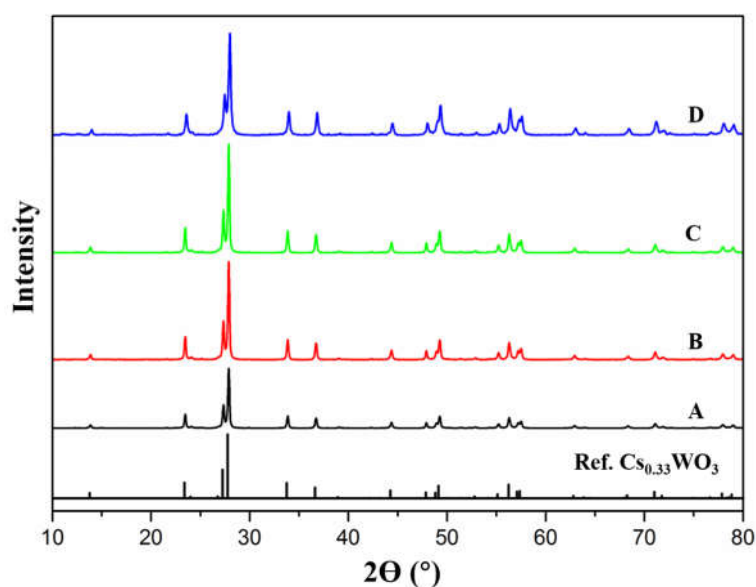
Figure 6.8 The XRD pattern of the Cs_xWO_3 nanoparticles in different reaction time
(A: 6h, B: 12h, C: 24h, D: 48h)

To reduce the time cost and process, the optimum hydrothermal reaction time was 12 hours. In this reaction time, the Cs_xWO_3 nanoparticles exhibited a fully crystal structure and completed growth of grain.

6.3.1.3 Effect of doping content on the morphology of the Cs_xWO_3 nanoparticles

The cesium element in Cs_xWO_3 nanoparticles not only affects the morphology of nanoparticles but also has impacts on the optical properties on the semiconductors, thus it is the important factor in hydrothermal reactions. As in the previous research, to enhance the thermal stability of the Cs_xWO_3, one of the M_xWO_3 group, the Cs% should be lower than 40%. Hence, this section investigated the morphology and optical property of different samples in different doping content. The steps of experiment were

conducted as in 6.2.1. The reaction temperature and the reaction time was maintained at 220°C and 12 hours, respectively. The Cs% would be in 20%, 25%, 30%, 35%, and the citric acid content in the hydrothermal reaction was 5wt%.

The morphology of different samples was recorded by TEM images as shown in Figure 6.9. It could be found that with the Cs% increase, the particle size distribution of Cs_xWO_3 would be decreased. This is because the lattice imperfection and volume shrinkage should lead the particle size decrease when the Cs^+ is substituted via a competition mechanism between the oxygen vacancy generative W^{6+} and the oxygen vacancy compensating W^{5+}. However, when the Cs% was 35%, the surface energy of the Cs_xWO_3 nanoparticles would lead to conglomeration of nanoparticles.
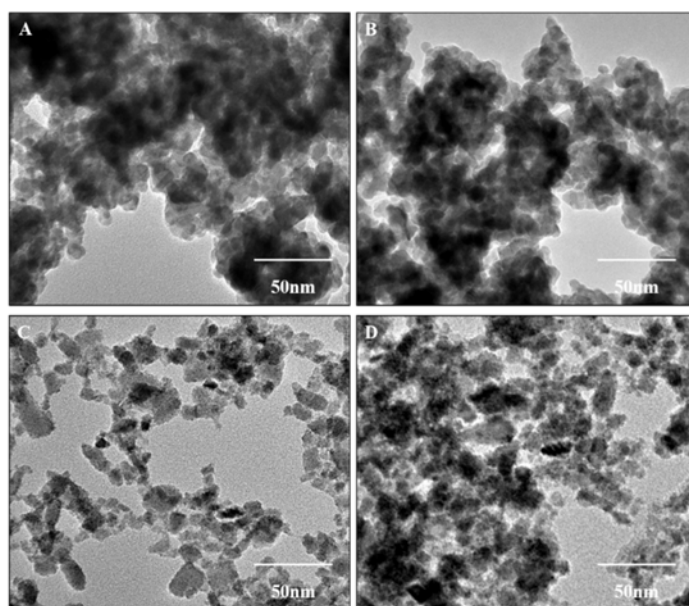
Figure 6.9 The TEM image of the Cs_xWO_3 nanoparticles in different Cs%

(A: 20%; B: 25%; C: 30%; D: 35%)

Figure 6.10 shows the XRD pattern of Cs_xWO_3 nanoparticles in different Cs%. It could be fund that the peaks position would not be changed but the intensity of the peaks would be decreased with the Cs% be increased. The reason that the crystallinity of nanoparticles reduced by the lattice distortion and particle size reduction, when the W element in the crystal was replaced by Cs element. This behavior is consistent with the TEM and morphology analyses. Hence, to obtain a small sized and high crystalline nanoparticle, the Cs doping content should be considered carefully.
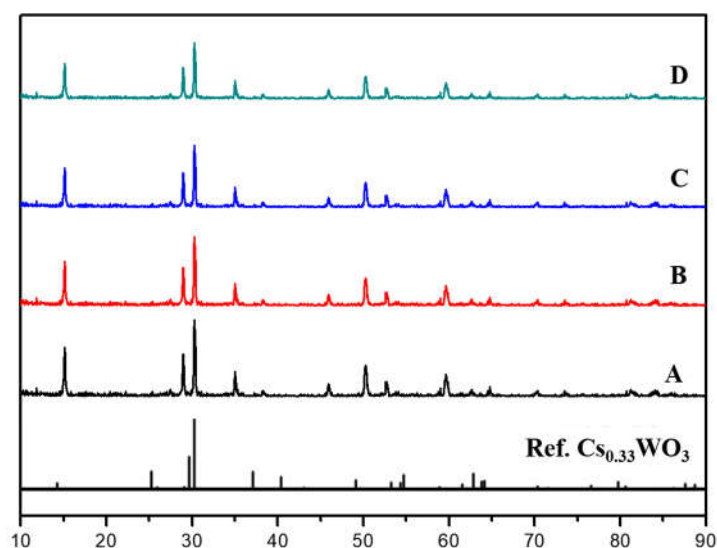
Figure 6.10 The XRD pattern of Cs_xWO_3 nanoparticles in different Cs%

(A: 20%; B: 25%; C: 30%; D: 35%)

UV-Vis-NIR transmittance can accurately represent the optical properties of the Cs_xWO_3 nanoparticles. Figure 4.11 shows the UV-Vis-NIR transmittance of Cs_xWO_3 nanoparticles with different Cs doping content. It could be found that all the samples exhibited a high transmittance in the visible light range of 380~780nm, and a high

blocking rate in the NIR light range of 780~2500nm, especially in the range of 780-1500nm. According to the previous research, the Sb doping could increase the local surface plasma resonance, which could change the optical properties of the semiconductors, especially the absorption and reflection of the visible light and NIR light. Nevertheless, the lattice distortion of the Cs_xWO_3 nanoparticles would be increased with the Cs% further increased, which could lead to the carrier concentration reduce and visible light transmittance decrease. Hence, 30% of the Cs doping content in Cs_xWO_3 nanoparticles was the optimum point in consideration of carrier concentration and electronic mobility, which exhibited a high visible light transmittance and excellent NIR light absorption.
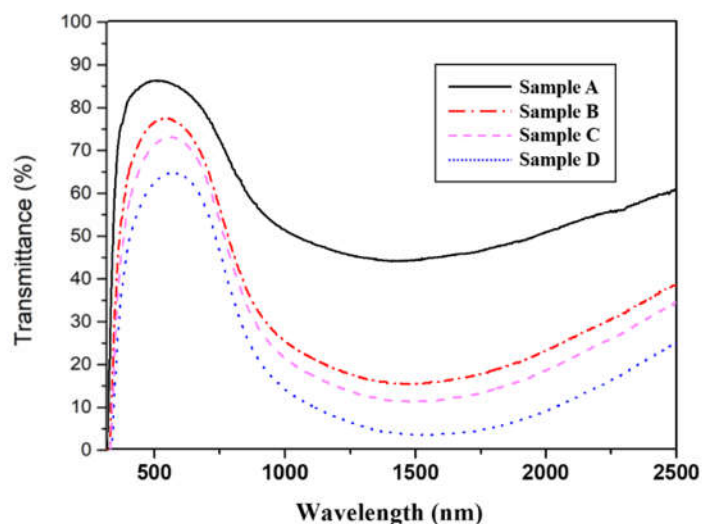
Figure 6.11 The UV-Vis-NIR transmittance of Cs_xWO_3 nanoparticles in different Cs% (A: 20%; B: 25%; C: 30%; D: 35%)

6.3.1.4 Effect of citric acid content on the morphology and optical property of Cs_xWO_3 nanoparticles

In the controllable hydrothermal reaction, the citric acid, as the surface end capping agent, can be selectively absorbed in the surface of nanoparticles, which can affect and control the growth of grain, agglomeration of nanoparticles, and stability of the nanoparticle dispersion. Hence, the citric acid content shows an important effect on the morphology and optical property of Cs_xWO_3 nanoparticles. The steps of controllable hydrothermal reaction were conducted as in 4.2.1. The reaction temperature and reaction time was 220°C and 12 hours, respectively. Meanwhile, the Cs% in the hydrothermal reaction was 30%. The citric acid content was maintained in 0wt%, 3wt%, 5wt% and 10wt%.

Figure 6.12 shows the TEM images of the Cs_xWO_3 nanoparticles in different citric acid content. It could be found that the sample, without citric acid, exhibited a large particle size which was belong to the "micron powder", and it shows an obvious aggregation of Cs_xWO_3 powder. After adding the citric acid, the Cs_xWO_3 particles through the hydrothermal reaction was belong to the "nano-powder", which exhibited an excellent dispersion and distinct morphology. The increasing of the citric acid would lead to a decrease of the Cs_xWO_3 nanoparticles size distribution. Plus, it is because that the electrostatic interactions between the nanoparticles, when the citric acid was absorbed on the surface of nanoparticles during the hydrothermal reaction. In figure 12C, the particle size distribution of nano Cs_xWO_3 was 10-25nm, and the particle edge was clear and distinct, when the citric acid content was 5wt%, which means a completed

crystalline Cs_xWO_3 nanoparticles was obtained. However, in figure 12D, when the citric acid content was 10wt%, the aggregation of Cs_xWO_3 nanoparticles was in the TEM image. It is because that high citric acid would prevent the growth of gain, and the small sized nanoparticle exhibited a high surface energy which caused a negative effect of the nanoparticle dispersion.
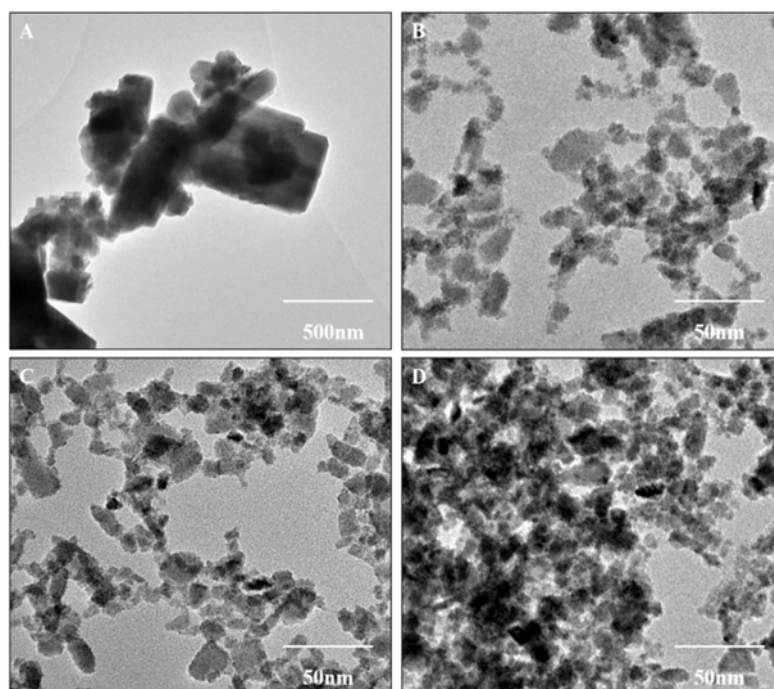
Figure 6.12 The TEM images of Cs_xWO_3 nanoparticles in different citric acid content
(A: 0wt%; B: 3wt%; C: 5wt%; D: 10wt%)

Figure 6.13 shows the XRD pattern of Cs_xWO_3 nanoparticles in different citric acid content. It could be found that the peak positions of all the samples were agree with the reflections of $Cs_{0.33}WO_3$(Ref. No.83-1334). As the citric acid content increased, the intensity of the peak would be slightly enhanced, which fit with the results of TEM images shown. However, there were some peaks in sample A did not agree with the

reflections of reference, which means there had some impurity crystal in the sample. These peaks position matched well with the characteristic peaks position of WO_3. That $Cs+$ was doping in the regular octahedron lattice of $WO6$ during the hydrothermal reaction to form the reduction state of Cs_xWO_3 ($Cs_x^+W_{1-x}^{6+}W_x^{5+}$) crystal. Hence, the $Cs+$ cannot dope into the $WO6$ crystal when the citric acid was not added in the hydrothermal reaction.
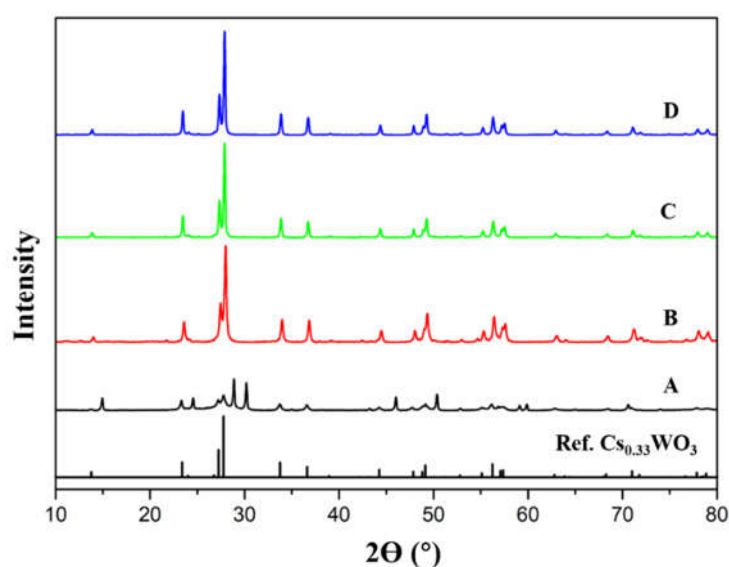
Figure 6.13 The XRD pattern of Cs_xWO_3 nanoparticles in different citric acid content
(A: 0wt%; B: 3wt%; C: 5wt%; D: 10wt%)

Figure 6.14 shows the UV-Vis-NIR transmittance of Cs_xWO_3 nanoparticles in different citric acid content. It could be found that all samples exhibited a high transmittance in visible light range (380-780nm). However, sample A exhibited a poor NIR light blocking which is caused by the high transmittance of WO_3 crystal in both visible light range and NIR light range. Sample B, sample C and sample D shows a

high blocking rate in the NIR light range (780-2500nm), The reason is that the local surface plasma resonance increased when the polarized charges increased by the Cs^+ doped. When the citric acid content was 5wt%, the NIR blocking rate was the highest, as shown in sample C.
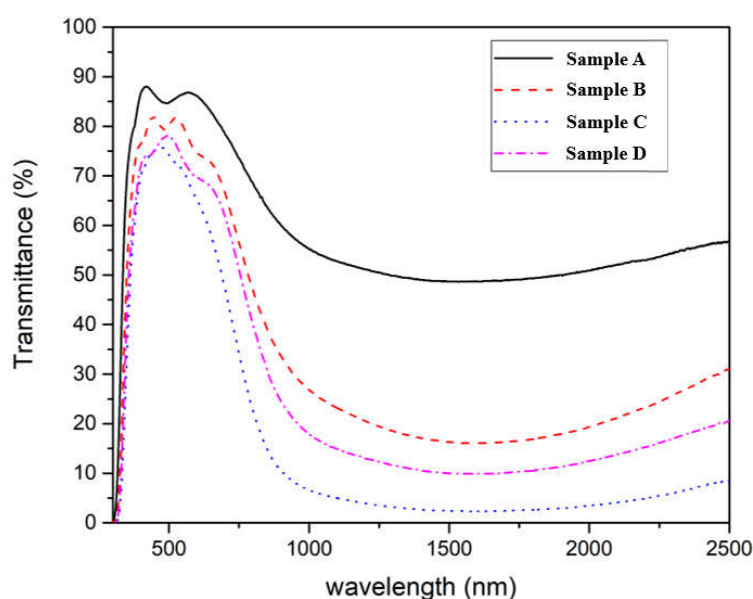
Figure 6.14 The UV-Vis-NIR transmittance of Cs_xWO_3 nanoparticles in different citric acid content (A: 0wt%; B: 3wt%; C: 5wt%; D: 10wt%)

Owning to the above investigation, the optimum citric acid content was 5wt%. Figure 6.15 shows the HRTEM image, SAED pattern and EDX pattern of Cs_xWO_3 nanoparticles in reaction conditions 5wt% of citric acid, 30% of Cs%, 220°C of reaction temperature, 12 hours of reaction time, respectively. Figure 6.15B shows that nanoparticles possess interplanar spacing of 3.21 Å corresponding to the (200), which is further indicated Cs_xWO_3 nanocrystal. The EDX of the Cs_xWO_3 (Figure 6.15C) samples which can be fund that the major elemental composition are Cs, W and O and

without impurity element.
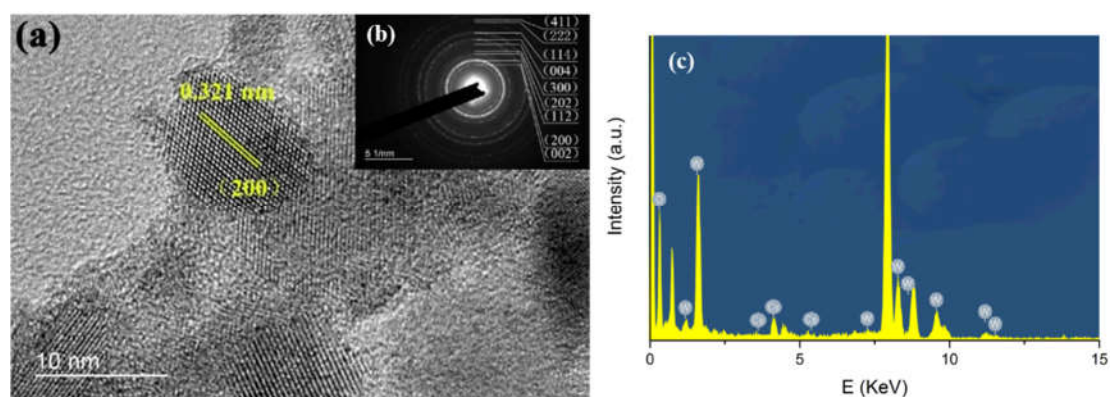
Figure 6.15 shows the HRTEM image(a), SAED pattern (b) and EDX pattern (c) of Cs_xWO_3 nanoparticles

6.3.2 Effect of dispersing process on the stability of the Cs_xWO_3 aqueous solution

6.3.2.1 Effect of different dispersing agents on the stability of the Cs_xWO_3 aqueous solution

In this thesis, the effect of four kinds of common dispersing agents, PVP, SN5040, KH550 and SIM6492.72, on the stability of the Cs_xWO_3 aqueous solution were investigated. The effect of pH value would not be investigated on this chapter, because it hardly affects the stability of the Cs_xWO_3 aqueous solution. The steps of experiment were conducted as in the 4.2.2, and the stirring time and the stirring rate were 2 hours and 5000rpm, respectively.

Figure 6.16 shows the sedimentation rate of the Cs_xWO_3 aqueous solution in different dispersants, and the sedimentation time was 7 days. It could be found that all the 4 dispersants can enhance the dispersion of Cs_xWO_3 aqueous solution. The results

show that the efficiency of dispersing agent A was the highest. Plus, the optimum of the SN5040 content in the dispersing process was 7wt%.
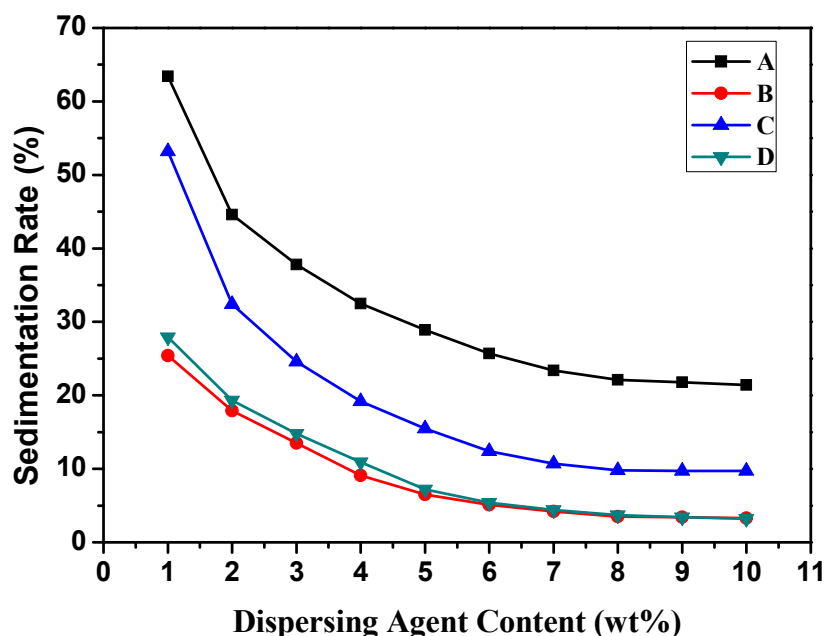
Figure 6.16 The sedimentation rate of the Cs_xWO_3 aqueous solution in different dispersants (A: PVP; B: SN5040; C: KH550; D: SIM6492.72)

6.3.2.2 Effect of different physical dispersion method on the stability of the Cs_xWO_3 aqueous solution

In this section, the effect of three different physical dispersion methods including high speed mechanical agitation, ball-milling dispersion, and ultrasonic dispersion on the stability of the Cs_xWO_3 aqueous solution would be investigated.

Due to the high stability of the Cs_xWO_3 aqueous solution dispersed by the ball-milling dispersion which exhibited no sedimentation after 15 days, the secondary particle size would be measured to represent the stability of the Cs_xWO_3 aqueous

solution. The experiment steps were followed the 4.2.3, and the dispersing agent was SN5040. The physical methods were high speed mechanical agitation, ball-milling dispersion and ultrasonic dispersion. The stirring speed and stirring time of high-speed mechanical agitation was 5000rmp and 6 hours, respectively. The ball-milling dispersion was applied in planetary ball mill with 0.3mm alumina toughened zirconia bead for 6 hours. The fluctuating frequency and the ultrasonic time were 20KHz and 6 hours, respectively.
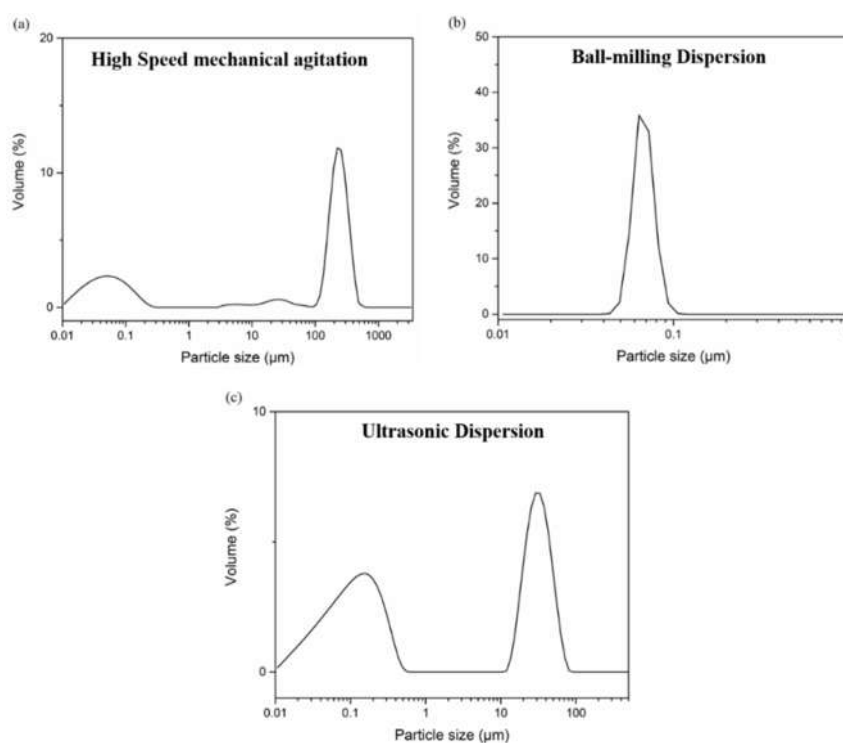
Figure 6.17 The secondary particle size distribution of the Cs_xWO_3 aqueous solution in different physical method. (a: High speed mechanical agitation; b: ball-milling dispersion; C: Ultrasonic dispersion)

Figure 6.17 shows the secondary particle size distribution of Cs_xWO_3 aqueous

solution with different physical dispersion methods. It could be found that the Cs_xWO_3 dispersion with high speed mechanical agitation exhibited the lowest stability due to some peaks in the curve, and the largest secondary particle size is higher than 1000um, which was caused by the serious aggregation of nanoparticles in the Cs_xWO_3 aqueous. The Cs_xWO_3 dispersion with ball-milling dispersion exhibited a highest stability due to the unimodal distribution and the narrow diameter distribution of the secondary particle size. After calculating, the average particle size of the ATO aqueous dispersion with ball-milling was 62.7nm. The Cs_xWO_3 aqueous dispersion with ultrasonic dispersion in a narrow diameter distribution but the curve exhibits two peaks. Hence, the optimum physical dispersion method of Cs_xWO_3 aqueous is ball-milling dispersion.

6.4 Conclusion

In this chapter, the Cs_xWO_3 nanoparticles were synthesis by the controllable hydrothermal reaction and dispersed in water with surfactant. The effects of citric acid content, doping content, reaction time and reaction temperature on the morphology and optical properties of Cs_xWO_3 were investigated, by which the optimum reaction conditions were obtained. The effects of the kind and concentration of dispersant, and dispersion methods were also analyzed. The details are as follows:

1. The doping content of Cs was 30%, the reaction temperature was 220℃ and the reaction time was 12 h.

2. By Using surfactant agent SN5040 of 7wt%, and the size of zirconia ball milling to 0.3 mm at 6 h could obtain stable Cs_xWO_3 aqueous dispersion. The secondary

particles size of aqueous dispersion was unimodal distribution and the narrow diameter distribution. Meanwhile, the average secondary particle size of the Cs_xWO_3 aqueous dispersion was 62.7nm.

6.5 Reference

[1] Koffyberg, F. P., Dwight, K., & Wold, A. (1979). Interband transitions of semiconducting oxides determined from photoelectrolysis spectra. *Solid State Communications*, *30*(7), 433-437.

[2] Srinivasarao, K., Rajinikanth, B., Pandurangarao, K., & Mukhopadhyay, P. K. (2012). Physical investigations on pulsed laser deposited nanocrystalline ZnO thin films. *Applied Physics A*, *108*(1), 247-254.

[3] Lynch, D. W., Rosei, R., Weaver, J. H., & Olson, C. G. (1973). The optical properties of some alkali metal tungsten bronzes from 0.1 to 38 eV. *Journal of Solid State Chemistry*, *8*(3), 242-252.

[4] Schirmer, O. F., Wittwer, V., Baur, G., & Brandt, G. (1977). Dependence of WO 3 electrochromic absorption on crystallinity. *Journal of the Electrochemical Society*, *124*(5), 749-753.

[5] Mamak, M., Choi, S. Y., Stadler, U., Dolbec, R., Boulos, M., & Petrov, S. (2010). Thermal plasma synthesis of tungsten bronze nanoparticles for near infra-red absorption applications. *Journal of Materials Chemistry*, *20*(44), 9855-9857.

[6] Young Kim, J., Yoon, H. J., yong Jeong, S., Lee, S., jic Shin, G., & Choi, K. H. Effect of CsxWO3 Nanoparticles Content and Atomic Ratio for Near Infrared Cut-off Characteristics.

Chapter 7 Development and Characterization of Nano ATO/Nano Cs$_x$WO$_3$ Thermal Insulation Coating

7.1 Introduction

The energy saving of buildings and cars is a very important part of energy conservation. In recent years, transparent insulation coating has been a new and high technology method to realize energy saving and consumption reduction because of its low production cost and simple technological process, which has attracted more and more attention [1].

Transparent insulation coating, is made up of nano inorganic transparent conductive oxide TCO (Transparent Conductive Oxide) and organic polymer resin film-former composition, which has a high visible light transmittance (50% ~ 90%) [2]. Plus, a very high shielding effect on the near-infrared light and ultraviolet light. Preparation of transparent insulation coating process is relatively simple, which disperses nano conductive oxides into the dispersion medium by physical and chemical methods to prepare stable dispersion, then mix with resin matrix film-former according to certain proportion, adding trace amounts of dispersing agent, defoamer, tackifier coating additives, and stir it well to get the final coating [3]. The produced coating can be coated on the glass surface by spraying, spraying, brushing, etc., with natural air drying or hot solidification, uv curing, etc., to form heat insulation coated glass.

In Chapter 5 and Chapter 6, the inorganic functional nanomaterials of the

transparent insulating coating of the nano-oxide antimony (ATO) and cesium tungsten bronze (Cs_xWO_3) were synthesized respectively. Both have high visible light transmittance, high absorption near infrared region. However, through observing the experimental UV-Vis-NIR transmission curve characterization results, ATO, absorption effect of ATO is not ideal in near-infrared wavelength of 780 nm to 780 nm region. At the same time, the transmission curve of Cs_xWO_3 began to increase at the wavelength of >1300 nm, while the infrared absorption capacity decreased.

In order to improve the near-infrared absorption ability of the transparent insulating coating and to strengthen the shielding of solar thermal radiation, this paper combined ATO and Cs_xWO_3 to prepare a two-component transparent insulating coating with a wide band. The ATO and Cs_xWO_3 nanoparticles were prepared and dispersed respectively by controllable solvent thermal method. With coating additives such as flow ping agent, antifoaming agent, and thickening agent, and film forming resin of waterborne polyurethane (WPU), a transparent insulating coating through a series of process condition was obtained, which exhibits an excellent heat insulating performance and high transmittance in the visible area, high absorption near infrared area. The mechanical properties and optical properties of coatings were characterized and studied in detail.

7.2 Experiment

7.2.1 Development of the thermal insulation coating based on ATO/Cs$_x$WO$_3$

7.2.1.1 Coating process

The ATO nanoparticles and Cs$_x$WO$_3$ nanoparticles were synthesized by controllable hydrothermal reaction which were reported in Chapter 5 and Chapter 6. The thermal insulation coating based on ATO/Cs$_x$WO$_3$ was fabricated by co-blending method. The aqueous dispersion of ATO and Cs$_x$WO$_3$ were added into the mixture of film-forming resin and other coating additive. After high speed mechanical agitation, the thermal insulation coating based on ATO/Cs$_x$WO$_3$ was obtained. Through the preliminary experiment, the formula of thermal insulation coating was shown in table 7.1.

Table 7.1 The formula of thermal insulation coating based on ATO/Cs$_x$WO$_3$

Component	Mass fraction (wt%)
Water based film-forming resin	55
ATO/Cs$_x$WO$_3$	20
Coating additive	5
pH adjusting agent/H$_2$O	20

Firstly, the waster-based film-forming resin was added with ATO and Cs$_x$WO$_3$ aqueous dispersion and stirred in the speed of 600rpm for 2 hours. Then, the flatting

agent, thickening agent, and other additive agents were added in the mixture solution and stirred in the speed of 1500rpm for 30 minutes. Finally, the antifoaming agent was added in the mixture solution and stirred in the speed of 800rpm for 1 hour. After 10 minutes standing, the final thermal insulation coating based on ATO and Cs_xWO_3 was fabricated. The details of the preparation flow chart of the thermal insulation coating was shown in figure 7.1
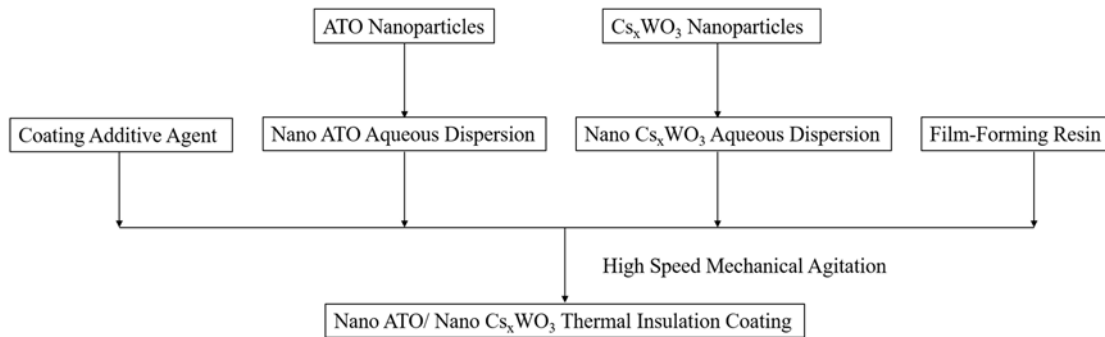
Figure 7.1 The details of the preparation flow chart about the thermal insulation coating based on ATO/ Cs_xWO_3

7.2.1.2 Film process

The glass slides or the float glasses were put on the surface of the platform in the automatic spraying equipment. The coating was sprayed in the surface of substrate with 0.2MPa by using a turbo molecular pump. The velocity of the spraying gun was 10cm/s in x-direction, and the length of the repetition space about the glass slides or the float glasses in y-direction was 2cm. The diagrammatic film process is shown in figure 7.2. The characterization of the film would be compared with the Low-E glass and tinted glass with same thickness.
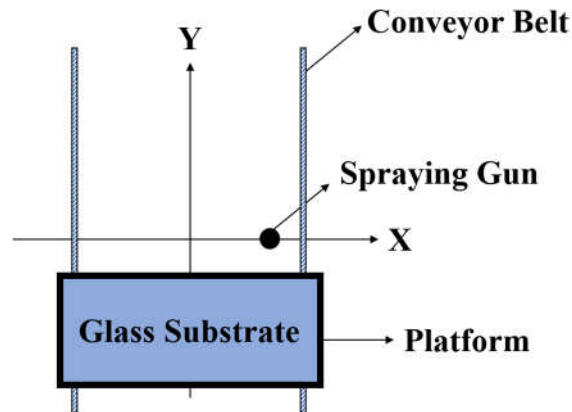
Figure 7.2The diagrammatic film process

7.2.2 Characterization of the thermal insulation coating based on ATO/Cs$_x$WO$_3$

7.2.2.1 Pencil hardness

The hardness of the coating was measured by the electric film coating pencil thickness meter. Details of the measurement process were shown in below:

1. The pencil was sharpened and fixed in the one side of the horizontal bracket on the equipment;

2. The glass substrate with the coating would be placed on the surface of the horizontal platform, and a weight was fixed in another side of the horizontal bracket on the equipment.

3. The pencil across the sample with 45°, and repeat 5 times. If there was no obvious mark on the coating surface, the hardness of the pencil was the pencil hardness of the film.

Figure 7.3Electric Film Coating Pencil Thickness Meter

7.2.2.2 Adhesion Test

The adhesion test of the coating on the glass substrate was according to the standard of ASTM D3359 (Scotch tape method of coating adhesion testing). Plus, the evaluation standard of the coating adhesion is shown below:

Table 7.2The Evaluation Standard of the Coating Adhesion

Grade	Evaluation Standard
0	Removal beyond the area of the X with tape
1	Removal from most of the area of the X with tape
2	Jagged removal along most of incisions up to 3.2mm on either side under the tape
3	Jagged removal along most of incisions up to 1.6mm on either side under the tape
4	Trace peeling or removal along incisions or at their intersection
5	No peeling or removal

7.2.2.3 Water resisting property

The water resisting test of the coating on the glass substrate was according to the standard of the GB/T 1733-1993 (the determination of the waster resisting about water-based coating). Details of the standard method are shown in below:

1. The glass substrate with coating was put into the glass container with water and 60% of the coating area was into the water.

2. After standing for 72 hours, the sample was taken out and dried with filter paper.

3. The results were evaluated according to the standard.

7.2.2.4 Thickness of the coating

The thickness of the coating would be measured by the stylus profiler of Alpha Step D-500 (KLA-Tencor).

7.3 Results and Discussion

7.3.1 Physical properties of the thermal insulation coating based on ATO/CsxWO3

7.3.1.1 The effect of different film-forming resin on the physical properties of the thermal insulation coating

In this section, the effect of different film-forming resins, acrylic latex, styrene-acrylic emulsion, fluorocarbon emulsion, and waterborne polyurethane, on the physical properties of the thermal insulation coating were investigated. The fabrication of the thermal insulation coating is shown in the 7.2.1. The mass content of the ATO and

Cs_xWO_3 was 20wt%, and the mass ratio of the ATO and Cs_xWO_3 was 1:1.

Table 7.3 shows the stability of the thermal insulation coating with different film-forming resin. It could be found that poor physical compatibility was between the fluorocarbon emulsion and ATO/ Cs_xWO_3 nanoparticles, which means that this film-forming resin cannot applied in the thermal insulation coating. The thermal insulation coating shows a certain physical compatibility with acrylic latex and styrene-acrylic emulsion, but the coating was placed stratified after a few days later, which means that the ATO/ Cs_xWO_3 nanoparticles were agglomerated with the macromolecular chain of these film-forming resin. The thermal insulation coating shows an excellent physical compatibility and high stability with the waterborne polyurethane, which means that this film-forming resin shows a great potential to apply in thermal insulation coating.

Table 7.3 The stability of the thermal insulation coating with different film-forming resin

Film-forming resin	Mixture condition	Stability (7 days)
Styrene-acrylic emulsion	Uniform without Stratified	Stratified
Acrylic latex	Uniform without Stratified	Stratified
Fluorocarbon emulsion	nonuniform	Stratified
Waterborne polyurethane	Uniform without Stratified	Uniform

Due to the poor physical compatibility of the thermal insulation coating with fluorocarbon emulsion, this film-forming resin would not be considered in the later

experiment. Table 5.4 shows the mechanical properties of the thermal insulation coating with different film-forming resin. It could be found that the hardness of the three samples was almost the same, which was higher than 4H. However, the thermal insulation coating with waterborne polyurethane shows a high hardness of 5H and high adhesion of 1 grade which was better than the adhesion of 2 grade for thermal insulation coating with styrene-acrylic emulsion and acrylic latex. In the water resisting property, there was no color fading and dropping of the thermal insulation coatings. However, some bubble and wrinkle were in the layer with styrene-acrylic emulsion and acrylic latex after water resisting test. To sum up, waterborne polyurethane is applied in the thermal insulation coating in this research.

Table 7.4 The mechanical properties of the thermal insulation coating with different film-forming resin

Film-forming resin	Hardness	Adhesion	Water resisting
Acrylic latex	4H	2	Some bubbles
Styrene-acrylic emulsion	4H	2	Some Wrinkle
Waterborne polyurethane	5H	1	Surface smoothness without color fading

7.3.1.2 The basic properties of thermal insulation coating with waterborne polyurethane

Table 7.5 shows the basic properties of the transparent thermal insulation coating with waterborne polyurethane. The fabrication process was shown in 7.2.1. The mass content of ATO and Cs_xWO_3 nanoparticles was 20wt%, and the mass ration between the ATO and Cs_xWO_3 nanoparticles was 1:1.

Table 7.5 The basic properties of the transparent thermal insulation coating with waterborne polyurethane

Basic properties	Results	Standard
Color and appearance	Cambridge blue and surface smoothness	GB 1729-79
Hardness	5H	GB/T 6739-1996
Adhesion	1Grade	ASTM D3359
Water resisting	Surface smoothness no color fading	GB/T 1733-1993
Alcohol resisting	No bubble, wrinkle and color fading	JGT 338-2011
Thermal resisting	No bubble, wrinkle, color fading and crack	GB 1735-79
Drying time of the film	80°C×3h	GB/T1728-1979
Flexibility	2mm	GB/T 1731-93

Temperature Reducing	9.2℃	Self-made hot box testing

According to the above investigation, the transparent thermal insulation coating based on ATO/Cs$_x$WO$_3$ with waterborne polyurethane shows an excellent physical property which can be applied in the window glass.

7.3.2 Optical Property of the thermal insulation coating based on ATO/Cs$_x$WO$_3$

7.3.2.1 Optical property of the thermal insulation coating with different mass ration of ATO/Cs$_x$WO$_3$

Both ATO and Cs$_x$WO$_3$ exhibited a high visible light transmittance and high NIR light blocking rate. However, they show a different absorption in different NIR light range. Hence, to obtain a transparent thermal insulation coating with optimum NIR blocking rate and visible light transmittance, the mass ration between ATO and Cs$_x$WO$_3$ nanoparticles in the coating is very important.

In this section, the mass content of the nanoparticles was 20wt%, and the mass ration between ATO and Cs$_x$WO$_3$ was 7:3, 5:5, and 3:7, respectively. Besides, the transparent thermal insulation coatings with 20wt% ATO nanoparticles and 20wt% Cs$_x$WO$_3$ nanoparticles would also be fabricated, respectively. The fabrication process was shown in 5.2.1, and the UV-Vis-NIR spectrophotometer was employed in the wavelength range from 300-2500nm for transmittance measurement of the different transparent thermal insulation coating as shown in figure 7.4.
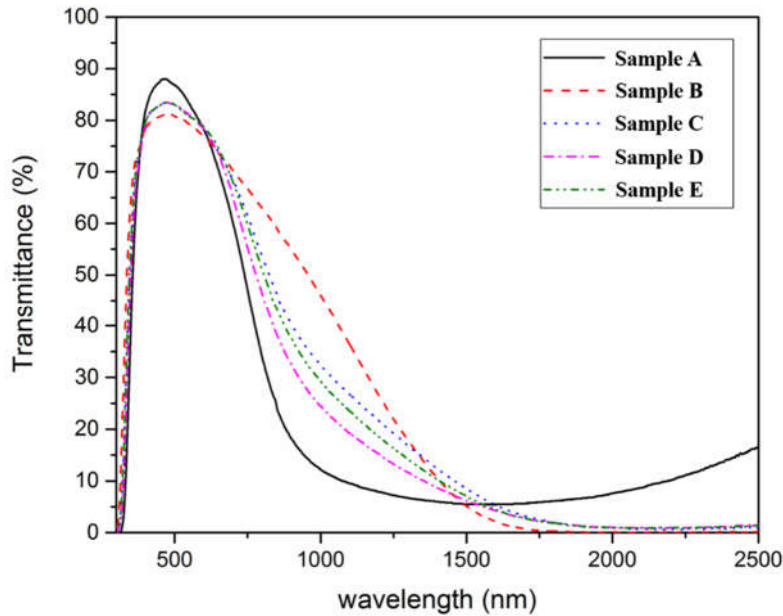
Figure 7.4 The transmittance of the thermal insulation coating with different mass ration between ATO and Cs_xWO_3 nanoparticles

(A: Cs_xWO_3; B: ATO; C: 7:3; D: 5:5; E: 3:7)

It could be found that all the samples show a high visible light transmittance in wavelength of 380-780nm and high NIR light blocking rate in the wavelength range of 780-2500nm. The blocking rate of the thermal insulation coating with Cs_xWO_3 was obviously higher than the thermal insulation coating with ATO in the range of 780-1500nm. However, the transmittance of the thermal insulation coating with Cs_xWO_3 was obviously higher than the thermal insulation coating with ATO in the range of 1500-2500nm. Combined with ATO and Cs_xWO_3, the thermal insulation coatings exhibited a higher NIR blocking rate in wavelength range of 780-2500nm. After calculation, when the mass ration between ATO and Cs_xWO_3 was 1:1, the thermal

insulation shows a highest NIR blocking rate. Table 7.6 shows the integral computation of the optical properties in different wavelength range. It could be found the transmittance of the visible light was 74.3%, and the NIR light transmittance was 9.6%, which was the optimum formula as a thermal insulation coating.

Table 7.6 The integral computation of the transmittance about the different mass ration for the coating in UV light range, visible light range and NIR light range

Sample	UV light (%)	Visible light (%)	NIR light (%)
A	28.6	73.8	10.1
B	45.3	75.6	14.2
C	38.0	75.7	12.3
D	34.5	74.3	9.6
E	38.1	75.6	11.1

7.3.2.2 Optical property of the thermal insulation coating with different thickness

In this section, the effect of the thickness on the optical property of the thermal insulation coating would be investigated. The coating would be filmed on the glass substrate through the automatic spraying equipment. Plus, the thickness of the coating would be adjusted by changing the conditions of film process. Meanwhile, the thickness of the thermal insulation coating would be measured by the stylus profiler. The mass content of the ATO/Cs_xWO_3 nanoparticles was 20wt%, and the mass ratio between the ATO and Cs_xWO_3 was 1:1.

Figure 7.5 shows the transmittance of the thermal insulation coating in different thickness. It could be found that the transmittance of the visible light and NIR light were decreased with the thickness of the thermal insulation coating be enhanced. Table 7.7 shows the integral computation of the transmittance in UV light range, visible light range and NIR light range. It could be found that a rapid decrease was in the visible light transmittance, when the thickness was higher than 6.59μm. Hence, the optimum thickness of the thermal insulation coating was 6.59μm.
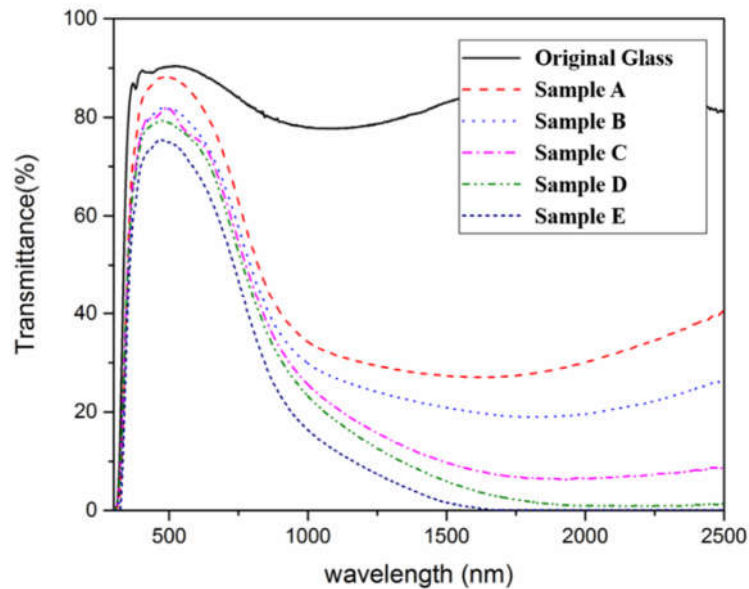
Figure 7.5 The transmittance of the thermal insulation coating in different thickness
(A: 3.17μm; B: 4.29μm; C: 5.68μm; D: 6.59μm; E: 7.64μm)

Table 7.7 The integral computation of the transmittance about the different coating thickness in UV light range, visible light range and NIR light range

Sample	UV light (%)	Visible light (%)	NIR light (%)
A	49.4	88.1	81.9
B	34.5	79.9	32.3

C	34.2	73.8	24.2
D	33.5	72.4	13.5
E	32.8	70.6	9.1

7.3.2.3 Optical property comparison between thermal insulation coating, Low-E glass, and tinted glass

To compare with other thermal insulation glass, Low-E glass and tinted glass would be purchased for this experiment. The size of the Low-E glass and tinted glass was 0.3m×0.3m×0.005m. The transparent thermal insulation coating was fabricated according to the 7.2.1. The mass content of the ATO/Cs$_x$WO$_3$ nanoparticles was 20wt%, and the mass ration between ATO and Cs$_x$WO$_3$ was 1:1. Besides, the thickness of the thermal insulation coating was adjusted in 6.59μm through automatic spraying equipment.

Figure 7.6 shows the transmittance of the glass with thermal insulation coating, Low-E glass, tinted glass and original glass. Table 7.8 shows the integral computation of the transmittance about the glass with thermal insulation coating, Low-E glass, tinted glass and original glass in UV light range, visible light range and NIR light range.
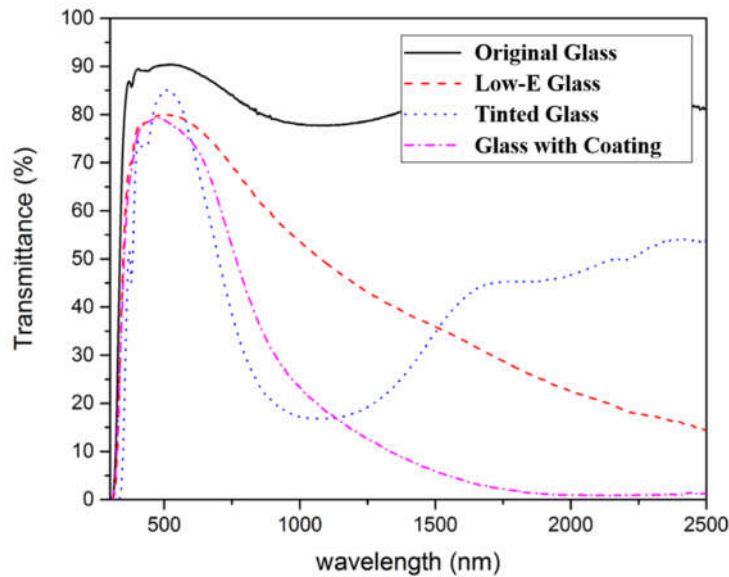
Figure 7.6 The transmittance of the glass with thermal insulation coating, Low-E glass, tinted glass and original glass

It could be found that the original glass only shows a small UV light blocking rate, while original glass shows a high transmittance in both visible light and NIR light range. Compared with the Low-E glass and tinted glass, the glass with thermal insulation coating exhibited a higher NIR blocking rate of 90.9%. Meanwhile, the glass with thermal insulation coating also shows a high visible light transmittance of 70.6%. It means that the thermal insulation coating based on ATO and Cs_xWO_3 shows a great potential in reducing the energy consumption in building area.

Table 7.8 Integral computation of the transmittance about the glass with thermal insulation coating, Low-E glass, tinted glass and original glass in UV light range, visible light range and NIR light range

Sample	UV light (%)	Visible light (%)	NIR light (%)
Glass with coating	32.8	70.6	9.1

Low-E glass	33.9	76.2	34.1
Tinted Glass	15.9	66.8	36.7
Original Glass	49.4	88.1	81.9

7.4 Conclusion

In this chapter, a novel thermal insulation coating based on ATO and Cs_xWO_3 has been fabricated. This coating was constituted with nanoparticles aqueous solution, film-forming resin, and some additive agents, which exhibited a high NIR light blocking rate and excellent visible light transmittance. The physical properties and optical properties of the thermal insulation coating were investigated in this chapter. Details are shown as below:

1. The waterborne polyurethane was the optimum film-forming resin applied in the thermal insulation coating. In addition, the coating with this resin exhibited a high hardness of 3H, high adhesion of 1 grade. Meanwhile, the coating combined with resin shows a high water resisting.

2. The effect of the mass ration between ATO and Cs_xWO_3 on the optical property of thermal insulation coating has been firstly investigated. The result shows that the optimum mass ration of the thermal insulation coating between ATO and CsxWO3 was 1:1, and the coating exhibited a high NIR light blocking rate of 90.4%, and an excellent visible light transmittance of 74.3%.

3. The effect of the coating thickness on the optical property of thermal insulation

coating has been firstly investigated. The result shows that the optimum thickness of the thermal insulation coating was 6.59μm, and the coating exhibited a low NIR light transmittance of 9.6%.

4. This chapter also firstly investigated the optical property comparison between the glass with thermal insulation coating, Low-E glass, tinted glass and original glass. The results show that the glass with thermal insulation coating exhibited a high visible light transmittance of more than 70%, and the NIR blocking rate was higher than Low-E glass of 34.1% and tinted glass of 36.7%, which was more than 90%. It means that the thermal insulation coating based on ATO and Cs_xWO_3 shows a great potential in reducing energy consumption of buildings.

7.5 Reference

[1] Guo, C., Yin, S., Zhang, P., Yan, M., Adachi, K., Chonan, T., & Sato, T. (2010). Novel synthesis of homogenous Cs x WO 3 nanorods with excellent NIR shielding properties by a water controlled-release solvothermal process. *Journal of Materials Chemistry, 20*(38), 8227-8229.

[2] Liu, J. X., Ando, Y., Dong, X. L., Shi, F., Yin, S., Adachi, K., ... & Sato, T. (2010). Microstructure and electrical–optical properties of cesium tungsten oxides synthesized by solvothermal reaction followed by ammonia annealing. *Journal of Solid State Chemistry, 183*(10), 2456-2460.

[3] Mamak, M., Choi, S. Y., Stadler, U., Dolbec, R., Boulos, M., & Petrov, S. (2010). Thermal plasma synthesis of tungsten bronze nanoparticles for near infra-red absorption applications. *Journal of Materials Chemistry*, *20*(44), 9855-9857.

[4] Chen, C. J., & Chen, D. H. (2013). Preparation and near-infrared photothermal conversion property of cesium tungsten oxide nanoparticles. *Nanoscale research letters*, *8*(1), 57.

[5] Guo, C., Yin, S., Yan, M., Kobayashi, M., Kakihana, M., & Sato, T. (2012). Morphology-controlled synthesis of W18O49 nanostructures and their near-infrared absorption properties. *Inorganic chemistry*, *51*(8), 4763-4771.

[6] Bamwenda, G. R., Sayama, K., & Arakawa, H. (1999). The effect of selected reaction parameters on the photoproduction of oxygen and hydrogen from a WO3–Fe2+–Fe3+ aqueous suspension. *Journal of Photochemistry and Photobiology A: Chemistry*, *122*(3), 175-183.

Chapter 8 Development and Investigation of Black-TiO$_2$ Film

8.1 Introduction

TiO$_2$ is a kind of widely used oxide semiconductor materials. Due to its environmentally friendly, chemical stability, low cost and good electric transfer performance, TiO$_2$ has been widely applied in energy and environmental area [1-3]. Since an excellent photocatalysis property of anatase TiO$_2$ has been found in 1972, TiO$_2$ has been prepared and studied intensively in recent decades, especially as electro-chromic devices in energy and environment governance. However, the bandgap of the anatase TiO$_2$ is 3.2eV, and the ability of electron hole pairs separation and transfer is low, which limit the application of pure anatase TiO$_2$.

Hence, the morphological control and crystal face control were used to enhance the property of TiO$_2$. Elements doping was considered as an effective method to change the photocatalysis property, light absorption and local surface plasma frequency. Until now, the element doping of TiO$_2$ contains metallic element doping, nanometallic element doping and metallic/nonmetallic elements co-doping.

The metallic element doping of TiO$_2$ is a very impartment method to change the property of anatase TiO$_2$, due to its simple process, short reaction time and low cost. There are two positive effect on photocatalysis property of TiO$_2$ when the metallic elements doping into the TiO$_2$ crystal lattice. The first is that the defect in the doping

crystal lattice could become low potential capture trap, which can enhance the hole-electron pair separation. The second is that the effect on the separated hole-electron pair due to the light absorption can reduce the potential of recombination of the hole-electron pair. It means that these can enhance the photocatalysis property of the TiO_2. However, the metallic elements doping may cause the negative effect on the photocatalysis of TiO_2, because the hole-electron pair may recombine and center on the metallic elements. According to the previous research, even though the TiO_2 was doped with same metallic element, the effect on the photocatalysis would be different by changing the conditions of methods.

Since Asahi has investigated that nanometallic element doping can enhance the light absorption in theory, and he found that TiO_2 doped with N exhibited a positive photocatalysis property in 2001, numerous studies are focus on the nonmetallic elements doping of TiO_2, and a series of significant progress has been made. However, some limitations were found in the nonmetallic element doping of TiO_2, such as the poor heat stability, and nonmetallic element would easy be the center of hole-electron pair recombined. Plus, the major problem is that the principle of nonmetallic element improving the photocatalysis of TiO_2 would remain controversial. Some researchers consent that nonmetallic element would reduce the bandgap of TiO_2 by combining with P orbital of Ti, which tend the light absorption of TiO_2 to visible light range, and make photocarriers to enhance the redox reaction.

In 2011, Xiaobo Chen firstly obtain the Black-TiO_2 through hydrogen reduction,

and he presented his results in Science. This Black-TiO$_2$ has special structure of lattice imperfection, ameliorative electron structure and enhancement of surface activity, which exhibited an excellent light absorption and electrochemistry property [4-5].

However, the cost of the method is very high and cannot be manufactured. This chapter synthesized the Black-TiO$_2$ with a simple method and investigated the optical property and photocatalysis property of the Black-TiO$_2$ film.

8.2 Experiment

8.2.1 Synthesis of self-dispersion TiO$_2$

Self-dispersion nano TiO$_2$ was synthesized by controllable hydrothermal reaction, and the details of the technical process are as follows (Figure 8.1):

1) The precursor of titanium tetrachloride of (TiCl$_4$) and hydrochloric acid were weighed by analytical balance and measuring cylinder, respectively, and then added in absolute ethyl alcohol with as mixture solution A. The mass fraction of TiCl4 in absolute ethyl alcohol was 10wt%.

2) PPL liner was successively cleaned with hydrochloric acid, deionized water and absolute ethyl alcohol.

3) The mixture solution A was added in PPL liner and the PPL with the reactant was sealed in stainless steel case. Then, the hydrothermal reactor was placed in drying oven at 180°C.

4) After finishing reaction, the ionic impurity in the product should be removed by centrifuge and absolute ethyl alcohol. Than the solid in the bottom of the

centrifuge tube would be transferred into drying oven at 80°C. After drying, the white self-dispersion TiO_2 nanoparticles, as shown in figure 6.2, would be obtained.
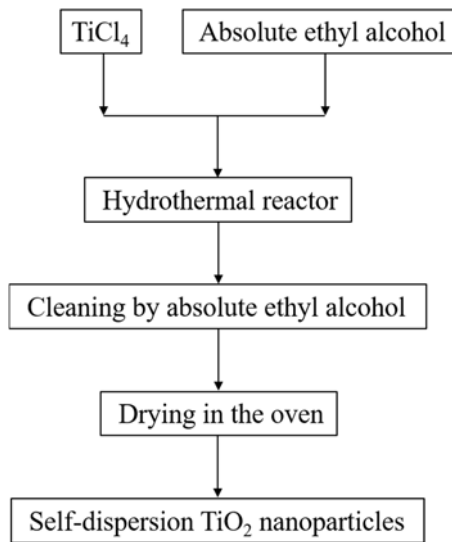
Figure.1 Synthesis of self-dispersion TiO_2 nanoparticles
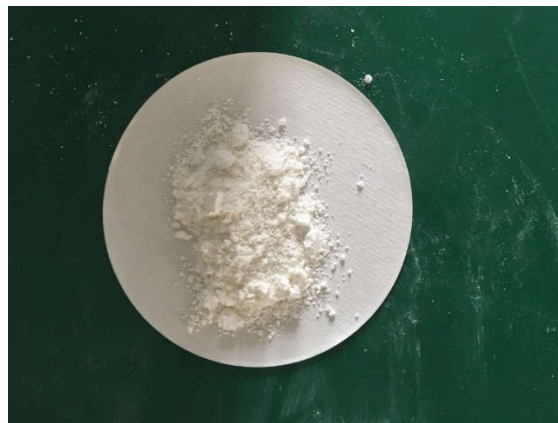
Figure 8.2 White self-dispersion TiO_2 nanoparticles

8.2.2 Preparation of Black-TiO₂ film

The white self-dispersion TiO_2 nanoparticles, which were measured by analytical balance, were added in deionized water, and the mass fraction of the TiO_2 nanoparticles

in deionized water was 5wt%. A well dispersion aqueous colloid solution was obtained. The aqueous colloid solution was put into the storage silo in the automatic spraying equipment. The glass substrate was placed on the platform and the coating was sprayed in the surface with 0.2MPa by using a turbo molecular pump. The velocity of the spraying gun was 10cm/s in x-direction, and the length of the repetition space about the glass slides or the float glasses in y-direction was 2cm. Finally, the film coated glass was placed in electric reduction equipment. After adjusting the conditions of electrochemistry reduction, the final black-TiO_2 film would be obtained. The diagrammatic film process is shown in figure 8.3.
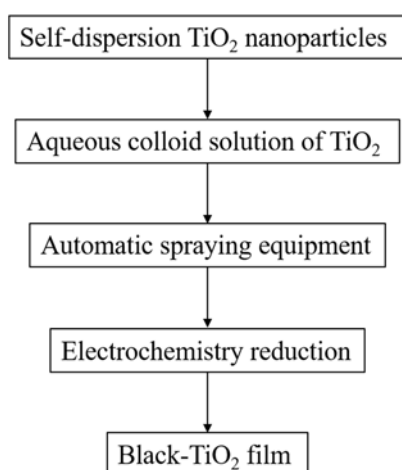
Figure 8.3 The diagrammatic Black TiO_2 film process

8.3 Results and Discussion

8.3.1 Characterization of the white self-dispersion TiO₂ nanoparticles

Self-dispersion TiO_2 nanoparticles were fabricated through controllable thermal insulation coating which is conducted as 8.2.1. The crystal structure of the nanoparticles

was recorded by XRD and are shown in Figure 6.4. It could be found that the peak positions of sample are well agree with the reflections of anatase TiO_2, and no other impurities peaks in samples can be recorded, which indicates that the TiO_2 with anatase crystal form was obtained.
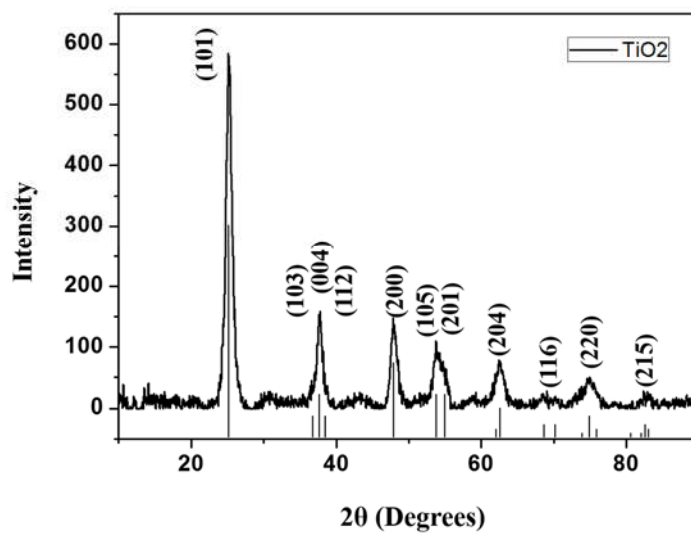
Figure 8.4 The XRD pattern of the TiO_2

The morphology of self-dispersion TiO_2 nanoparticles were observed by TEM and are shown in figure 8.5A. The particle size of TiO_2 is homogeneous and the size distribution is around 5nm. The SAED pattern taken form a part of the self-dispersion TiO_2 nanoparticles in figure 6.5a are shown in figure 8.5b, which could be found that the nanoparticles possess interplanar spacings of 3.5213, 2.4320, 2.3787, 2.3322, 1.8926, and 1.7000 Å corresponding to the (101), (103), (004), (112), (200), and (105) planes, respectively. Figure 8.5c shows the HRTEM image of the self-dispersion TiO_2 nanoparticles. In this image, the lattice plane of TiO_2 nanoparticles was (101) with a lattice of 3.5Å.
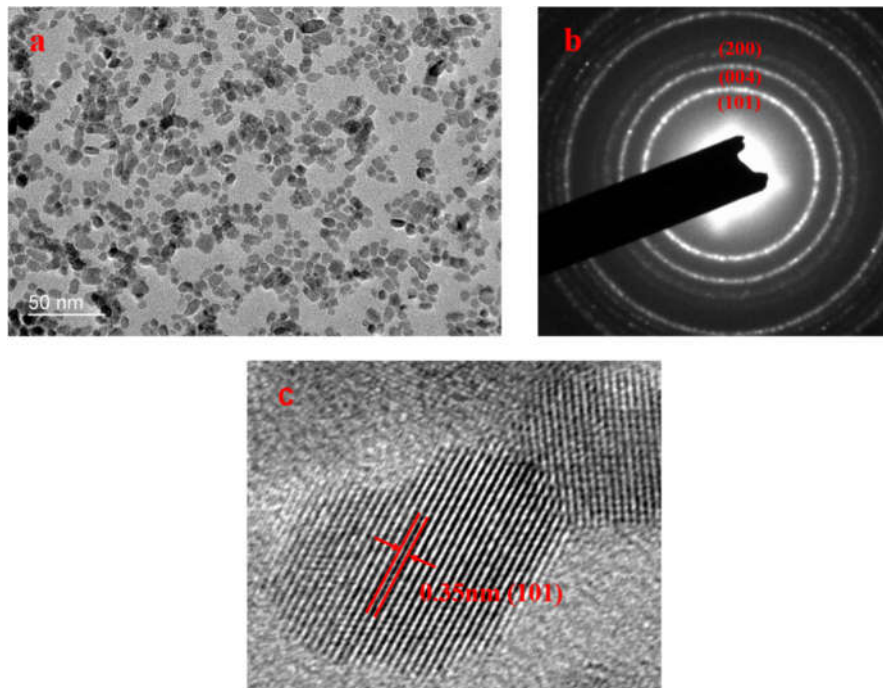
Figure 8.5 The TEM image of the TiO$_2$ (a), SAED pattern of the TiO$_2$ (b) and the HRTEM image of the TiO$_2$ (c)

Figure 8.6A shows the TiO$_2$ nanoparticles was self-dispersing in the deionized water. It could be found that a transparent colloid with baby blue could be obtained. Plus, after standing for 7days, there was still no precipitate in the bottom of glass container. The secondary particle size distribution of the TiO$_2$ colloid is shown in figure 8.6B. The narrow size distribution was from 12nm to 30nm, and average of the secondary particle size is only 19nm, which further confirmed a high dispersion of TiO$_2$.
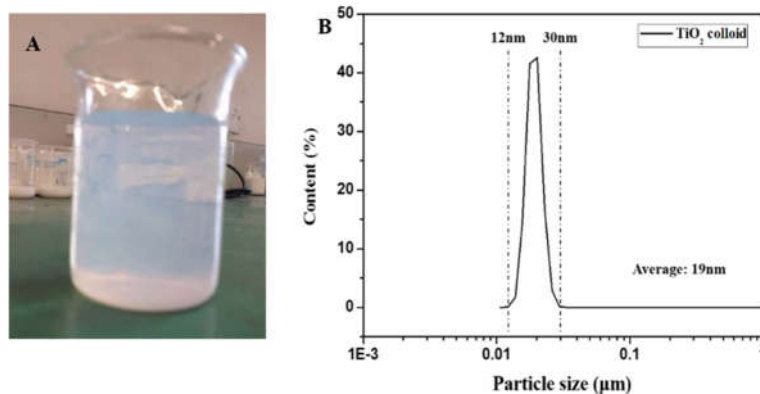
Figure 8.6 The TiO₂ nanoparticles self-dispersing in deionized water (A) and laser particle size distribution of TiO₂ colloid

8.3.2 The effect of hydrochloric acid concentration on the property of the white self-dispersion TiO₂ nanoparticles

This section investigated the effect of hydrochloric acid concentration on the property of the TiO_2 nanoparticles which were fabricated through controllable hydrothermal reaction as conducted in 8.2.1. The pH of the reactant was maintained in 6.46, 6.08, 5.62, 5.08, 4.28, and 3.60, which were measured by pH meter. The reaction time and reaction temperature were kept at 8 hours and 180°C, respectively, and the mass fraction of $TiCl_4$ in absolute ethyl alcohol was 10wt%.

Figure 8.7 shows the XRD spectrum of the samples with different pH, and the XRD pattern of Am show the clear spectral characteristics for TiO_2 which confirmed the identity of TiO_2. By calculating the peak intensity from the XRD data, it clearly shows that the peak intensity of [101] direction increases with the decrease of pH value. The reason was that H^+ would promote the dissolution of the reacted precursor, which exhibited a positive effect on the crystal growth. However, the intensity of the peak in A1 shows a small difference between the intensity of the peak in A2, which means that

the effect of the pH value in sample of A2 was tend to the equilibrium. The peak intensity of [101] is always as a measure of the degree of crystallinity for TiO$_2$. Thus, with the decreasing pH, the crystallinity of TiO$_2$ increased, which means the photocatalyst property will be improved.
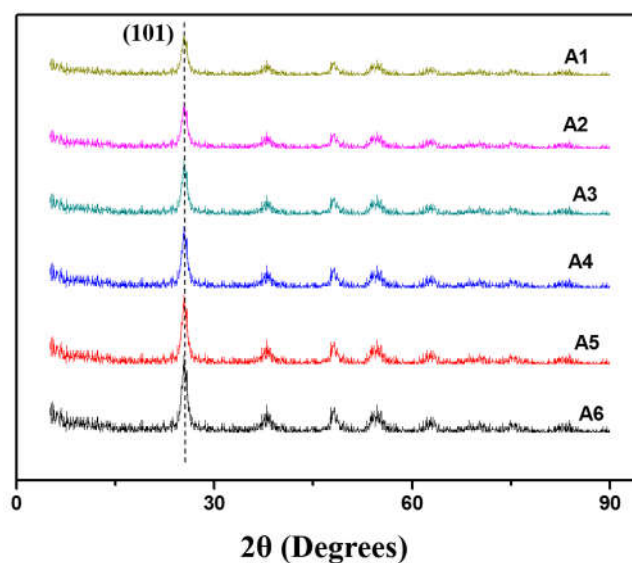
Figure 8.7 The XRD spectrum of the samples with different pH value

A1: 6.46; A2: 6.08; A3: 5.62; A4: 5.08; A5: 4.28; A6: 3.60

Figure 8.8 shows the optical property of TiO$_2$ coating on glass substrate which was processed by the automatic spraying equipment. In the process method, the mass concentration of TiO$_2$ in deionized water was 5wt%. The velocity of the spraying gun was kept in 10cm/s in x-direction, and the length of the repetition space about the glass slides or the float glasses in y-direction was kept in 2cm.
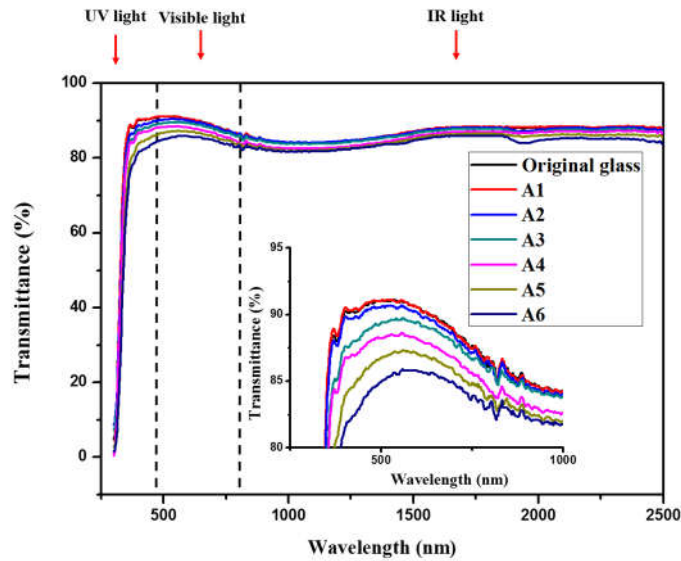
Figure 8.8 The Transmittance of TiO$_2$ coating on glass substrate

A1: 6.46; A2: 6.08; A3: 5.62; A4: 5.08; A5: 4.28; A6: 3.60

It could be found that due to the band gap of TiO$_2$ is around 3.2eV, all the samples had a light absorption in UV region, which can induce the generation of hydroxyl radical (-OH) and superoxide anion (O^{3-}) to break down organic dirt and obtain a super-hydrophilic surface. But a lower absorption in visible light region as shown in figure 8.8 may be a negative effect on coating application. This may be caused by the reason that the H$^+$ promote the small grain dissolved and then recrystallized to large-crystal which lead a reduction of visible light transmittance.

Table 8.1 Transmittance reduction of different samples

A1: 6.46; A2: 6.08; A3: 5.62; A4: 5.08; A5: 4.28; A6: 3.60

Sample	UV-light	Visible light	IR light

A1	0.8%	0.1%	0%
A2	1.3%	0.2%	0%
A3	4.3%	0.9%	0.2%
A4	6.7%	1.2%	0.5%
A5	12.4%	2.5%	3.8%
A6	15.1%	3.3%	6.8%

The transmittance reduction value of the samples in different pH value was shown in table 8.1. It could be found that in the transmittance reduction from A3 to A6, the visible light and IR light transmittance were reduced with decreased pH value. Thus, the pH value of the reactants was 5.62.

To evaluate the self-cleaning properties of the samples in different pH value, a camera was used to record the static behavior of a water droplet on the surface of different samples. As shown in figure 8.9, side view images showed that WCA on the original glass was about 43.7°, and the WCA on the treated surface was lower than 10°. With the decrease of pH, the WCA of the glass with TiO_2 coating was diminution, because the degree of crystallization (crystallinity) for TiO_2 was enhanced by the addition of acid, which means the self-cleaning property was improved.
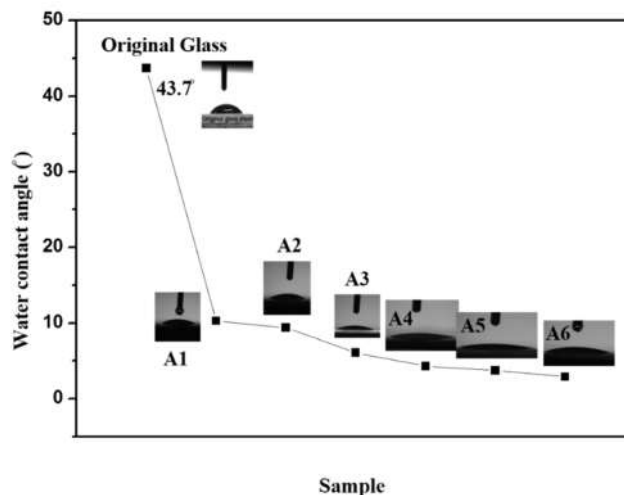
Figure 8.9 The WCA image of the sample in different pH value

A1: 6.46; A2: 6.08; A3: 5.62; A4: 5.08; A5: 4.28; A6: 3.60

Owing to the above investigation, the optimum pH value of the reactant was 5.62, which exhibited a high visible light transmittance of 99.1% and low WCA of 7.6°. Meanwhile, the UV blocking rate and NIR blocking rate were 4.3% and 0.2%, respectively.

8.3.3 The effect of the reaction conditions on the property of the black-TiO$_2$ film

8.3.3.1 The effect of the NH$_4$Cl concentration in the electrochemistry reaction on the property of the black-TiO$_2$ film

This chapter investigated the effect of the NH$_4$Cl concentrate in the electrochemistry reaction on the property of the black-TiO$_2$ film. Black-TiO$_2$ film was fabricated as conducted in 8.2.2. The glass substrate was placed on the platform and the coating was sprayed in the surface with 0.2MPa by using a turbo molecular pump. The velocity of the spraying gun was kept in 10cm/s in x-direction, and the length of the

repetition space about the glass slides or the float glasses in y-direction was kept in 2cm. The NH_4Cl mass concentration was maintained at 5wt%, 10wt%, 15wt% and 20wt%. The mass ration between deionized water and ethylene glycol was maintained at 1:1. The voltage and the electric current in the electrochemistry reaction were maintained at 5V and 2A, respectively. The reaction time was kept in 10minutes.

Figure 8.10 shows the photos of the samples in different NH_4Cl mass concentrate. It could be found that the color would be changed darker with the NH_4Cl mass concentration increased, especially in the sample A-C, which means that the degree of doping was increased. This is because that the ionic concentration would be increased with the NH_4Cl mass concentration increased, which lead to a positive effect on the electro-reduction reaction.
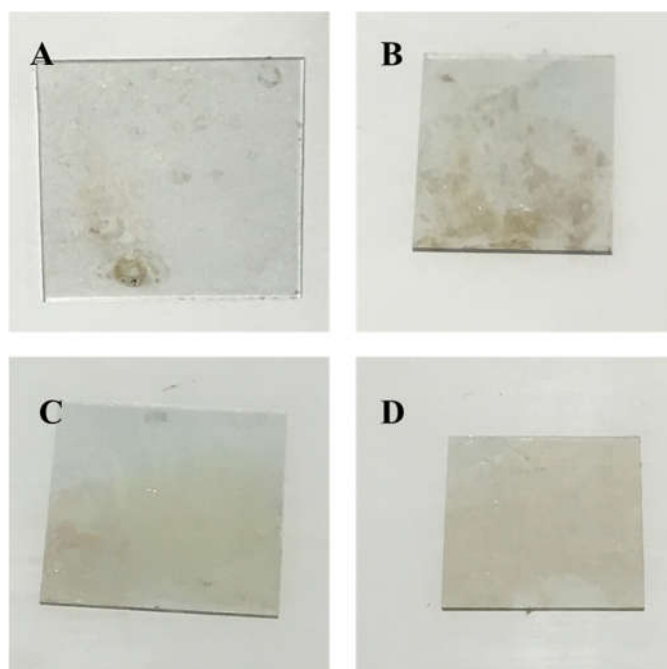
Figure 8.10 The photos of the samples in different NH_4Cl mass concentrate

A: 5wt%; B: 10wt%; C: 15wt%; D: 20wt%

Figure 8.11 shows the XRD pattern of the samples in different NH_4Cl mass concentration. It could be found that the peak positions of samples are well agree with the reflections of anatase TiO_2, and no other impurity peaks in samples can be recorded, which indicates that the black-TiO_2 with anatase crystal form was obtained. By calculating the peak intensity from the XRD data, it clearly shows that the peak intensity of [101] direction decreases with the increase of NH_4Cl mass concentration, especially in the sample A-C. The reason is that the crystallinity of the nanoparticles reduced by the lattice distortion, when the Ti^{4+} was replaced by Ti^{3+}. This behavior is consistent with the photos of the samples in different NH_4Cl mass concentration. However, the intensity of [101] almost same between sample C in 15wt% of NH_4Cl and sample D in 20wt% of NH_4Cl. This may be because NH_4Cl mass concentration tends to saturate to support the return of white TiO_2 film to black TiO_2 film.
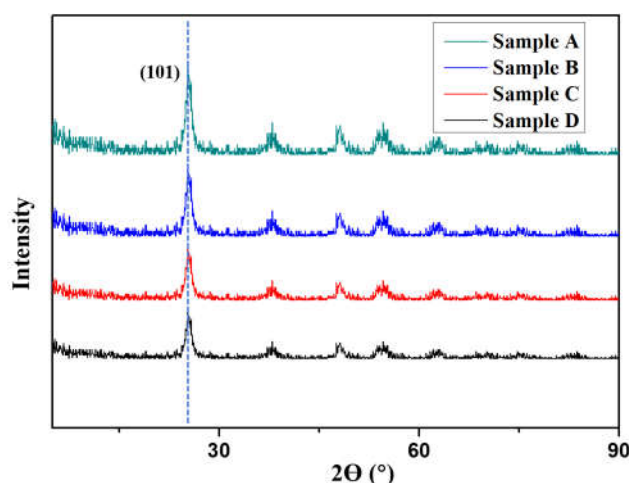
Figure 8.11 The XRD pattern of the samples in different NH_4Cl mass concentrate. (A: 5wt%; B: 10wt%; C: 15wt%; D: 20wt%)

UV-Vis-NIR transmittance can accurately represent the optical properties of the black-TiO$_2$ films. Figure 8.12 shows the UV-Vis-NIR transmittance of the samples under different NH$_4$Cl mass concentration. It could be fund that all the samples exhibited a high transmittance in the visible light range of 380~780nm, and a high blocking rate in the NIR light range of 780-2500nm, especially in the range of 1500-2500nm. With the NH$_4$Cl concentrate increased, the NIR transmittance would decrease. However, the visible light transmittance would also decrease with the NH$_4$Cl concentrate increased. This is because that the black TiO$_2$ is a core-shell structure with chaotic crystal lattice. In this structure the band gap would be changed with the abundant oxygen vacancy. Meanwhile, much trailer tape and interstitials would be processed with the band gap changed. Hence, black-TiO$_2$ exhibited two kinds of electron excitation: one is from valence band to conduction band, another is from valence band to interstitials or from interstitials to conduction band.
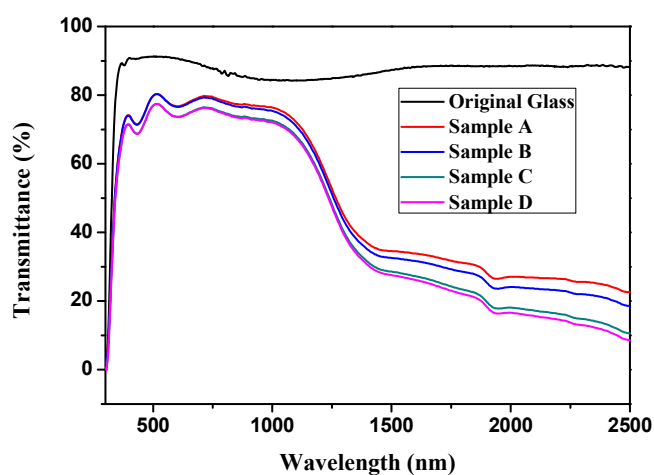
Figure 8.12 The UV-Vis-NIR transmittance of the samples in different NH$_4$Cl mass concentration. A: 5wt%; B: 10wt%; C: 15wt%; D: 20wt%

After integration of different wavelength range, the UV-Vis-NIR transmittance value are shown in Table 8.2. It could be found the NIR blocking rate tended to a limit value after NH$_4$Cl mass concentration higher than 15wt%.

Table 8.2 The UV-Vis-NIR transmittance value of the samples in different NH$_4$Cl mass concentration. A: 5wt%; B: 10wt%; C: 15wt%; D: 20wt%

Sample	UV-light	Visible light	IR light
A	36.6%	75.8%	53.4%
B	34.3%	75.2%	42.7%
C	21.4%	72.3%	38.2%
D	20.9%	72%	35.6%

Figure 8.13 shows the WCA of the samples under different NH$_4$Cl mass concentration. It could be found that the WCA would be decreased with the NH$_4$Cl mass concentration increased. Because the doped degree was increased by the enhancement of the NH$_4$Cl mass concentration, it exhibited a positive effect on the photocatalysis property of the black-TiO$_2$ film. When the NH$_4$Cl mass concentration was higher than 15wt%, the WCA tended to a limited value of 3.5°, which was consist with the results shown in the XRD pattern.
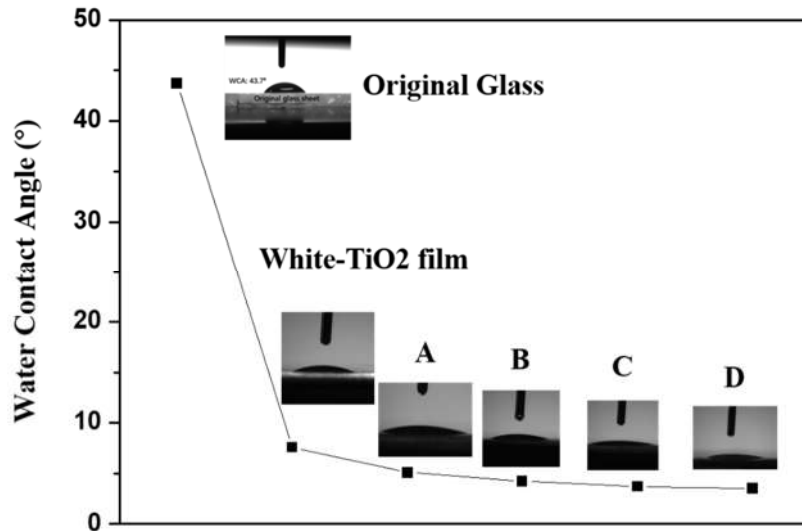
Figure 8.13 The WCA of the samples under different NH$_4$Cl mass concentration

A: 5wt%; B: 10wt%; C: 15wt%; D: 20wt%

The photocatalytic activity properties of the black-TiO$_2$ films were measured as in section 8.2.2. Every black-TiO$_2$ film had surface area of 0.36cm^2. The distance between the thin film and the fluorescent lamp (12w, 150mm long, broad emission peak range is 365nm-750nm, and the center peak is 550nm) was 10cm. Figure 8.14 shows the degradation efficiency of the MB solution degraded by the different samples in different time. Plus, the table 8.3 shows the degradation efficiency value of the MB solution degraded by the samples in different NH$_4$Cl mass concentration under different time.
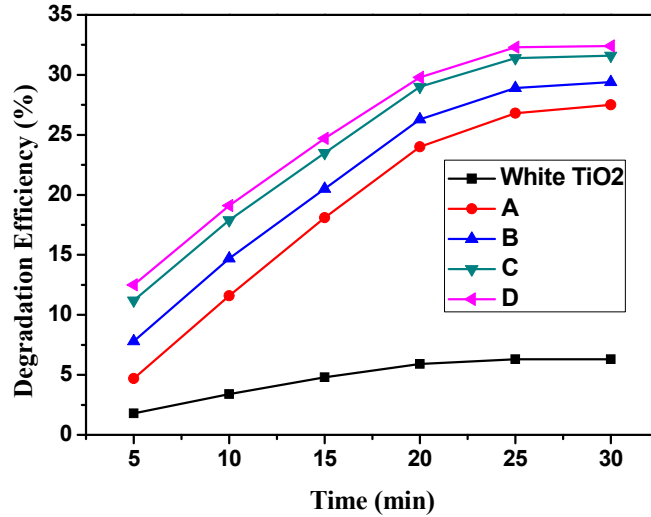
Figure 8.14 The degradation efficiency (%) of the MB solution degraded by the samples in different NH$_4$Cl mass concentration under different time

(A: 5wt%; B: 10wt%; C: 15wt%; D: 20wt%)

It could be found that with the NH$_4$Cl mass concentration increase, the degradation efficiency of the MB solution would be increased. Meanwhile, with the time increased, the degradation rate was decreased, because the concentration of the MB solution was decreased. After the NH$_4$Cl mass concentration was higher than 15wt%, the degradation efficiency was tended to a limited value, which is consist the results of the WCA as shown in figure 8.13. Hence, the optimum NH$_4$Cl mass concentration was 15wt%.

Table 8.3 The degradation efficiency (%) of the MB solution degraded by the samples in different NH$_4$Cl mass concentration under different time

(A: 5wt%; B: 10wt%; C: 15wt%; D: 20wt%)

Sample	5min	10min	15min	20min	25min	30min
White-TiO$_2$	1.8	3.4	4.8	5.9	6.3	6.3

|						
A	4.7	11.6	18.1	24.0	26.8	27.5
B	7.8	14.7	20.5	26.3	28.9	29.4
C	11.2	17.9	23.5	29.0	31.4	31.6
D	12.5	19.1	24.7	29.8	32.3	32.4

8.3.3.2 The effect of the ratio between deionized water and ethylene glycol in the electrochemistry reaction on the property of the black-TiO$_2$ film

This chapter investigated the effect of the ration between deionized water and ethylene glycol in the electrochemistry reaction on the property of the black-TiO$_2$ film. Black-TiO$_2$ film was fabricated as conducted in 8.2.2. The glass substrate was placed on the platform and the coating was sprayed on the surface with 0.2MPa by using a turbo molecular pump. The velocity of the spraying gun was kept in 10cm/s in x-direction, and the length of the repetition space about the glass slides or the float glasses in y-direction was kept in 2cm. The NH$_4$Cl mass concentration was maintained at 15wt%. The mass ration between deionized water and ethylene glycol was maintained at 2:1, 1:1, and 1:2. Meanwhile, the pure deionized water and pure ethylene glycol were as the comparison samples. The voltage and the electric current in the electrochemistry reaction were maintained in 5V and 2A, respectively. The reaction time was kept in 10minutes.

Figure 8.15 The photos of the samples in different mass ratio between deionized water and ethylene glycol (A: pure water; B: 2:1; C: 1:1; D: 1:2; E: pure ethylene glycol)

Figure 8.15 shows the photos of the samples in different mass ratio between deionized water and ethylene glycol. It could be found that the color would be changed darker with the mass ration increased, due to the high solubility of NH_4Cl in deionized water, which can increase the ionic conduction in the electrolyte solution. Hence, a positive effect was on the electrochemistry reaction. However, a nonuniform coating surface can be found in the photos, when the mass ration higher than 1:1. The reason is

that the bubble on the coating surface would be increased with the ionic conduction be improved. Thus, the mass ratio between deionized water and ethylene glycol in electrochemistry reaction is very important.

Figure 8.16 shows the XRD pattern of the samples in different mass ratio between deionized water and ethylene glycol. It could be found that the peak positions of samples are well agree with the reflections of anatase TiO_2, and no other impurity peaks in samples can be recorded, which indicates that the black-TiO_2 with anatase crystal form was obtained. By calculating the peak intensity of the XRD data, it clearly shows that the peak intensity of [101] direction decreases with the increase of mass ratio between deionized water and ethylene glycol, which is consist with the results shown in Figure 8.15.
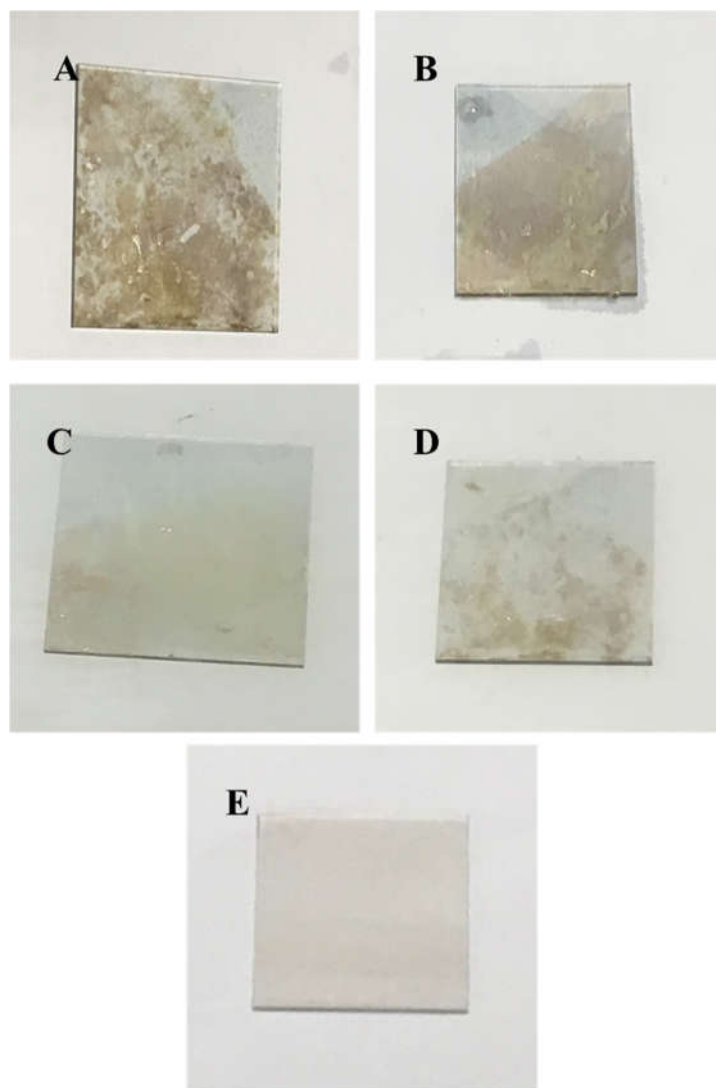

Figure 8.16 The XRD pattern of the samples in different mass ratio between deionized water and ethylene glycol

(A: pure water; B: 2:1; C: 1:1; D: 1:2; E: pure ethylene glycol)

Figure 8.17 shows the UV-Vis-NIR transmittance of the samples under different mass ratio between deionized water and ethylene glycol. It could be found that all the samples exhibited a high transmittance in the visible light range of 380~780nm, and a high blocking rate in the NIR light range of 780-2500nm, especially in the range of 1500-2500nm. With the mass ratio increased, the NIR transmittance would decrease. However, the visible light transmittance would also decrease with the mass ratio increased, especially in sample A and B. This is because that the abundant bubbles on the coating surface would decrease the light transmittance. Sample E exhibited the lowest blocking rate in NIR light range, because that the poor ionic conduction leads to a low doped TiO_2, which would reduce the NIR light absorption.

Figure 8.17 the UV-Vis-NIR transmittance of the samples under different mass ratio between deionized water and ethylene glycol

(A: pure water; B: 2:1; C: 1:1; D: 1:2; E: pure ethylene glycol)

According to the UV-Vis-NIR transmittance value of the samples under different mass ratio between deionized water and ethylene glycol as shown in Table 8.4, the mass ratio of sample C may be the optimum value of 1:1, which exhibited a high visible light transmittance and high NIR light blocking rate.

Table 8.4 The UV-Vis-NIR transmittance value of the samples under different mass ratio between deionized water and ethylene glycol

(A: pure water; B: 2:1; C: 1:1; D: 1:2; E: pure ethylene glycol)

Sample	UV-light	Visible light	IR light
A	15.4%	57.8%	32.6%
B	16.3%	59.2%	36.7%
C	21.4%	72 %	38.2%
D	25.9%	72.3%	40.3%
E	27.3%	78.4%	49.8%

Figure 8.18 shows the WCA of the samples under different mass ratio between deionized water and ethylene glycol. It could be found that the WCA would be decreased with the mass ratio decreased. Because that the doped degree was increased by the enhancement of the mass ratio, it exhibited a positive effect on the photocatalysis property of the black-TiO$_2$ film, and the results was consisting with the results shown in the XRD pattern.
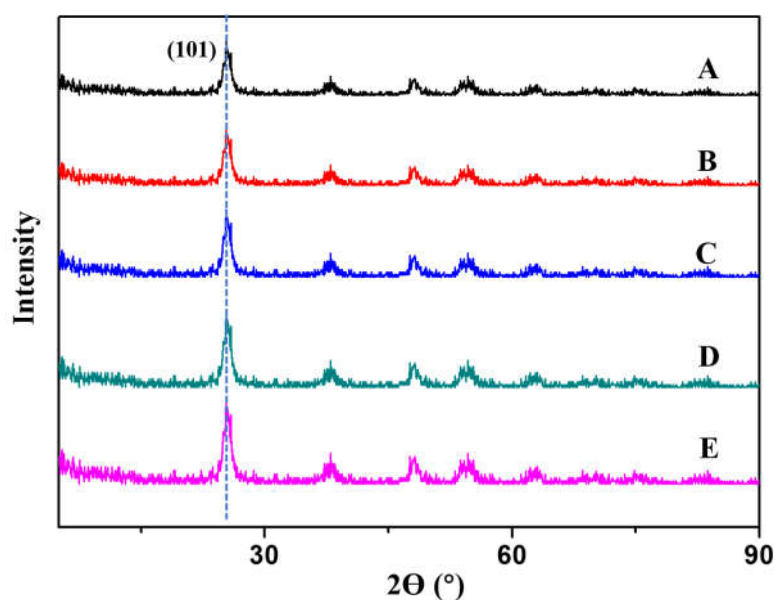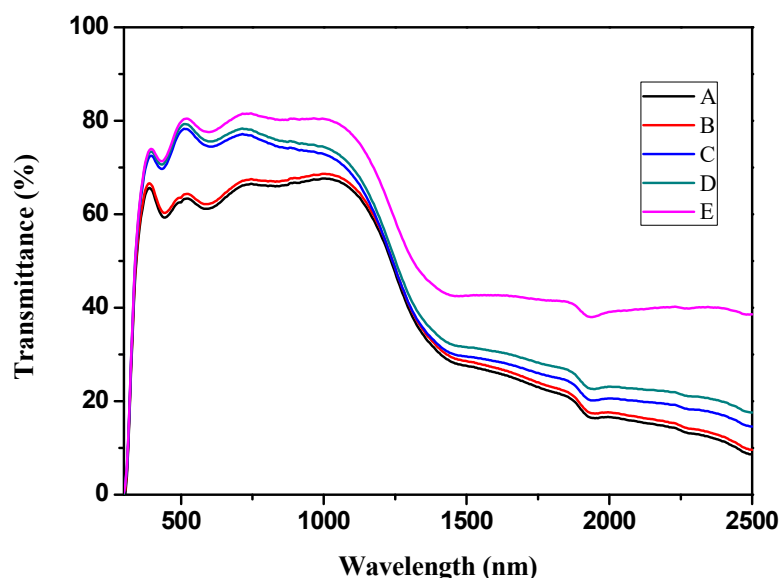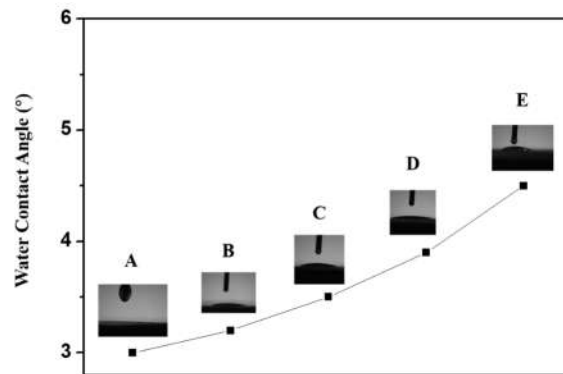
Figure 8.18 The WCA of the samples under different mass ratio between deionized
water and ethylene glycol

(A: pure water; B: 2:1; C: 1:1; D: 1:2; E: pure ethylene glycol)

Figure 8.19 shows the degradation efficiency of the MB solution degraded by the different samples in different time. Plus, the Table 8.5 shows the degradation efficiency value of the MB solution degraded by the samples in different mass ratio between deionized water and ethylene glycol under different time.
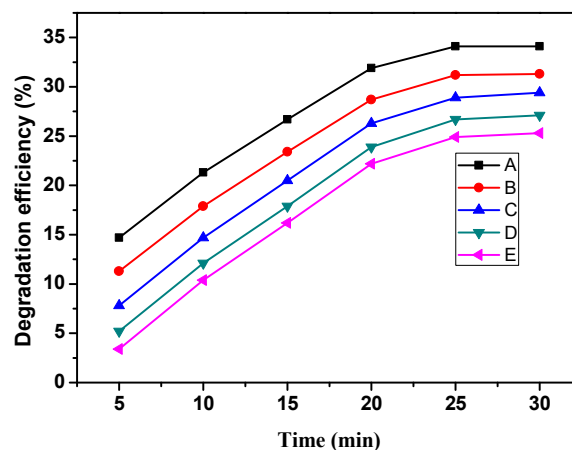
Figure 8.19 The degradation efficiency (%) of the MB solution degraded by the
samples in different mass ratio between deionized water and ethylene glycol under
different time

(A: pure water; B: 2:1; C: 1:1; D: 1:2; E: pure ethylene glycol)

It could be found that the degradation efficiency of the MB solution was increased with the ration increased, which is consist with the result of the WCA shown in figure 8.18.

Table 8.5The degradation efficiency (%) of the MB solution degraded by the samples in different mass ratio between deionized water and ethylene glycol under different time (A: pure water; B: 2:1; C: 1:1; D: 1:2; E: pure ethylene glycol)

Sample	5min	10min	15min	20min	25min	30min
A	14.7	21.3	26.7	31.9	34.1	34.1
B	11.3	17.9	23.4	28.7	31.2	31.3
C	7.8	14.7	20.5	26.3	28.9	29.4
D	5.2	12.1	17.9	23.9	26.7	27.1
E	3.4	10.4	16.2	22.2	24.9	25.3

Owing to the above investigation, the optimum of the mass ratio between deionized water and ethylene glycol was 1:1.

8.3.3.3 The effect of the voltage in the electrochemistry reaction on the property of the black-TiO₂ film

The power in the electrochemistry reaction is very important, which can affect the extent of reaction and the final product. In this section, the electricity would maintain a fixed value of 2A. In addition, the effect of voltage in the reaction on the property of

the black-TiO$_2$ film would be investigated. Black-TiO$_2$ film was fabricated as conducted in 8.2.2. The voltage would be adjusted at 2V, 5V, 8V and 10V. The NH$_4$Cl mass concentration and the mass ratio between the deionized water and ethylene glycol were kept at 15wt% and 1:1, respectively. Meanwhile, the reaction time was kept in 10 minutes.
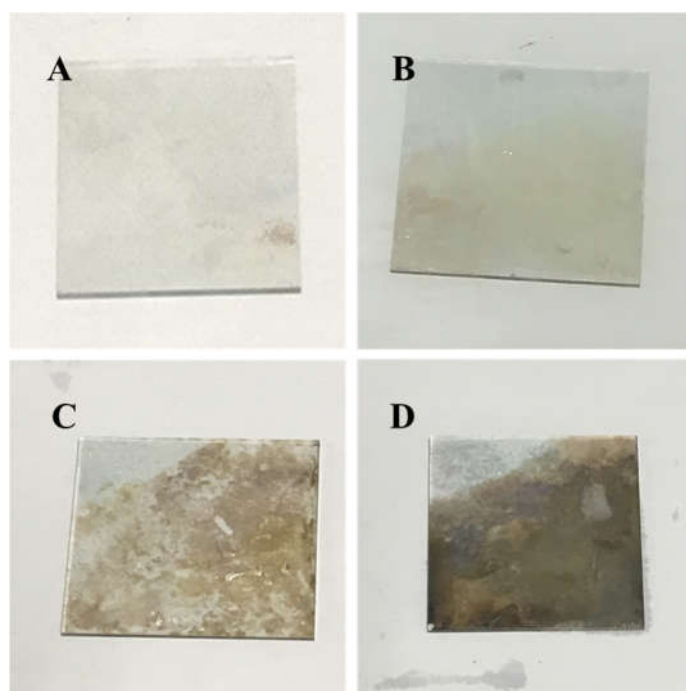
Figure 8.20 The photos of the samples in different voltage

A: 2V; B: 5V; C: 8V; D: 10V;

Figure 8.20 shows the photos of the samples under different voltage in reaction. It could be found that the color would be changed darker with the voltage increased, due to the high voltage can increase the ionic conduction in the electrolyte solution. Hence, a positive effect was on the electrochemistry reaction which can increase the doped

degree of black-TiO_2. However, a nonuniform coating surface can be found in the photos, when the voltage higher than 5V, because the bubble on the coating surface would be increased with the ionic conduction be improved. Thus, the voltage in electrochemistry reaction is very important.

Figure 8.21 shows the XRD pattern of the samples in different voltage. It could be found that the peak positions of samples are well agree with the reflections of anatase TiO_2, and no other impurity peaks in samples can be recorded, which indicates that the black-TiO_2 with anatase crystal form was obtained. By calculating the peak intensity from the XRD data, it clearly shows that the peak intensity of [101] direction decreases slightly with the increase of voltage in the reaction, because the doped degree was increased.

Figure 8.21 The XRD pattern of the samples under different voltage in reaction

A: 2V; B: 5V; C: 8V; D: 10V

Figure 8.22 shows the UV-Vis-NIR transmittance of the samples under different voltage in reaction. It could be found that all the samples exhibited a high transmittance in the visible light range of 380~780nm, and a high blocking rate in the NIR light range of 780-2500nm, especially in the range of 1500-2500nm. With voltage increased, the NIR transmittance would decrease. However, the visible light transmittance would also decrease with the voltage increase, especially in the sample C and D. This is because that the abundant bubbles on the coating surface would decrease the light transmittance.
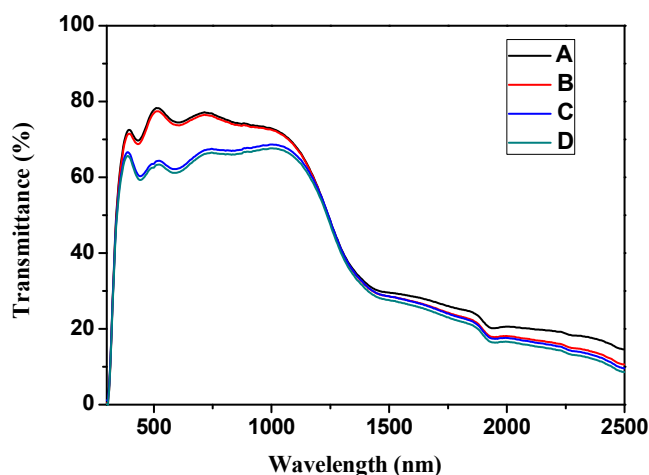
Figure 8.22 The UV-Vis-NIR transmittance of the samples under different voltage A: 2V; B: 5V; C: 8V; D: 10V

According to the UV-Vis-NIR transmittance test, sample B under the voltage of 5V exhibited a high visible light transmittance and high blocking rate.

Table 8.6 The UV-Vis-NIR transmittance value of the samples under different voltage A: 2V; B: 5V; C: 8V; D: 10V

Sample	UV-light	Visible light	IR light

A	22.3%	74.6%	44.8%
B	21.4%	72 %	38.2%
C	17.3%	53.6%	36.3%
D	15.2%	52.7%	36.1%

Figure 8.23 shows the WCA of the samples under different voltage in reaction. It could be found that the WCA would be slightly decreased with the voltage increased. Because that the doped degree of black TiO_2 was increased by the improvement of the voltage, which exhibited a positive effect on the photocatalysis property of the black-TiO_2 film, and the results was consist with the results shown in the XRD pattern.
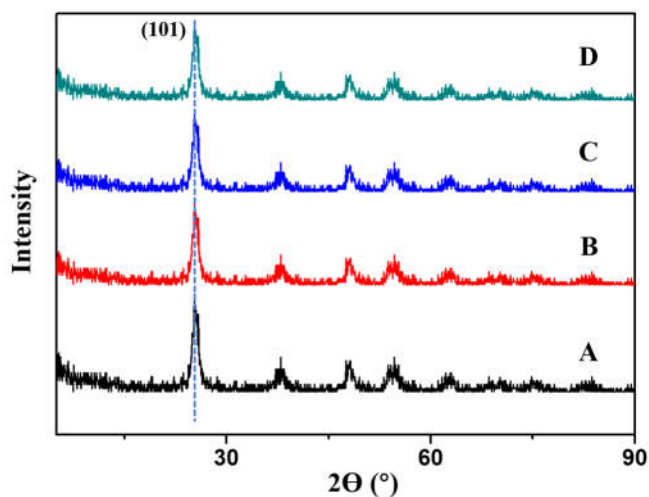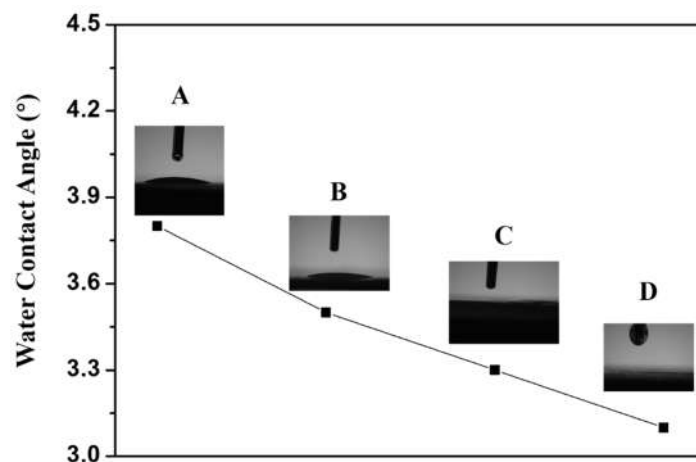

Figure 8.23 The WCA of the samples under different voltage in reaction

A: 2V; B: 5V; C: 8V; D: 10V

Figure 8.24 shows the degradation efficiency of the MB solution degraded by different samples in different time. Meanwhile, Table 8.7 shows the degradation

efficiency value of the MB solution degraded by the samples in different voltage under different time.

Figure 8.24 The degradation efficiency of the MB solution degraded by the samples under different voltage in different time

A: 2V; B: 5V; C: 8V; D: 10V

It could be found that the degradation efficiency of the MB solution was increased with the voltage increased, due to the doped degree increased, which is consist with the result of the WCA shown in figure 8.23

Table 8.7 The degradation efficiency (%) of the MB solution degraded by the samples under different voltage in different time

A: 2V; B: 5V; C: 8V; D: 10V

Sample	5min	10min	15min	20min	25min	30min
A	6.5	13.5	19.2	25.1	27.8	28.3

B	7.8	14.7	20.5	26.3	28.9	29.4
C	10	16.8	22.6	28.4	31.1	31.5
D	11.6	18.3	24.1	29.7	32.6	32.9

Owing to the above investigation, the optimum voltage in the electrochemistry reaction was 5V.

8.3.3.4 The effect of the reaction time in the electrochemistry reaction on the property of the black-TiO₂ film

Reaction time is very important in the electrochemistry reaction, due to the effect on the doped degree of the black TiO_2 film. In this section, the effect of the reaction time would be investigated. The electricity and the voltage in the reaction were maintained at 2A and 5V, respectively. The mass concentration of the NH_4Cl and mass ratio between deionized water and ethylene glycol were 15wt% and 1:1, respectively. The coating process was conducted in 8.2.2. The reaction time was adjusted at 3, 5, 10 and 15 minutes.

Figure 8.25 shows the photos of the samples under different reaction time. It could be found that the color would be changed darker with the reaction time extend, due to the long reaction time can increase the doped degree of the black TiO_2 films. Thus, the voltage in electrochemistry reaction is very important.

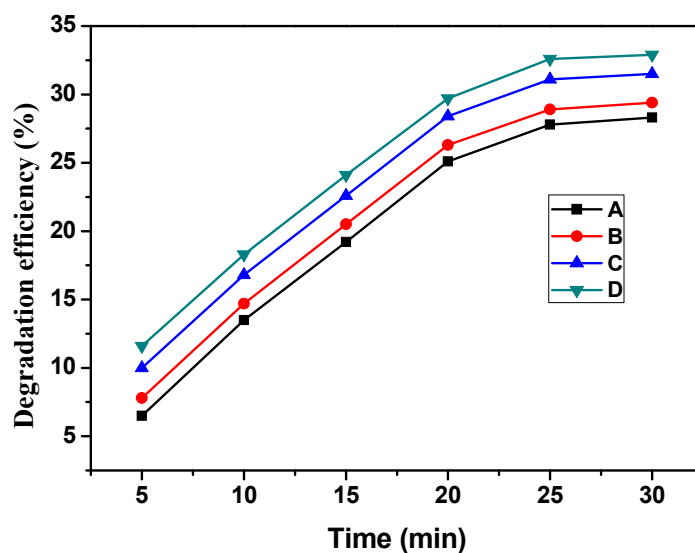Figure 8.25 The photos of the samples under different reaction time

A: 3min; B: 5min; C: 10min; D: 15min

Figure 8.26 shows the XRD pattern of the samples in different voltage. It could be found that the peak positions of samples are well agree with the reflections of anatase TiO_2, and no other impurity peaks in samples can be recorded, which indicates that the black-TiO_2 with anatase crystal form was obtained. By calculating the peak intensity from the XRD data, it clearly shows that the peak intensity of [101] direction decreases slightly with the increase of reaction time in the reaction, because the doped degree was increased. When the reaction time was longer than 10 minutes, the peak intensity shown a slight change, because the doped element was tended to a limit value.
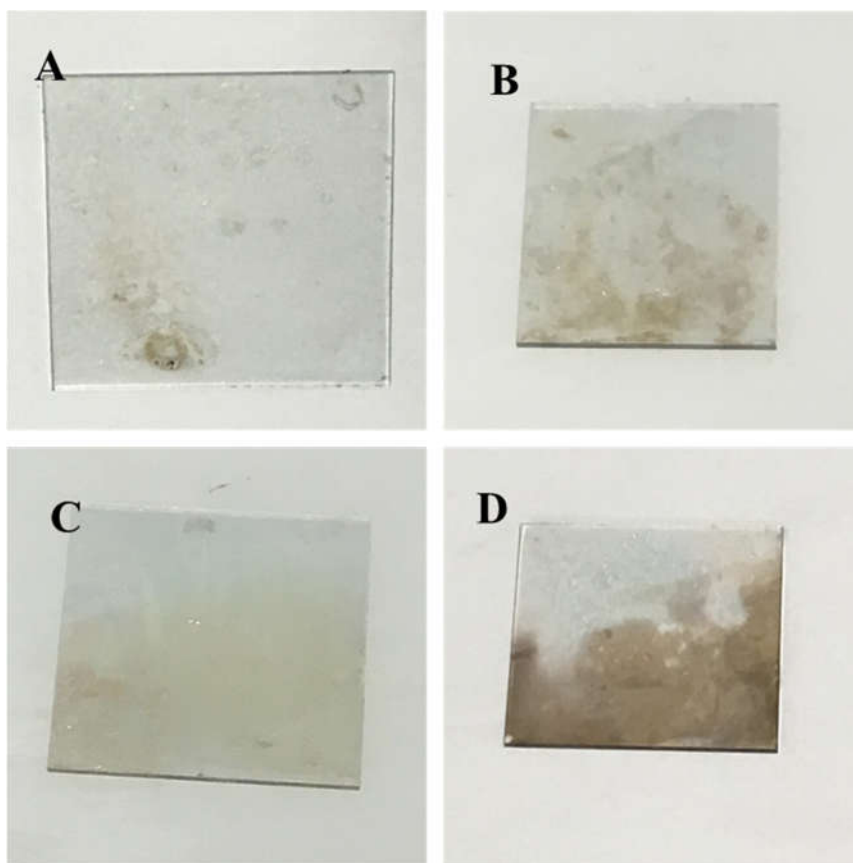
Figure 8.26 The XRD pattern of the sample under different reaction time

A: 3min; B: 5min; C: 10min; D: 15min

Figure 8.27 shows the UV-Vis-NIR transmittance of the samples under different reaction time. It could be found that all the samples exhibited a high transmittance in the visible light range of 380~780nm, and a high blocking rate in the NIR light range of 780-2500nm, especially in the range of 1500-2500nm. With reaction time extending, the NIR transmittance would decrease. After the reaction time longer than 10min, the light transmittance exhibited a slight change, which was consist with the results shown in the XRD pattern.
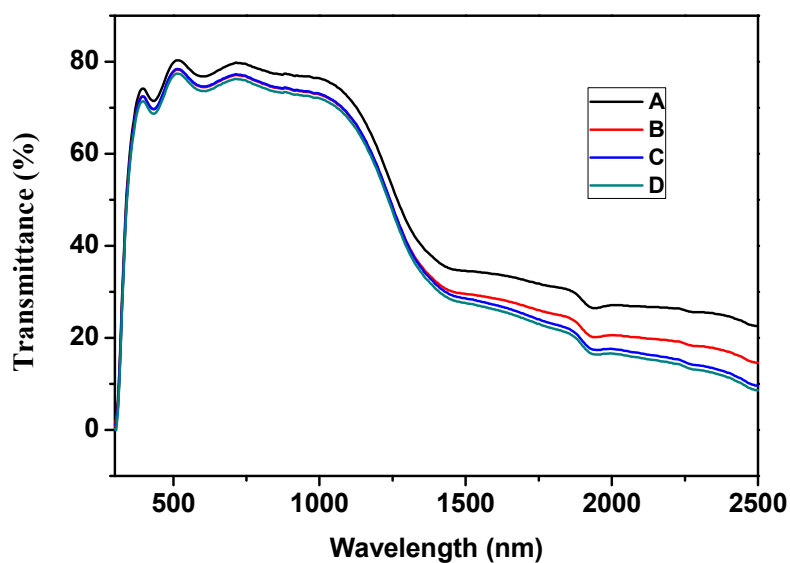
Figure 8.27 The UV-Vis-NIR transmittance of the samples under different reaction time (A: 3min; B: 5min; C: 10min; D: 15min)

According to the UV-Vis-NIR transmittance test, the sample C and sample D exhibited a high visible light transmittance and high NIR light blocking rate.

Table 8.8 The UV-Vis-NIR transmittance of the samples under different reaction time A: 3min; B: 5min; C: 10min; D: 15min

Sample	UV-light	Visible light	IR light
A	25.3%	78.4%	43.4%
B	23.6%	75.2%	40.2%
C	21.4%	72 %	38.2%
D	20.8%	71.6%	37.7%

Figure 8.28 shows the WCA of the samples under different reaction time. It could be found that the WCA would be decreased with the reaction time increased. Because

that the doped degree of black TiO$_2$ was increased caused by the reaction time extension, which exhibited a positive effect on the photocatalysis property of the black-TiO$_2$ film, and the results was consist with the results shown in the XRD pattern.
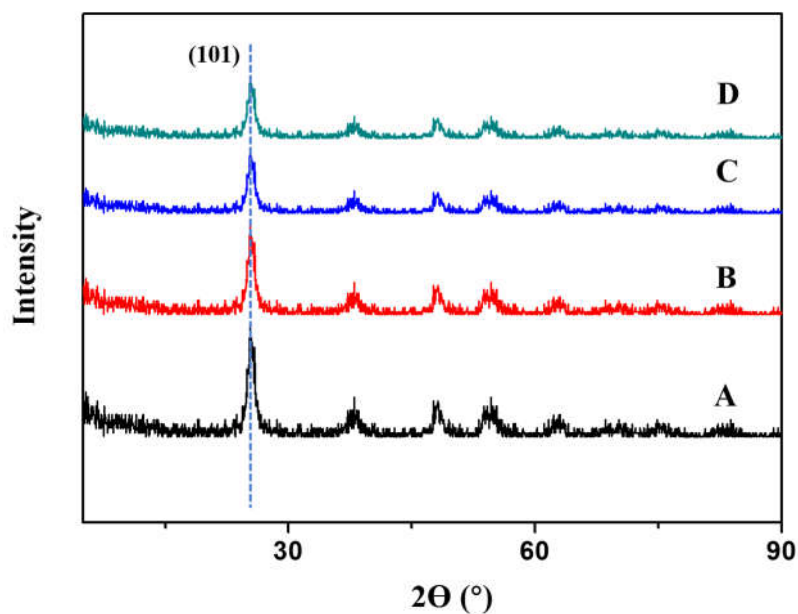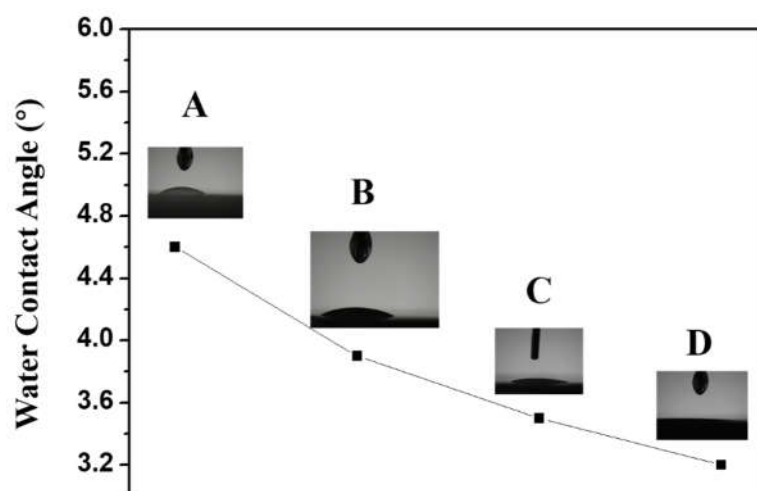

Figure 8.28 The WCA of the samples under different reaction time

A: 3min; B: 5min; C: 10min; D: 15min

Figure 8.29 shows the degradation efficiency of the MB solution degraded by the different samples in different time. Plus, Table 8.9 shows the degradation efficiency value of the MB solution degraded by the samples in different reaction time in electrochemistry reaction under different time.
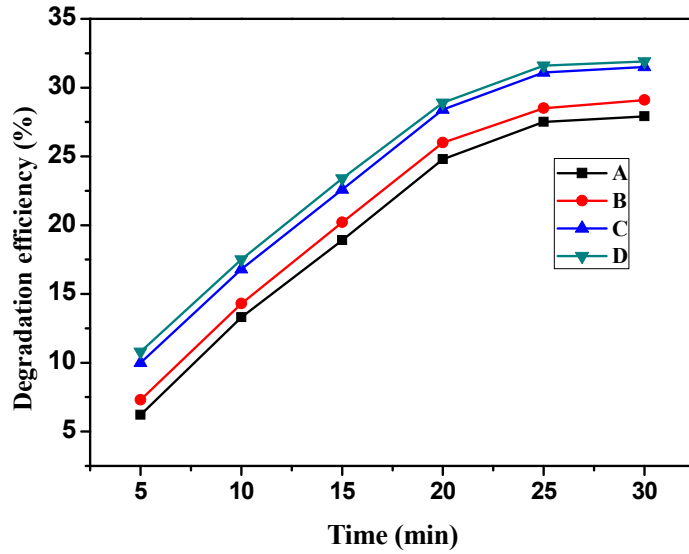
Figure 8.29 The degradation efficiency of the MB solution degraded by the different
samples in different time (A: 3min; B: 5min; C: 10min; D: 15min)

It could be found that the degradation efficiency of the MB solution was increased

with the reaction time extending, due to the doped degree increased, which is consist

with the result of the WCA shown in figure 8.29.

Table 8.9 The degradation efficiency (%) of the MB solution degraded by the
different samples in different time (A: 3min; B: 5min; C: 10min; D: 15min)

Sample	5min	10min	15min	20min	25min	30min
A	6.2	13.3	18.9	24.8	27.5	27.9
B	7.3	14.3	20.2	26	28.5	29.1
C	7.8	14.7	20.5	26.3	28.9	29.4
D	10.8	17.5	23.4	28.9	31.6	31.9

Owing to the above investigation, the optimum reaction time in the

electrochemistry reaction was 10 minutes.

8.4 Conclusion

In this chapter, the black-TiO$_2$ films were fabricated by the controllable hydrothermal reaction and electrochemistry reaction. The effects of hydrochloric acid concentration, NH$_4$Cl concentration in electrochemistry, mass ratio between deionized water and ethylene glycol, voltage, and reaction time in electrochemistry were investigated, and finally the optimum reaction conditions were obtained. Details are as follows:

1. In self-dispersion TiO$_2$ synthesis, the optimum pH value of the reactant was 5.62, which exhibited a high visible light transmittance of 99.1% and low WCA of 7.6°. Meanwhile, the UV blocking rate and NIR blocking rate were 4.3% and 0.2%, respectively.

2. Using the NH$_4$Cl as the electrolyte and adjusting the concentration of the NH$_4$Cl to 15wt%. The electricity and the voltage were adjusted as 2A and 5V, respectively. The ratio of the deionized water to ethylene glycol was 1:1. In addition, the reaction time of electrochemistry was kept in 10min. Finally, the Optimization of the black-TiO$_2$ would be obtained, which exhibited a high visible light transmittance of 72%, and high NIR light blocking rate of 61.8%. Meanwhile, the black-TiO$_2$ film shows a WCA lower than 5°, and a high degradation efficiency of the MB solution. It means that the black TiO$_2$ film could not only be used as a self-cleaning coating but also can be applied on

window glass to reduce the heat gain from the sunlight.

8.5 Reference

[1] Sambur, J. B., Novet, T., & Parkinson, B. A. (2010). Multiple exciton collection in a sensitized photovoltaic system. *Science*, *330*(6000), 63-66.

[2] Green, M. A., Emery, K., Hishikawa, Y., & Warta, W. (2011). Solar cell efficiency tables (version 37). *Progress in photovoltaics: research and applications*, *19*(1), 84-92.

[3] Chapin, D. M., Fuller, C. S., & Pearson, G. L. (1954). A new silicon p-n junction photocell for converting solar radiation into electrical power. *Journal of Applied Physics*, *25*(5), 676-677.

[4] Kamat, P. V. (2008). Quantum dot solar cells. Semiconductor nanocrystals as light harvesters. *The Journal of Physical Chemistry C*, *112*(48), 18737-18753.

[5] O'regan, B., & Grätzel, M. (1991). A low-cost, high-efficiency solar cell based on dye-sensitized colloidal TiO2 films. *nature*, *353*(6346), 737.

Chapter 9 Development and Characterization of Structural Black-TiO$_2$/Nano ATO/Nano Cs$_x$WO$_3$ Thermal Insulation Coating

9.1 Introduction

With the development of science and technology, energy and environmental problems are becoming more serious. Photocatalyst, a kind of catalyst can decompose the organic pollutant through light absorption, has attracted great interests of scientists. More recently, TiO$_2$ has become the research focus of photocatalyst, due to its low cost, simple synthesis, high stability and non-poisonous for human body [1-3].

As the investigation in Chapter 8, the black TiO$_2$ exhibit a visible light and NIR light absorption in the range of 400-2500nm, because there are two kinds of electronic excitation. One is from valence band to conduction band, and another is from valence band to interstitials or from interstitials to conduction band. The black TiO$_2$, a kind of modified semiconductor oxides, has a narrow energy gap, which lead to a high electrical conductivity.

Black-TiO$_2$ shows a high potential of the application in environment. TiO$_2$ can process the free electronic and hole after light irradiation, which can combine with the O$_2$ and H$_2$O and become free radical with high oxidizing ability. Comparing with traditional anatase TiO$_2$, the black TiO$_2$ shows a broad band of light absorption, which can enhance the photocatalysis property. Meanwhile, black TiO$_2$ also shows a high potential in the thermal insulation property, due to the NIR light absorption of Black-

TiO$_2$ [4-5].

According to the above investigation in Chapter 5, the optimum mass ratio between ATO nanoparticles and Cs$_x$WO$_3$ nanoparticles was 1:1. In addition, this two-components coating exhibited a high visible light transmittance of 74.3% and a high NIR light blocking rate of 90.4%. Hence, in order to improve NIR light shielding property, a novel structural black-TiO$_2$/ATO/Cs$_x$WO$_3$ thermal insulation coating would be developed in this chapter, which also exhibited a high photocatalysis property. The optical properties of the coating were characterized and studied in detail.

9.2 Experiment

9.2.1 Coating Process

To avoid the decomposition of the film-forming resin in the two-components coating based on ATO/Cs$_x$WO$_3$, the black TiO$_2$ would be coated on another side of the glass. The fabrication of the two-component coating based on ATO/Cs$_x$WO$_3$ was conducted in 7.2.1, and the fabrication of the black-TiO$_2$ film was conducted in 6.2. The mass ratio between ATO nanoparticles and Cs$_x$WO$_3$ nanoparticles was 1:1, and the mass concentration of the ATO and Cs$_x$WO$_3$ nanoparticles in the two-components thermal insulation coating was 20wt%.

In the black-TiO$_2$ film process, the mass concentration of the self-dispersion TiO$_2$ was 5wt%. The electricity and the voltage in electrochemistry was 2A and 5V, respectively. The mass concentration of the electrolyte as NH$_4$Cl and the mass ratio between deionized water and the ethylene glycol in electrochemistry was 15wt% and

1:1, respectively.

9.2.2 Film Process

Firstly, the black-TiO$_2$ film was coated on one side of the glass sheet, which was conducted as 6.2.2. then the two-component thermal insulation coating based on nano ATO/nano Cs$_x$WO$_3$ was sprayed on the surface of another side by automatic spraying equipment which was conducted as 7.2.1.2. The details of the film process are shown in Figure 9.1. Plus, the diagram of the final structural black TiO$_2$/ATO/Cs$_x$WO$_3$ thermal insulation coating is shown in figure 9.2.
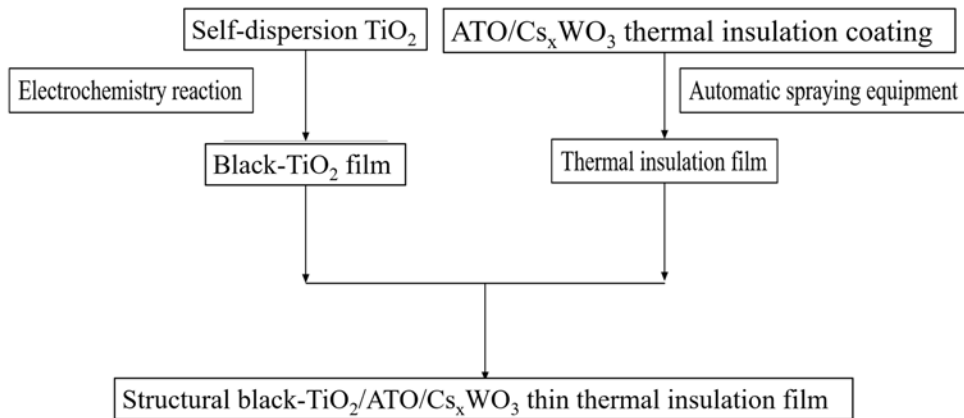

Figure 9.1 The flow chart of the structural black-TiO$_2$/ATO/Cs$_x$WO$_3$ thermal insulation coating
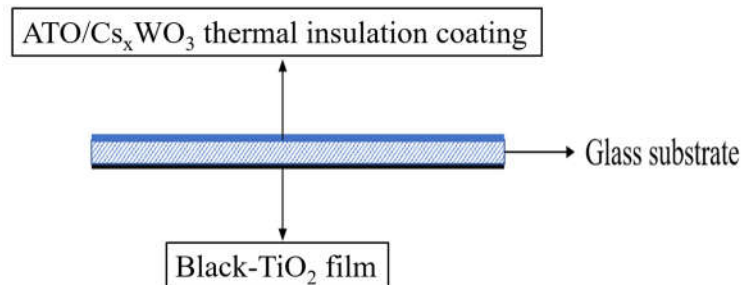

Figure 9.2 The Diagram of the structural black TiO$_2$/ATO/Cs$_x$WO$_3$ thermal insulation coating filmed on the glass substrate

9.2.3 Characterization of the structural black TiO_2/ATO/Cs_xWO_3 thermal insulation coating

The optical property of the structural coating would be measured by the UV-Vis-NIR spectrophotometer. The WCA and the thickness of the coating would be recorded by the contact angle meter and stylus profiler of Alpha Step D-500 (KLA-Tencor).

9.3 Results and Discussion

9.3.1 Optical property of the structural thermal insulation coating with different thickness of the ATO/Cs_xWO_3 thin film.

In this section, the effect of the thickness about the ATO/Cs_xWO_3 thin film on the optical property of the structural thermal insulation coating would be investigated. The two-components coating based on nano ATO and nano Cs_xWO_3 was filmed on the glass substrate with block-TiO_2 film on another side through the automatic spraying equipment. The thickness of the two-component coating could be adjusted by changing the conditions of film process. Meanwhile, the thickness of the thermal insulation coating would be measured by the stylus profiler. The mass content of the ATO and Cs_xWO_3 nanoparticles was 20wt%, and the mass ratio between the ATO and Cs_xWO_3 was 1:1.

Figure 9.3 shows the transmittance of the structural thermal insulation coating in different thickness of the ATO/Cs_xWO_3 two-component coating. It could be found that the transmittance of the visible light and NIR light were decreased with the thickness of the ATO/Cs_xWO_3 two-component coating be enhanced.
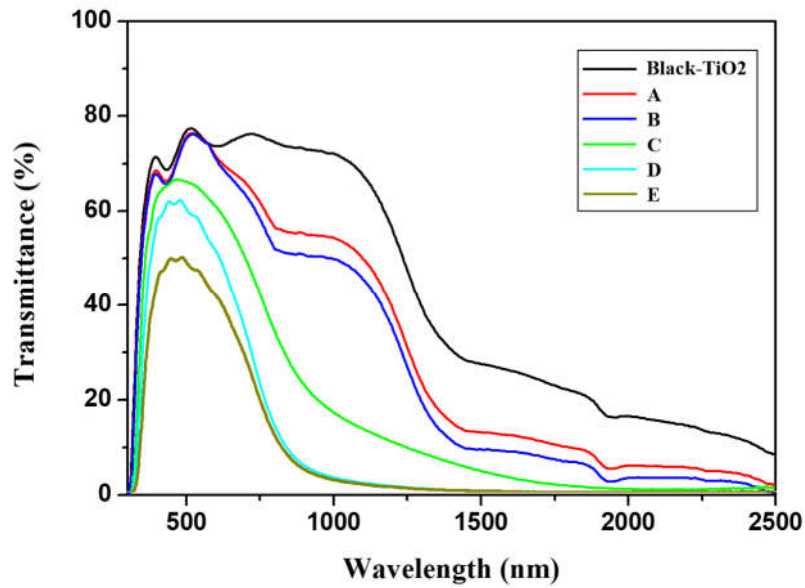
Figure 9.3 The Transmittance of the structural thermal insulation coating in different thickness of the ATO/Cs$_x$WO$_3$ two-components coating

(A: 0.94μm; B: 1.29μm; C: 3.864μm; D: 4.63μm; E: 5.02μm)

Table 9.1 shows the integral computation of the transmittance in UV light range, visible light range and NIR light range. It could be found that a rapid decrease was in the visible light and NIR light transmittance, when the thickness of ATO/Cs$_x$WO$_3$ two-component coating greater than 3.84μm. However, the visible light also exhibited a rapid decrease, especially the thickness of the two-components coating greater than 1.29μm. When the thickness greater than 4.63μm, the shielding performance in NIR light range just shows a slight increase, while the transmittance in visible light range show a rapid decrease. Hence, the optimum thickness of the ATO/Cs$_x$WO$_3$ two-component coating was 4.63μm.

Table 9.1 The integral computation of the transmittance in UV light range, visible light range and NIR light range with different thickness of the ATO/Cs$_x$WO$_3$ two-components coting (A: 0.94μm; B: 1.29μm; C: 3.864μm; D: 4.63μm; E: 5.02μm)

Sample	UV light (%)	Visible light (%)	NIR light (%)
Black-TiO$_2$	21.4	72	38.2
A	20.3	68.2	25.1
B	18.7	66.3	23.2
C	15.2	62.7	15.5
D	3.2	58.6	6.3
E	1.7	42.3	5.4

9.3.2 The characterization of the optimum structural black TiO$_2$/ATO/Cs$_x$WO$_3$ thermal insulation coating

According to the above investigation, the optimum of the structural black-TiO$_2$/ATO/Cs$_x$WO$_3$ thermal insulation coating would be fabricated. The mass ratio between ATO nanoparticles and Cs$_x$WO$_3$ nanoparticles was 1:1 and the mass concentration of the nano ATO/Cs$_x$WO$_3$ in the two-component coating was 20wt%. The black TiO$_2$ film was fabricated by the electrochemistry under the electricity and voltage of 2A and 5V, respectively. The concentration of NH$_4$CL was 15wt% and the mass ratio between deionized water and ethylene glycol in electrochemistry reaction was 1:1.
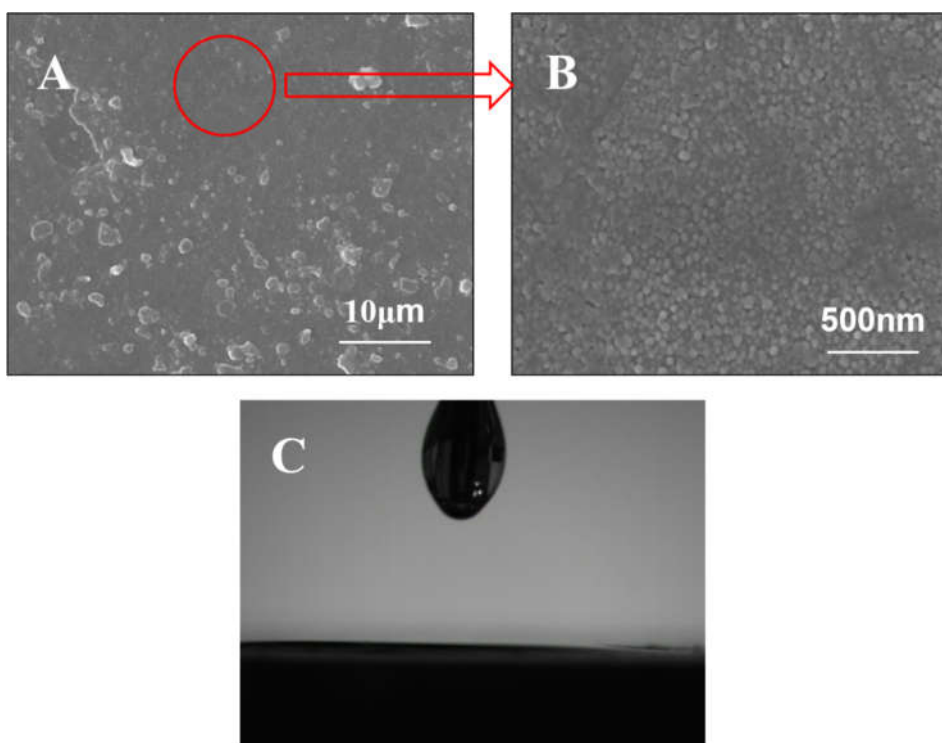
Figure 9.4 The SEM image (A and B) and the WCA (C) of on the side of black-TiO$_2$ thin film

The surface morphology of the side of black-TiO$_2$ thin film was shown in the SEM image in Figure 9.4 A and Figure 9.4 B. It could be found that an even thin film was on the surface of the glass substrate. The nanoparticles in the figure 9.4B was lower than 10nm. Meanwhile the coating shows an excellent self-cleaning property, which was represented in WCA of lower than 5° as shown in Figure 9.4C.

Figure 9.5 shows the XRD pattern of the black-TiO$_2$ thin film on the one side of the glass substrate. It could be found that the peak positions of sample are well agree with the reflections of anatase TiO$_2$, and no other impurity peak in samples can be recorded, which indicates that the black-TiO$_2$ with anatase crystal form was obtained

Figure 9.5 The XRD pattern of the black-TiO$_2$ thin film on the one side of the glass substrate
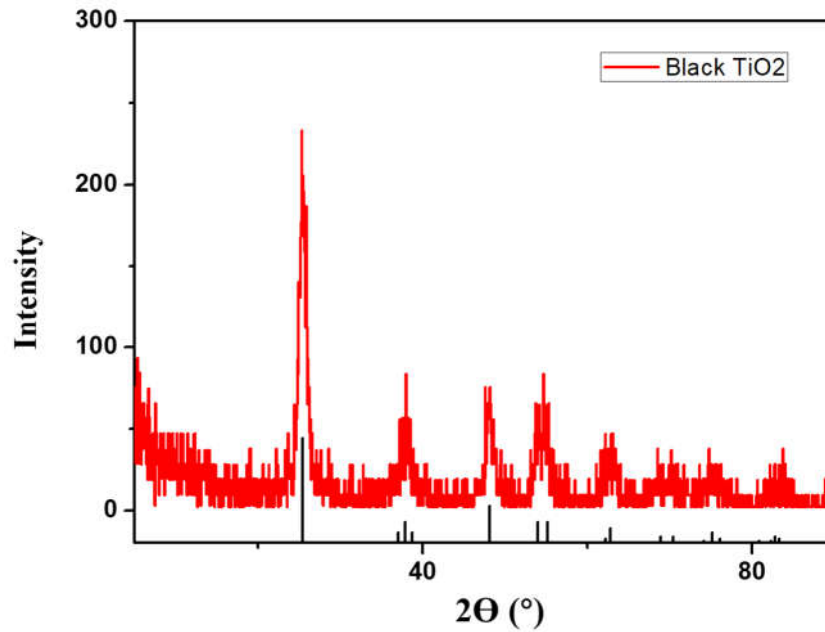
Figure 9.6 shows the SEM image of the two-component coating based on ATO/Cs$_x$WO$_3$ on another side of the glass substrate. The glass substrate with the two-component coating was placed on the sample stage which was in a dip angle of 45° as shown in figure 9.6A. The thickness of the two-component coating would be observed in this image and the dried resin mixed with nanoparticles could be observed in Figure 9.6B.

The two-component coating based on ATO/Cs$_x$WO$_3$ was in reciprocating friction by high speed reciprocating wear tester of MFT-EC400. The wear method was ball-plate reciprocating sliding friction. The grinding unit was Al$_2$O$_3$ ceramic ball in the diameter of 6mm, and the surface roughness was 0.032μm (GBC 308-2002). Besides, the hardness of the grinding unit was 1600HV. The grinding unit was added in a load of 5N, and the reciprocating frequency was 3Hz. After the wear test, the surface

morphology of the two-component coating was recorded by the SEM image in Figure 9.6C and 9.6D. It could be found that the coating was still on the surface of the glass substrate and the particle size of the nano ATO/Cs$_x$WO$_3$ was lower than 5nm.
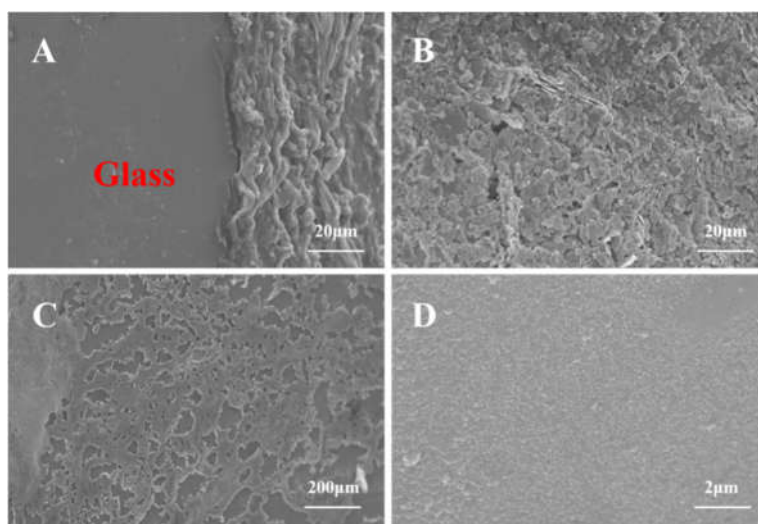
Figure 9.6 The SEM image of the two-components coating based on ATO/Cs$_x$WO$_3$ on another side of the glass substrate (A: Sample stage on 45°; B: Sample stage on horizontal; C: Sample after friction measurement; D: Amplification of the image C)

Figure 9.7 shows the degradation efficiency of the MB solution degraded by the different samples in different time. Plus, the table 9.2 shows the degradation efficiency value of the MB solution degraded by the samples of original glass, two-component coating, self-dispersed TiO$_2$ coating and structural black-TiO$_2$/ATO/Cs$_x$WO$_3$ coating.
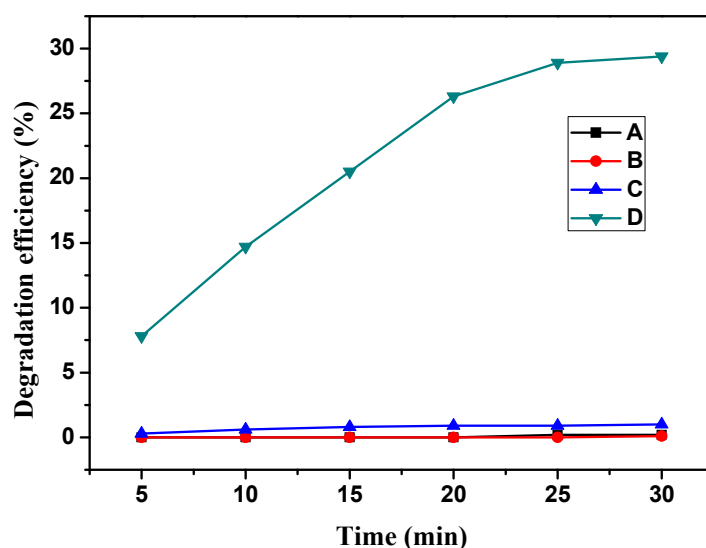
Figure 9.7 The degradation efficiency value of the MB solution degraded by different samples (A: Original glass; B: Two-components coating; C: Self-dispersed TiO_2 coating; D: Structural black-TiO_2/ATO/Cs_xWO_3 coating)

It could be found that the original glass and two-component coating did not show the photocatalysis property. Sample C show a poor photocatalysis property, due to the low light absorption and narrow light absorption range. The structure black-TiO_2/ATO/Cs_xWO_3 thermal insulation coating exhibited an excellent photocatalysis property of high MB solution degradation.

Table 9.2 the degradation efficiency value (%) of the MB solution degraded by different samples (A: Original glass; B: Two-components coating; C: Self-dispersed TiO_2 coating; D: Structural black-TiO_2/ATO/Cs_xWO_3 coating)

Sample	5min	10min	15min	20min	25min	30min
A	0	0	0	0	0.2	0.2
B	0	0	0	0	0	0.1
C	0.3	0.6	0.8	0.9	0.9	1.0

| D | 7.8 | 14.7 | 20.5 | 26.3 | 28.9 | 29.4 |

9.3.3 Optical property comparison between structural thermal insulation coating, Low-E glass, and tinted glass

To compare with other thermal insulation glass, Low-E glass and tinted glass would be purchased for this experiment. The size of the Low-E glass and tinted glass was 0.3m×0.3m×0.005m. The fabrication of the structural black-TiO_2/ATO/Cs_xWO_3 thermal insulation coating was conducted as 9.2.2. The thickness of the two-component coating in the structure thermal insulation coating was 4.63μm

Figure 9.8 shows the transmittance of the glass with the structural thermal insulation coating, Low-E glass, tinted glass and original glass. Table 9.3 shows the integral computation of the transmittance about the glass with structural thermal insulation coating, Low-E glass, tinted glass and original glass in UV light range, visible light range and NIR light range.

It could be found that the original glass only shows a small UV light blocking rate, while original glass shows a high transmittance in both visible light and NIR light range. Compared with the Low-E glass and tinted glass, the glass with structural thermal insulation coating exhibited a higher NIR light blocking rate of 93.7% and a higher UV light blocking rate of 96.8%. Meanwhile, the glass with structural thermal insulation coating also shows a visible light transmittance of 58.6%. Besides, the structural shows a low WCA of 3.5° and high degradation efficiency of the MB solution, which exhibited an excellent photocatalytic property.
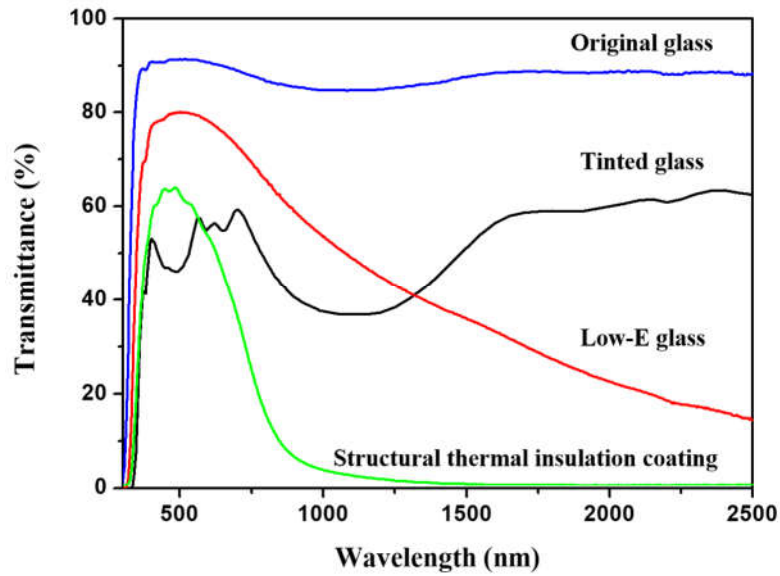
Figure 9.8 The transmittance of the glass with the structural thermal insulation coating, Low-E glass, tinted glass and original glass

Table 9.3 The integral computation of the transmittance about the glass with structural thermal insulation coating, Low-E glass, tinted glass and original glass in UV light range, visible light range and NIR light range.

Sample	UV light (%)	Visible light (%)	NIR light (%)
Glass with coating	3.2	58.6	6.3
Low-E glass	33.9	76.2	34.1
Tinted Glass	15.9	66.8	36.7
Original Glass	49.4	88.1	81.9

9.4 Conclusion

In this chapter, the structural black-TiO_2/ATO/Cs_xWO_3 thermal insulation coating was fabricated by electrochemistry reaction and automatic spraying equipment. The

effects of the thickness for the two-component ATO/Cs_xWO_3 thin films on the optical property of structural thermal insulation coating was investigated. Plus, finally, the optimum formula of the structural thermal insulation coating was obtained. The details are as follows:

1. The optimum of the two-components coating was 4.63μm. After the ATO/Cs_xWO_3 thin film combined with black TiO_2, the structural coating exhibited a low NIR light transmittance of 6.3%. The visible light of the structural thermal insulation coating was 58.6%.

2. The structural thin films have excellent photocatalytic property, which can degrade 29.4% of methylene blue in 30min. Plus, the WCA of the structural thermal insulation coating was only 3.5°.

3. This chapter firstly investigated the optical property comparison between the glass with structural thermal insulation coating, Low-E glass, tinted glass and original glass. The results show that the glass with the structural thermal insulation coating exhibited a high NIR light blocking rate of 93.7%. Plus, a high UV light blocking rate of 96.8%. Meanwhile, the structural thermal insulation coating still exhibited a visible light transmittance of 58.6%. It means that the structural black-TiO_2/ATO/Cs_xWO_3 thermal insulation coating shows a great potential in energy conservation window.

9.5 Reference

[1] Chen, Z., Li, H., Tang, Y., Huang, X., Ho, D., & Lee, C. S. (2014). Shape-controlled synthesis of organolead halide perovskite nanocrystals and their tunable optical absorption. *Materials Research Express*, *1*(1), 015034.

[2] Wojciechowski, K., Saliba, M., Leijtens, T., Abate, A., & Snaith, H. J. (2014). Sub-150 C processed meso-superstructured perovskite solar cells with enhanced efficiency. *Energy & Environmental Science*, *7*(3), 1142-1147.

[3] Zhou, H., Chen, Q., Li, G., Luo, S., Song, T. B., Duan, H. S., ... & Yang, Y. (2014). Interface engineering of highly efficient perovskite solar cells. *Science*, *345*(6196), 542-546.

[4] Grätzel, M. (2004). Conversion of sunlight to electric power by nanocrystalline dye-sensitized solar cells. *Journal of Photochemistry and Photobiology A: Chemistry*, *164*(1-3), 3-14.

[5] Listorti, A., O'Regan, B., & Durrant, J. R. (2011). Electron transfer dynamics in dye-sensitized solar cells. *Chemistry of Materials*, *23*(15), 3381-3399.

Chapter 10   Conclusions and Prospects

10.1 Summary of the research findings/contributions

To develop a novel thermal insulation coating, a comprehensive investigation of novel NIR-blocking materials combined with ATO has been presented in this thesis. Cs_xWO_3 was selected to be mixed with ATO due to its high light absorption in the wavelength of 800-1500nm. Meanwhile, the black-TiO_2 film was selected to combine with the two-component thermal insulation coating based on ATO/Cs_xWO_3, due to its high NIR light absorption and high self-cleaning property. The major findings achieved by this investigation are concluded as follows:

10.1.1 The Synthesis and preparation of nano ATO and ATO aqueous dispersions

Firstly, the ATO nanoparticles has been synthesized by the controllable hydrothermal reaction and dispersed in water with surfactant. The effects of doping content, reaction time and reaction temperature on the morphology and optical properties of ATO were investigated, by which the optimum reaction conditions were obtained. The optimum of the Sb doping content was 10%. Besides, the optimum reaction temperature and optimum reaction time was 230°C and 12h, respectively. In addition, a blue transparency liquid of ATO dispersion aqueous was obtained through the surfactant agent SIM6492.72 and high-speed ball mill, which exhibited a low secondary particle size distribution of 28.1nm, and the liquid was without sedimentation after 7 days.

10.1.2 The Synthesis and preparation of nano Cs$_x$WO$_3$ and Cs$_x$WO$_3$ aqueous dispersions

To enhance the NIR light absorption of the ATO, a novel thermal insulation material was synthesized through controllable hydrothermal reaction and dispersed in water with surfactant. The effect of citric acid content, doping content, reaction time and reaction temperature on the morphology and optical properties of Cs$_x$WO$_3$ were investigated, by which the optimum reaction conditions were obtained. The optimum of the Cs doping content was 30%. Besides, the optimum reaction temperature and optimum reaction time was 220°C and 12h, respectively. In addition, a blue transparency liquid of Cs$_x$WO$_3$ dispersion aqueous was obtained through the surfactant agent SN5040 and high-speed ball mill, which exhibited a low secondary particle size distribution of 62.7nm, and the liquid was without sedimentation after 7 days.

10.1.3 Nano ATO/Nano Cs$_x$WO$_3$ thermal insulation coating synthesis and characterization

For the further study of its application performance, a wide waveband two-components transparent NIR shielding coating contains ATO and Cs$_x$WO$_3$ film was synthesized using the waterborne polyurethane (WPU) as the film-forming resin. The physical properties and optical properties of the thermal insulation coating were investigated in this thesis. This coating shows an excellent mechanical property that the hardness was 3H and the adhesion property was 1 grade, besides, the coating combined with the WPU exhibited a high water resisting. The optimum mass ration between ATO and Cs$_x$WO$_3$ was 1:1, and the optimum thickness of the coating was 6.95μm. Under

these optimum conditions, the coating shown a high NIR light blocking rate of 90.4% and an excellent visible light transmittance of 74.3%.

10.1.4 Synthesis and preparation of Black-TiO$_2$ film

To further enhance the property of the two-component transparent thermal insulation NIR shielding coating contains ATO and Cs$_x$WO$_3$ film. The black-TiO$_2$ films were fabricated by controllable hydrothermal reaction and electrochemistry reaction. The effects of hydrochloric acid concentration, NH$_4$Cl concentration in electrochemistry, mass ratio between deionized water and ethylene glycol, voltage, and reaction time in electrochemistry were investigated, and finally the optimum reaction conditions were obtained. The optimum pH value in the hydrothermal reaction was 5.62. Meanwhile, the optimum NH$_4$Cl concentration, mass ratio between deionized water and ethylene glycol, voltage, and reaction time in electrochemistry was 15wt%, 1:1, 5V and 10min, respectively. The black-TiO$_2$ film in these optimum conditions shown an excellent NIR light blocking rate of 61.8%, and an excellent self-cleaning property with a water contact angle lower than 5° and a high MB degradation efficiency of 29.4% in 30min.

10.1.5 Preparation and characterization of the structural Black-TiO$_2$/ATO/Cs$_x$WO$_3$ thermal insulation coating

For the weiter application of the structural thermal insulation coating, the effect of the thickness for the two-component ATO/Cs$_x$WO$_3$ thin films on the optical property of structural thermal insulation coating was investigated. Finally, the optimum formula of the structural thermal insulation coating was obtained. The optimum of the two-

components coating was 4.63μm, and the structural coating exhibited a low NIR light transmittance of 6.3%, after the two-component ATO/Cs$_x$WO$_3$ thin film combined with black-TiO$_2$ film. Meanwhile, the structural thermal insulation coating exhibited an excellent photocatalytic property, which can degrade 29.4% of methylene blue in 30min. The WCA of the structural thermal insulation coating was only 3.5°. Besides, this chapter investigated the optical property comparison between the glass with structural thermal insulation coating, Low-E glass, tinted glass and original glass. The results show that the glass with the structural thermal insulation coating exhibited a high NIR light blocking rate of 93.7%, and a high UV light blocking rate of 96.8%, and the structural thermal insulation coating still exhibited a visible light transmittance of 58.6%. It means that the structural black-TiO$_2$/ATO/Cs$_x$WO$_3$ thermal insulation coating shows a great potential in energy conservation window.

10.2 Prospects

Further work regarding the novel structural Black-TiO$_2$/ATO/Cs$_x$WO$_3$ thermal insulation coating is as follows.

1) The large scale of the black-TiO$_2$ uniform film will be developed and investigated. Meanwhile, the further simple method of the black-TiO$_2$ synthesis will be developed. It should be further studied about the mechanism of the self-doping balck-TiO$_2$.

2) A novel microstructural of the black-TiO$_2$ should be developed in future, which exhibited a super-hydrophilic property in solar radiation, and a super-

amphiphobic in dark environment.

3) A novel insulation material which shows a high passive radiation property should be developed. After combined with the structural thermal insulation coating, this novel coating can have a greater potential for energy conservation of buildings.